Zeeman-Doppler Imaging of active late-type stars

Dissertation

Markus Kopf

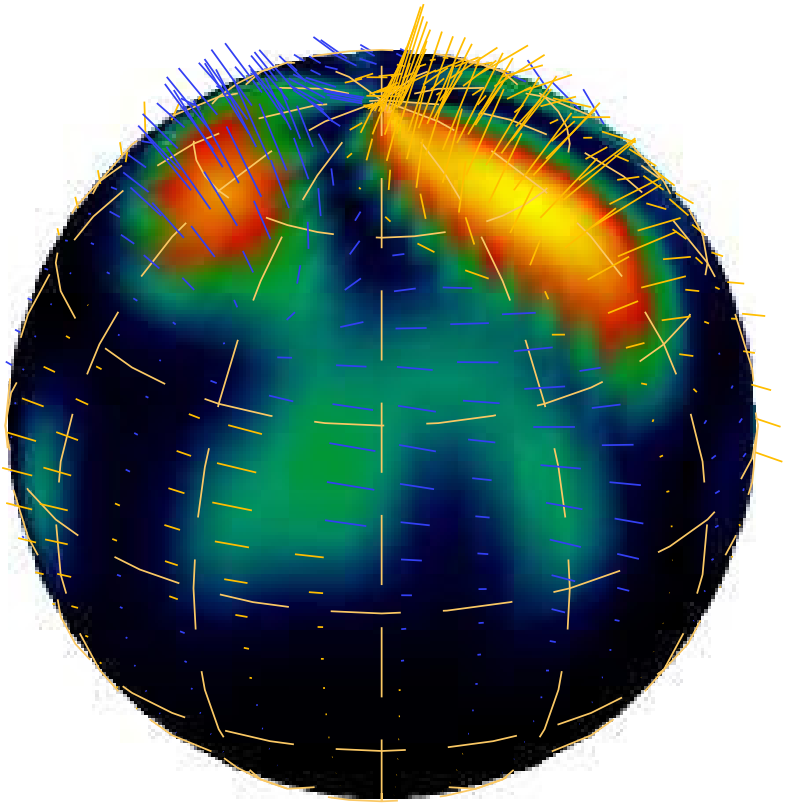

Astrophysikalisches Institut Potsdam

Zeeman-Doppler Imaging of active late-type stars

Dissertation
zur Erlangung des akademischen Grades
"doctor rerum naturalium"
(Dr. rer. nat.)
in der Wissenschaftsdisziplin Astrophysik

eingereicht an der
Mathematisch-Naturwissenschaftlichen Fakultät
der Universität Potsdam

von
Markus Kopf

Potsdam, November 2008

Published online at the
Institutional Repository of the University of Potsdam:
URL http://opus.kobv.de/ubp/volltexte/2009/3738/
URN urn:nbn:de:kobv:517-opus-37387
[http://nbn-resolving.org/urn:nbn:de:kobv:517-opus-37387]

Zusammenfassung

Stellare Magnetfelder spielen eine wichtige Rolle bei der Entstehung und Entwicklung von Sternen. Leider entziehen sie sich aber, aufgrund ihrer großen Entfernung zur Erde, einer direkten Beobachtung. Dies gilt zumindest für derzeitige und in naher Zukunft zur Verfügung stehende Instrumente. Um aber beispielsweise zu verstehen, ob Magnetfelder durch einen Dynamoprozess generiert werden oder Überbleibsel der Sternentstehung sind, ist es zwingend erforderlich, die Oberflächenstruktur und die zeitliche Entwicklung von stellaren Feldern zu untersuchen. Glücklicherweise haben wir mit der Dopplerverschiebung sowie der Polarisation von Licht Mittel zur Verfügung, um indirekt die Magnetfeldtopologie entfernter Sternen zu rekonstruieren, wenn auch nur die schnell rotierender. Die auf den beiden genannten Effekten basierende Rekonstruktionsmethode ist unter dem Namen *Zeeman-Doppler Imaging* (ZDI) bekannt. Sie stellt eine leistungsfähige Methode dar, um aus rotationsverbreiterten Stokes Profilen schnell rotierender Sterne Oberflächenkartierungen der Temperatur und Magnetfeldverteilung zu erstellen.

Durch das ZDI konnten in den vergangenen Jahren die Magnetfeldverteilungen zahlreicher Sterne rekonstruiert werden. Diese Methode stellt allerdings sehr hohe Anforderungen sowohl an die Instrumentierung als auch an die Rechenleistung und ist deshalb häufig mit zahlreichen Annahmen und Näherungen verbunden.

Ziel dieser Arbeit war es, Methoden für ein ZDI zu entwickeln, das darauf ausgelegt ist, zeitaufgelöste spektropolarimetrische Daten von aktiven späten Sternen zu invertieren. Es sollte also insbesondere den komplexen und lokalen Magnetfeldstrukturen dieser Sterne Rechnung getragen werden. Um die Orientierung und Stärke solcher Felder zuverlässig rekonstruieren zu können, sollte die Inversion im Stande sein, alle vier Stokes-Komponenten einzubeziehen. Ferner war vorgesehen auf vollständigen polarisierten Strahlungstransportmodellierungen aufzubauen. Dies ermöglicht eine simultane und selbstkonsistente Temperatur- und Magnetfeld-Inversion, die damit dem komplexen Zusammenspiel zwischen Temperatur und Magnetfeld gerecht wird. Schließlich sollte die Anwendung eines neu zu entwickelnden ZDI Programms auf Stokes I und V Beobachtungen von II Pegasi (kurz: II Peg) erste Magnefeldkarten dieses sehr aktiven Sterns liefern.

Um den hohen Rechenaufwand, der mit der Inversionsmethode einhergeht, besser bewältigen zu können, wurde zunächst eine schnelle Approximationsmethode für den polarisierten Strahlungstransport entwickelt. Sie basiert auf einer Hauptkomponentenanalyse (PCA) sowie auf künstlichen Neuronalen Netzen. Letztere approximieren den funktionalen Zusammenhang zwischen atmosphärischen Parametern und den zugehörigen lokalen Stokes Profilen.
Inverse Probleme sind potentiell schlecht gestellt und erfordern in der Regel eine Regularisierung. Der entwickelte Ansatz verwendet eine lokale Entropie, die auf die Besonderheiten bei der Rekonstruktion lokalisierter Magnetfeder eingeht. Ein weiterer neuartiger Ansatz befasst sich mit der Rauschreduktion polarimetrischer Beobachtungsdaten. Er macht sich die Hauptkomponentenanalyse zu Nutze, um mit Hilfe einer Vielzahl beobachteter Spektrallinien, einzelne Linien mit drastisch vergrößertem Signal-zu-Rausch-Verhältnis wieder zu geben. Diese Methode hat gegenüber anderen Multi-Spektrallinien-Verfahren den Vorteil, nach wie vor eine Inversion auf der Basis einzelner Spektrallinien durchführen zu können. Schließlich wurde das Inversionsprogramm *iMap* entwickelt, das die zuvor genannten Methoden implementiert.

Detaillierte Testrechnungen demonstrieren die Funktionsfähigkeit und Genauigkeit der schnellen Synthese-Methode und weisen einen Zeitgewinn von nahezu drei Größenordnungen gegenüber der konventionellen Strahlungstransportberechnung auf. Desweiteren untersuchen wir den Einfluss der verschiedenen Stokes Komponenten (IV bzw. IVQU) auf die Zuverlässigkeit, ein bekanntes Magnetfeld zu rekonstruieren. Damit belegen wir die Zuverlässigkeit unseres Inversionsprogrammes und zeigen darüber hinaus auch Einschränkungen von Magnetfeldinversionen im allgemeinen auf. Eine erste Inversion von Stokes I und V Profilen von II Peg liefert zum ersten Mal für diesen Stern simultan Temperatur- und Magnetfeldverteilungen.

Abstract

Stellar magnetic fields, as a crucial component of star formation and evolution, evade direct observation at least with current and near future instruments. However investigating whether magnetic fields are generated by a dynamo process or represent relics from the formation process, or whether they show a behavior similar to the sun or something very different, it is essential to investigate their structure and temporal evolution. Fortunately nature provides us with the possibility to indirectly observe surface topologies on distant stars by means of Doppler shift and polarization of light, though not without its challenges. Based on the mentioned effects, the so called Zeeman-Doppler Imaging technique is a powerful method to retrieve magnetic fields from rapid rotating stars based on measurements of spectropolarimetric observations in terms of Stokes profiles. In recent years, a large number of stellar magnetic field distributions could be reconstructed by Zeeman-Doppler Imaging (ZDI). However, the implementation of this method often relies on many approximations because, as an inversion method, it entails enormous computational requirements.

The aim of this thesis is to develop methods for a ZDI, designed to invert time-resolved spectropolarimetric data of active late type stars, and to account for the expected complex and small scale magnetic fields on these stars. In order to reliably reconstruct the detailed field orientation and strength, the inversion method is employed to be able to use of all four Stokes components. Furthermore it is based on fully polarized radiative transfer calculations to account for the intricate interplay between temperature and magnetic field. Finally, the application of a newly developed ZDI code to Stokes I and V observations of II Pegasi (short: II Peg) was supposed to deliver the first magnetic surface maps for this highly active star.

To accomplish the high computational burden of a radiative transfer based ZDI, we developed a novel approximation method to speed up the inversion process. It is based on Principal Component Analysis and Artificial Neural Networks. The latter approximate the functional mapping between atmospheric parameters and the corresponding local Stokes profiles. Inverse problems, as we are dealing with, are potentially ill-posed and require a regularization method. We propose a new regularization scheme, which implements a local entropy function that accounts for

the peculiarities of the reconstruction of localized magnetic fields. To deal with the relatively large noise that is always present in polarimetric data, we developed a multi-line denoising technique based on Principal Component Analysis. In contrast to other multi-line techniques that extract from a large number of spectral lines a sort of mean profile, this method allows to extract individual spectral lines and thus allows for an inversion on the basis of specific lines. All these methods are incorporated in our newly developed ZDI code *iMap*, which is based on a conjugated gradient method.

An in depth validation of our new synthesis method demonstrates the reliability and accuracy of this approach as well as a gain in computation time by almost three orders of magnitude relative to the conventional radiative transfer calculations. We investigated the influence of the different Stokes components (IV / IVQU) on the ability to reconstruct a known synthetic field configuration. In doing so we validate the capability of our inversion code, and we also assess limitations of magnetic field inversions in general. In a first application to II Peg, a K2 IV subgiant, we derived temperature and magnetic field surface distributions from spectropolarimetric data obtained in 2004 and 2007. It gives for the first time simultaneously the temporal evolution of the surface temperature and magnetic field distribution on II Peg.

Contents

List of Figures

List of Tables

1 Introduction

Magnetic fields play an important role in various domains of Astrophysics. They influence the formation and evolution of matter from galaxies over intergalactic media to stars. Concerning stars, magnetic fields play a key role in the understanding of solar and stellar activities of which spots are one of the most prominent manifestations, though flares, prominences and coronal mass ejections (CMEs) are also attributed to magnetic fields. First records of sunspot observations by naked-eye date back to Chinese astronomers more than 2000 years ago, but first detailed studies were carried out in 1611 by Christoph Scheiner (1575-1650) and Galileo Galilei (1564-1642). They developed and utilized instruments to keep track of the sunspot movements across the solar disk and to study their temporal evolution. Figure 1.1 shows a drawing from Christoph Scheiner's main work *Rosa Ursina sive Sol* on sunspots. Continuous observations throughout the last centuries allowed for the finding of maxima and minima in the solar activity, such as the 70 years lasting Maunder-Minimum, as well as a periodic evolution of sunspots that has an average cycle length of 11 years. This cyclic behavior was found by Heinrich Schwabe in 1843. Another important observation was made by George Ellery Hale (1868-1938) in 1908. He found the presence of strong magnetic fields within sunspots and thereby marked the beginning of the study of solar magnetic activity.

Consequently, scientists later wanted to observe temperature and magnetic field distributions on the surface of stars beyond the Sun to understand their influence on star formation and evolution in general. As direct surface resolving observations are not possible on stars other than the Sun, an indirect method was required. The idea for what is known today as Doppler Imaging (DI) was already formulated in 1958 by Armin Deutsch (1958). The basic concept is to use rotationally broadened spectral line profiles of fast rotating active stars to map their surface structures. First realizations of this method for mapping element abundances were made by Goncharskii et al. (1977) and Khokhlova & Riabchikova (1975). The name Doppler Imaging however was introduced by Vogt & Penrod (1983) when the method was used for temperature mapping. Following the same principle, and additionally utilizing spectral line polarization due to the Zeeman effect, Semel (1989) established the Zeeman-Doppler Imaging (ZDI) technique for inferring stellar magnetic fields. This method was further developed by means of image reconstruction al-

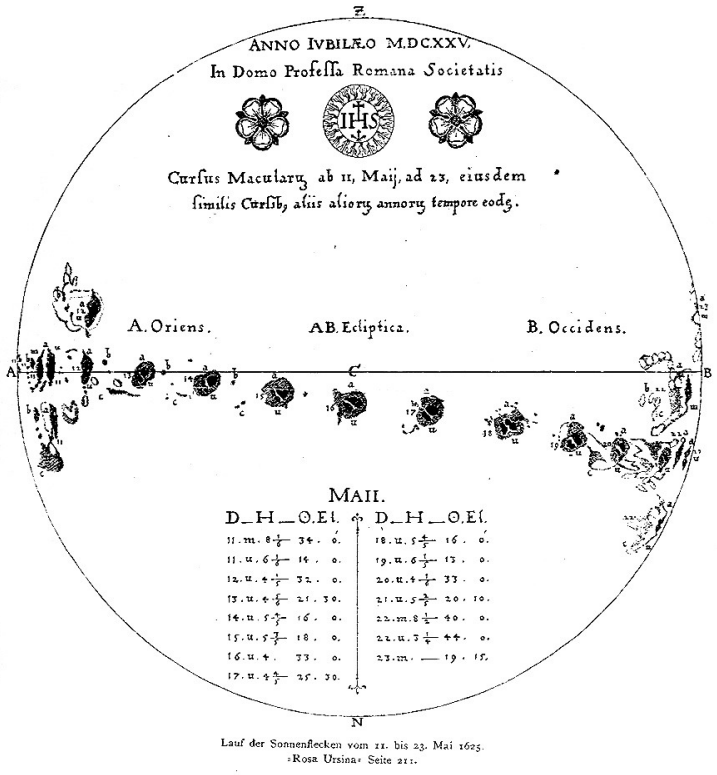

Figure 1.1: Sunspot drawings from Christoph Scheiner's (1575-1650) main work *Rosa Ursina sive Sol*, published 1626-1630.

gorithms by e.g. Brown et al. (1991), Piskunov & Rice (1993) and Donati et al. (1997).

Since then, magnetic fields have been widely studied by ZDI on chemically peculiar stars (Ap/Bp) exhibiting large scale magnetic fields (Donati & Semel 1990; Kochukhov et al. 2004). Concerning late-type stars, there has been many studies measuring the Zeeman broadening (e.g. Robinson 1980; Johns-Krull et al. 1999) of unpolarized but magnetically sensitive spectral lines, indicating the presence of magnetic fields. However, this method is valid only for slowly rotating stars and allows simply for an estimate of the average magnetic field strength. The more informative ZDI method has been applied only to a small number of late-type stars, compared to that of chemically peculiar stars.

The reason for that lies essentially in the relatively (compared to, e.g., Ap stars) weak and small scale magnetic fields of active late-type stars, which result in small polarization signals (of the order of 10^{-3} in circular polarization and 10^{-4} in linear polarization). Furthermore they are rather faint objects. This altogether makes their observation very difficult, especially in Stokes Q and U (linear polarized light).

Until now, observations in full Stokes have been carried out only for a limited number of AP stars (Wade et al. 2000; Kochukhov et al. 2004; Khalack & Wade 2006).

A technique, known as *Least-Squares Deconvolution* (Donati et al. 1997), could help to enhance the Zeeman signatures of Stokes V (circular polarized light) profiles by co-adding several thousand individual lines to form a mean profile. The difficulty of this technique however is the interpretation of the mean profile. It does not allow for the radiative transfer calculation on the basis of individual atomic lines and further involves for Stokes V the weak field approximation (Jefferies et al. 1989).

Our development of an inversion method (ZDI) and diagnosis tools for late-type stars was largely motivated by the forthcoming spectropolarimeter PEPSI[1] which will be installed at the Large Binocular Telescope (LBT) and developed at the Astrophysical Institute Potsdam (AIP). It particularly aims for the observations of solar-type stars in all four Stokes components. With PEPSI at LBT it is possible to achieve required spectral resolution of up to 120.000 and polarimetric precision of 10^{-5} for targets brighter than V=4mag in 1 hour integration time (Strassmeier et al. 2008).

Due to instrumental limitations and the complexity of ZDI, many applications rely on approximation methods which use, e.g., Stokes I profiles from template stars or model Stokes I with simple Gaussian profiles. Corresponding Stokes V profiles are then derived via the weak field approximation. This procedure allows to completely bypass the application of radiative transfer methods.

However a study of the complex magnetic fields of late-type stars must, as a final goal, incorporate the modeling of essential physical processes by means of full polarized radiative transfer calculations.

In this effort we have developed a ZDI code "iMap" that incorporates, beside the conventional numerical polarized radiative transfer calculation, a novel method for fast and accurate Stokes profile synthesis under local thermodynamic equilibrium (LTE). It is based on artificial neural networks which are trained on the conventional radiative transfer method to find an approximation of the mapping between atmospheric parameters and the corresponding local Stokes profiles.

Our full Stokes Zeeman-Doppler Imaging is based on a conjugated gradient method and an adopted maximum entropy regularization that is more appropriate for the mapping of the vector magnetic field. In the first application, we present surface magnetic field maps of II Pegasi (short: II Peg) for the years 2004 and 2007. Here we also employ a new multi-line technique which makes use of a larger number

[1]Potsdam Echelle Polarimetric and Spectroscopic Instrument

of spectral lines to reconstruct less noisy single line profiles and thus allow for inversion on the basis of individual spectral lines. This means, that for the first time, a radiative driven inversion approach is applied to spectropolarimetric data of II Peg.

1.1 Solar and stellar activity

Solar activity denotes the dynamic processes associated with magnetic fields that are expressed in various phenomena seen on the Sun. Analogous phenomena are expected to be also present on other stars exhibiting a convective envelope. In case of other stars it is then referred to as stellar activity. Some of the solar phenomena are shown in Fig. 1.2. The fruitful interaction between solar and stellar studies is generally referred to as the *solar-stellar connection* (Dupree 2003; Strassmeier 2004).

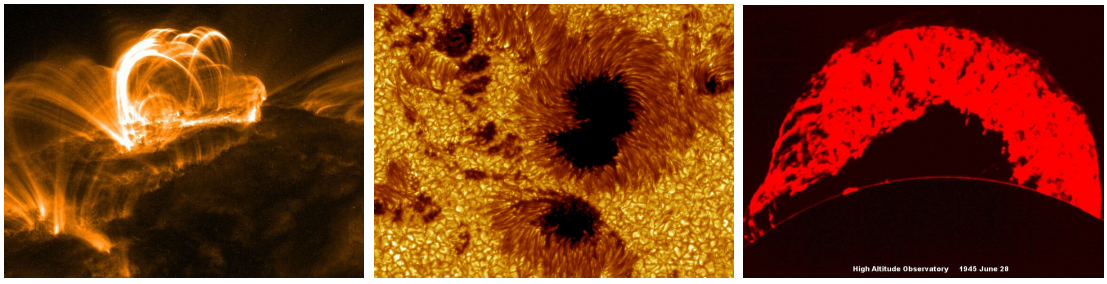

(a) Flare (b) Sunspots (c) Prominence

Figure 1.2: Solar activity phenomena, which are direct manifestations of magnetic fields: (a) Typical solar flare, captured in the X-ray waveband by NASA's TRACE satellite. (b) High resolution image of a sunspot observed with the Swedish 1-m Solar Telescope. (c) Large prominence "Granddaddy" observed in 1946 at the High Altitude Observatory. It extends some 200 000 km above the solar surface.

Activity phenomena on the Sun, as a neighboring star, are well studied. Therefore I will use solar activity as an example to describe stellar activity in general.

Spots are tracers of a tube-like magnetic field structure, which arises from the bottom of the convection zone and permeates the photosphere. Within the convection zone the convective energy transport is suppressed. As a consequence, this region has a lower temperature than its surroundings and therefore appears darker. It can

be stated as a generalized rule for stars that the occurrence of spots requires the existence of a convection zone.

Solar spots often appear as bipolar groups, where two involved spots harbor fields of opposite polarity. Their number and area varies largely in time as illustrated in Fig. 1.3, but also the position of spots on the solar disk varies with time. In the upper frame of Fig. 1.3, the latitudinal occurrence of spots, whose relative size is concurrently color-coded, is plotted over time, showing plainly an 11-year solar cycle. This plot is known as the *Butterfly-Diagram*. It can also be seen that, at the beginning of each new cycle, spots appear first at high latitudes and, as the cycle progresses, migrate towards lower latitudes, ending up very close to the equator. Besides these relatively short variations there are also long term variations. Between

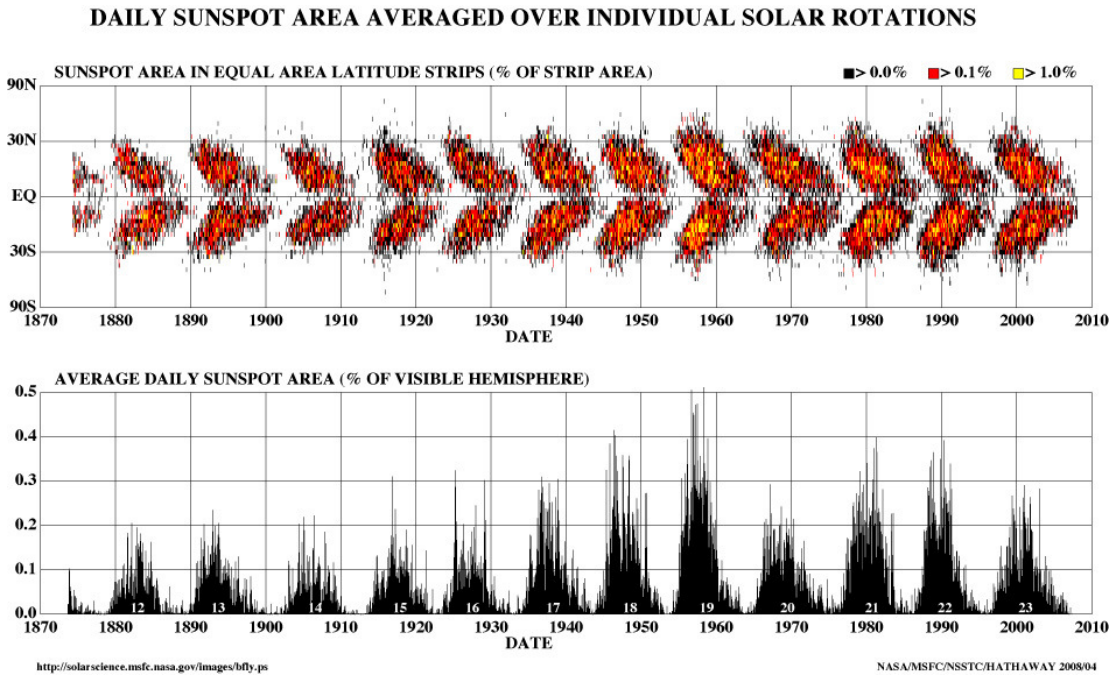

Figure 1.3: Diagrams showing the latitudinal occurrence of spots over time together with the color coded relative spot size (upper plot, known as the butterfly-diagram) and the average daily sunspot area versus time. Both plots show nicely the 11-year solar cycle.

1650 and 1700, for example, there happened to be a pronounced activity minimum (known as Maunder-Minimum), during which almost no spots were present on the solar surface. While the 11-year cycle could qualitatively be reproduced by magneto-hydrodynamic (MHD) simulations, the long term variations are still not well enough understood to be modeled.

The formation of stellar spots is similar to that of solar spots, but considering their

size, stellar spots can have a much larger extent and the total spot coverage can be in the order of a few percent compared to a maximum of 0.5% on the Sun (Strassmeier 1997). However, it is believed that large spots appearing in Doppler images are indeed clusters of spots.

Another characteristic of the Sun are the so-called active longitudes. These are longitudes at which magnetic activity concentrates and repeatedly shows up over longer timescales, up to the length of a solar cycle. A similar behavior was found by Berdyugina & Tuominen (1998) on RS CVns where mostly two dominant active regions were present and located about 180° apart. They show a periodic switching from one active longitude to the other, which is referred to as the *Flip-Flop* phenomenon (Berdyugina et al. 2005).

A somewhat controversial feature, though found on many stars, is a large polar spot (Strassmeier 1996). On the Sun spots are located at low latitudes typically between $10° - 40°$. There have been simulations reproducing high latitude spots (Schrijver & Title 2001), but the mechanisms, responsible for polar spots, are still not clearly understood.

1.2 Origin and evolution of stellar magnetic fields

The generation of stellar magnetic fields is usually explained by a dynamo theory. Within this framework, convection and differential rotation play key roles. However, we are still lacking a complete description of magnetic field generation in the Sun and stars. The so called $\alpha\Omega$ dynamo theory is in fact able to explain, e.g., the 11 year cycle, but lacks the ability to reproduce other effects, such as the latitudinal drift seen in the butterfly diagram (Fig. 1.3). It turns out, that for the understanding of a nonlinear dynamo the magnetic helicity plays a fundamental role (Brandenburg & Subramanian 2005). In stellar physics, a way to asses the helicity is to observe the stellar surface magnetic fields.

The convection zone, in which energy is transported by plasma motion rather than by radiation, spans about the outer third of the Sun. It is believed that rotation, together with convection, drives the dynamo that generates magnetic fields ranging from the bottom of the convection zone up to the photosphere, and even reaching out into the chromosphere. The $\alpha\Omega$-dynamo founded by Parker (1955) is basically constituted by two effects, the α and the Ω effect. According to this dynamo model, the differential rotation (on the Sun, the equator is rotating faster than the poles) is responsible for the transformation of a poloidal magnetic field into a toroidal magnetic field. This effect is named the Ω effect, because Ω generally

stands for the degree of differential rotation. The α effect describes the generation of a poloidal field by a toroidal field due to the Coriolis Force. The two effects produce alternately poloidal and toroidal flux tubes, thus maintaining a permanent field generation mechanism. Magnetic fields, or the imprints we see on the surface, are explained as toroidal flux tubes rising, due to turbulence and magnetic buoyancy, to the surface. The Coriolis Force causes it to twist in a clockwise direction in the northern hemisphere and in a counter-clockwise direction in the southern hemisphere. What we see is a bipolar group with a proceeding and a following spot of mutual polarity. The $\alpha\Omega$-dynamo is the preferred model for the Sun and other late-type stars. However, there is another dynamo mechanism able to generate large scale magnetic fields by the α effect alone. In this case also toroidal fields are generated by the α-effect. This model is therefore named α^2 dynamo. For a general review of astrophysical dynamo theory, see Brandenburg & Subramanian (2005).

There are other stars with strong magnetic fields, that do not harbor a convection zone and therefore no dynamo. These are typically young stars. It is believed that their field is a relic from the formation process of the star: the field present in the collapsing gas cloud was frozen in and still remains. The field is usually referred to as *primordial*. Classical representatives, which were in the past the main targets for ZDI, due to their strong, global magnetic fields, are Ap and Bp stars.

Concerning stellar activity, we are primarily interested in late-type stars, particularly solar-type stars, motivated by the solar-stellar connection, aiming for deeper insight into physical processes happening on the Sun.

1.3 Late-type stars

Stars with an outer convection zone are generally referred to as late-type stars and possess a dynamo that generates complex magnetic fields. Their spectral class ranges from F7 to K2 stars (Berdyugina et al. 2005), their temperature from about 3500 K to 7500 K and mass from $0.8 to 1.7\ M_{\odot}$. This means that our sun, of spectral type G2 V and laying on the main sequence, is a particular star in a sense that it is positioned in our immediate neighborhood, but is otherwise a rather ordinary late-type star among many others. Nevertheless, it seems to exhibit some special features, once compared to other Doppler Imaging observed stars. However, one should keep in mind when comparing the Sun with other stars mapped by Doppler and Zeeman-Doppler Imaging that both methods rely on rapidly rotating stars, while the Sun is a slow rotator. It is possible that common phenomena seen on other stars could be associated with selection effects. Some striking aspects, found on

solar-type stars are, e.g., rather large scale surface patches, anti-differential rotation or polar spots. We identify the following subtypes:

Solar-type stars is a synonym for those stars that have effective temperature, luminosity, chemical composition, and activity similar to those of the sun. That means they are also located on the lower main-sequence, have effective temperatures ranging from about 4900 K to 6400 K, are of spectral type between F7 and K2 and show a similar chromospheric activity, detected for example in the Ca II H & K emission. Photometric variability due to spot modulation reaches up to a maximal few tenth of a percent on the Sun, but can reach several percent on other solar-type stars.

T Tauri stars are young pre-main sequence stars undergoing a phase of high activity. Their young age of a few million years is noticeable by enhanced lithium absorption. Typically, they are surrounded by an accretion disk, a relic from the star formation process, and show some very strong emission lines. Especially at locations where matter from the disk is magnetically accreted, there appear hot spots. The strong surface activity of these low mass stars comes along with a high magnetic activity, accretion flows and stellar wind phenomena. The name that was given to that class of stars originates from the prototype star "T Tauri".

RS CVn stars form a system of close detached binaries exhibiting strong photometric variability, which was assigned by Eaton & Hall (1979) to star spot modulation. A spot coverage of up to 50 % can be found which makes them a particularly interesting target for Doppler and Zeeman-Doppler Imaging. Other characteristics include strong chromospheric Ca II H & K emission lines and fast stellar rotations with orbital periods of a few days. This type of star owes its classification name to the prototype stellar system RS CVn. II Peg, the object of consideration in this work belongs also to this class.

FK Com stars are rapidly rotating single G- or K-giants. The prototype star of this class is FK Comae which rotates with an impressive projected equatorial velocity of 160 km/s. Like RS CVn stars, they also show chromospheric activity with strong emission in the Ca II H & K lines.

1.4 Observation and diagnostic techniques

The lack of reasonable direct spatial resolution of any other star except the Sun, can be overcome by several observational and diagnostic techniques which allow to derive indirectly some information about their surface distributions. These methods are:

Photometry and Light-curve modeling: One of the first methods for the detection of star spots was photometry, which measures the total flux of a stellar object in a certain wavelength band. Kron discussed already in 1950 the possibility of photometric spot detections (Kron 1950). Since about the 1970's this method allowed for the detection of stellar surface variations, even for faint objects, due to the observation in integral light. First attempts to deduce spot distributions from photometric observations were based on trial and error light-curve modeling. A more mathematical way consisted then later on a two temperature light-curve inversion. Photometric data and light-curve inversion are often incorporated into Doppler Imaging, putting further constraints on the inversion (e.g. Rice & Strassmeier 2000).

Spectroscopy and Doppler Imaging: One of the most important observational tools in astrophysics is spectroscopy. It is the dispersion of visible light according to its wavelength and allows for resolving individual spectral lines. Todays spectrographs use mostly cross-dispersers, which allow for the simultaneous detection of a large spectral range. Thus, with a single exposure, many spectral line profiles become available.

The idea of using individual rotationally broadened line profiles, to derive surface temperature or abundance distributions, was first formulated by Deutsch (1958). As an optimization process, it was first realized by Goncharskii et al. (1977) and ever since applied to many stellar objects. It has been further developed by e.g. Vogt & Penrod (1983); Rice et al. (1989); Piskunov & Rice (1993); Rice & Strassmeier (2000). Existing Doppler images of late-type stars were summarized by Strassmeier (2002). A prerequisite is the rapid rotation of the considered star. The projected equatorial velocity should be larger than about 20 km/s, because only then the rotational broadening dominates the natural line broadening and a meaningful surface imaging is possible. Furthermore, to achieve a reasonable stellar surface resolution with Doppler Imaging, a spectral resolution of better than 35 000 is needed. The other important quantity is the signal-to-noise ratio (SNR) which must be high enough so that deviations introduced by a surface spot stand out in the line profile

from the noise. Instruments used for spectroscopy are, e.g., UVES at VLT, HIRES at KECK, or FORS at VLT. New developments go in the direction of robotic telescopes, such as STELLA (STELLar Activity), with the ambition to do follow-ups and derive long term activity variations and possibly obtain butterfly diagrams or flip-flop cycles.

Polarimetry and Zeeman-Doppler Imaging: Polarimetry, sometimes called Spectropolarimetry, refers to the spectroscopic measurement of polarized light, which carries details about the magnetic field configuration at the point of origin. For that purpose an elaborate polarization unit is connected ahead of the spectrograph and the so-called Stokes profiles are obtained. One difficulty in the disk integrated detection of small scale stellar magnetic fields is the mutual cancellation of local Stokes V profiles originating from regions harboring mixed polarities. As a result the disk integrated Stokes V profiles can be very small, which makes their detection and reconstruction rather challenging. The reconstruction of stellar magnetic fields can be achieved by Zeeman-Doppler Imaging. It is based on Doppler Imaging and polarization signals (Stokes IQUV) evoked by the Zeeman effect and was first proposed by Semel (1989). Like DI it also requires a fast stellar rotation.

1.5 Overview of the thesis

The objective of the present thesis was the development of analysis and diagnosis methods for the reconstruction of surface magnetic fields (Zeeman-Doppler Imaging) of active late-type stars employing all four Stokes components.

Chapter 2 gives an introduction to the essential physics involved, when studying stellar magnetic fields, i.e., the polarized radiative transfer (RT) calculation. Since Zeeman Doppler Imaging requires comprehensive and repeated RT calculations, we have developed a fast synthesis method, which is described and evaluated in Chap. 3. The following Chap. (4) presents our new inversion code *iMap* which performs the actual magnetic field reconstruction, incorporating an adapted maximum entropy regularization. Finally Chap. 6 presents temperature and magnetic field inversions of the very active binary star II Peg and discusses the observations. Chapter 7 draws final conclusions and gives an outlook on future investigations.

2 Polarized radiative transfer

This chapter gives an overview of the theory of polarized radiative transfer. First, polarization and its representation by the Stokes vector is described, then spectral line splitting in the presence of a magnetic field is addressed, and finally the actual radiative transfer and its formal solution is discussed.

2.1 Polarized light and Stokes parameters

Electromagnetic waves are described, in the picture of electromagnetic theory, by the electric and magnetic field vectors located in a plane, which is perpendicular to the direction of propagation. The orientation of the electric field vector specifies the polarization direction. If this direction is constant in time, the light is called linear polarized. If the field vector describes an ellipse in the plane perpendicular to the propagation direction, it is called elliptically polarized. A special case hereof is the circular polarization, where the field vector describes a circle. To fully specify the polarization state of light, besides the monochromatic intensity I_ν, three more variables are necessary. A formal description of the polarization states, which is also associated with measurable quantities (observables) and therefore particularly useful, was introduced 1852 by George G. Stokes. The components of the electric field vector $\boldsymbol{E}$ of a monochromatic wave, propagating in z-direction ($E_z = 0$) of a right-handed cartesian coordinate system, are given by:

$$\begin{aligned} E_x &= A_x \cos(\omega t - \phi_x) \\ E_y &= A_y \cos(\omega t - \phi_y) \quad , \end{aligned} \tag{2.1}$$

where A_x and A_y are the amplitudes, ω the circular frequency, ϕ_x and ϕ_y the phase shifts and t denotes time. For the description of a single wave train, the amplitude ratio, phase offset, and circular frequency are in fact adequate. However for a astrophysical observation with the multitude of independent rays from many atomic transitions, these parameters are not feasible. In this case, the Stokes formalism

allows an exact description in a statistical sense. The four Stokes parameters are defined by:

$$\begin{aligned} I &= < A_x^2 + A_y^2 > \\ Q &= < A_x^2 - A_y^2 > \\ U &= < 2A_x A_y \cos(\phi_x - \phi_y) > \\ V &= < 2A_x A_y \sin(\phi_x - \phi_y) > \quad , \end{aligned} \tag{2.2}$$

where the angle brackets indicate the average over time. The parameter I is a measure of the total intensity, Q and U of the linear, and V of the circular polarized intensity. They are summarized in the Stokes vector $\boldsymbol{I} = (I, Q, U, V)^{\mathsf{T}}$. For fully polarized light it holds the relation $I^2 = Q^2 + U^2 + V^2$ and the degree of polarization, defined as the ratio of polarized intensity to total intensity, is:

$$p = \frac{\sqrt{(Q^2 + U^2 + V^2)}}{I}. \tag{2.3}$$

After some transformation (see, e.g., Rees 1987; Rutten 2003), the four Stokes parameters (Eq. 2.2) can be expressed in a more intuitive way, which also gives a clear observational strategy:

$$\begin{aligned} I &= \text{total Intensity} \\ Q &= I_0^{linear} - I_{90}^{linear} \\ U &= I_{+45}^{linear} - I_{-45}^{linear} \\ V &= I_{right}^{circular} - I_{left}^{circular} \end{aligned} \tag{2.4}$$

Stokes Q and U can thus be measured by the difference of intensities, which remain after the passage of two crossed linear polarizers oriented at angles 0° and 90°. The intensity difference of right and left circular polarized light gives Stokes V.

2.2 Zeeman effect

The splitting of atomic energy levels and thus the splitting of spectral lines due to an external magnetic field was first observed in 1896 by the Dutch physicist Pieter Zeeman. This effect, named after him, was a little later explained on the basis of classical theory of the electron by Hendrik A. Lorentz. It is a result of the interaction between the total atomic magnetic momentum and the external magnetic field.

Historically there exists the terms *normal* and *anomalous* Zeeman effect. The normal Zeeman effect occurs if one of the energy levels involved in the transition has a quantum number $J = 0$ or if both levels have the same Landé factor ($g_l = g_u$), as it is for example the case for singlet states. In this case, the spectral line splits into

three separated components, which show different polarization states. The more general case however is the anomalous Zeeman effect. Here the Landé factors are different and several lines emerge. In the following, a derivation of the wavelength shift induced by the magnetic field is given and some important parameters are introduced. A detailed description of the Zeeman effect can be found, e.g., in Haken & Wolf (1996).

For an atom with an orbital and a spin momentum in an external magnetic field $\boldsymbol{B}$, the Hamilton operator is the sum of the undisturbed simple Hamiltonian H_0 and a perturbation term H_B, which describes the spin-orbit coupling:

$$H = H_0 + H_B \tag{2.5}$$

with

$$H_0 = \frac{p^2}{2m_e} + V \ , \quad H_B = -\boldsymbol{\mu}\boldsymbol{B} \ . \tag{2.6}$$

The magnetic moment $\boldsymbol{\mu}$ is given by:

$$\boldsymbol{\mu} = -\frac{\mu_B}{\hbar}(g_l\boldsymbol{L} + g_s\boldsymbol{S}) = -\frac{\mu_B}{\hbar}(\boldsymbol{L} + 2\boldsymbol{S}) \tag{2.7}$$

where p is the particle momentum, m_e the electron mass, V the potential energy and $\mu_B = \hbar e/2m_e$ the Bohr magneton, with $\hbar$ as the reduced Planck constant, and e the electron charge. The variables $g_l = 1$ and $g_s \approx 2$ are the gyromagnetic ratios and $\boldsymbol{L}$ and $\boldsymbol{S}$ the orbital and spin angular momentum, respectively. Here it is also assumed that the magnetic field is weak (< 10000 G), so that the spin-orbit coupling dominates over the interaction with the external field and the total angular momentum can be written as $\boldsymbol{J} = \boldsymbol{L} + \boldsymbol{S}$. This is known as the LS coupling or *Russel-Saunders* coupling.

If we assume the magnetic field to be in z-direction $\boldsymbol{B} = (0, 0, B_z)^\mathsf{T}$, the relevant projection of the total momentum on the z-axis is $J_z = m_j\hbar$ with the magnetic quantum number $m_j = -J, -J+1, ..., +J$, where J is the total angular momentum quantum number. So according to first order perturbation theory the $(2J+1)$ degeneracy is split and the energy-shift due to the external magnetic field is:

$$\Delta E_{mag} = \mu_B m_j g B \tag{2.8}$$

with the Landé factor:

$$g = 1 + \frac{J(J+1) - L(L+1) + S(S+1)}{2J(J+1)} \quad , \tag{2.9}$$

where J, L, S are quantum numbers corresponding to the total angular momentum, orbital angular momentum and spin angular momentum.

Spectral lines are generated by the transition of an electron between the degenerated states of two energy levels (an upper and a lower level). The wavelength of a photon resulting from such a transition $l \rightarrow u$ is shifted by:

$$\Delta\lambda_B = \frac{e}{4\pi m_e c} g^\star \lambda_0^2 B \tag{2.10}$$

where e is again the electron charge, c the speed of light and λ_0 the central labor wavelength of the line. The Landé factor is given by $g^\star = g_l m_l - g_u m_u$, where the indices l, u depict the lower and upper sublevels. This means the Zeeman splitting scales linearly with the magnetic field, but quadratic with the wavelength of the considered line. Consequently, the spectral resolution is greater the *more red* the observed line is. The special case of the normal Zeeman effect occurs, if $J = 0$ for one of the levels, because then it follows $m = 0$ for that level and due to the selection rules for electric dipole transitions ($\Delta m = 0, \pm 1$) there appear only three lines. The normal Zeeman effect also arises when the lower and the upper Landé factors are equal ($g_l = g_u$) so that the energy shifts in both levels equal each other.

In the more general anomalous Zeeman effect however, both levels are described by two different Landé factors and the energy splitting are different. Typically the two Landé factors are summarized as one effective Landé factor g_{eff}. Even though it does not fully describe the splitting, it is a reasonable approximation. The weighted mean of the upper and lower Landé factors is given by:

$$g_{eff} = \frac{1}{2}(g_l + g_u) + \frac{1}{4}(g_l - g_u)(J_l(J_l + 1) - J_u(J_u + 1)) \quad , \tag{2.11}$$

which gives a guide value for the magnetic sensitivity of a spectral line.

2.3 Radiative transfer

The formation of Zeeman split spectral lines is a process of absorption and emission of rays traveling through the media of a stellar atmosphere. Mathematically this is expressed by the polarized radiative transfer equation (Rees 1987)

$$\frac{d\boldsymbol{I}}{dz} = -\mathsf{K}(\boldsymbol{I} - \boldsymbol{S}) \tag{2.12}$$

where $\boldsymbol{S}$ is the source vector, K the absorption matrix, $\boldsymbol{I} = (I, Q, U, V)^\mathsf{T}$ the Stokes vector, and z the geometrical distance along the line of sight. In the non-magnetic case, all three quantities reduce to scalars and make Eq. 2.12 a single differential equation. Here in the magnetic case however, due to the rather complex dependence of K on the magnetic field, Eq. 2.12 represents four coupled differential

equations. In this work, Local Thermodynamic Equilibrium (LTE) is assumed and continuum polarization is neglected (Rees 1987), so the source vector can be written as

$$\boldsymbol{S} = B_\nu(T)\boldsymbol{e}_0 \quad . \tag{2.13}$$

with the Planck function

$$B_\nu(T) = \frac{2h\nu^3}{c^2}(e^{h\nu/kT} - 1)^{-1} \tag{2.14}$$

at local temperature T and with $\boldsymbol{e_0} = (1, 0, 0, 0)^\mathsf{T}$ to account for neglecting continuum polarization. The total absorption matrix is given by

$$\mathsf{K} = \kappa_c \mathsf{1} + \kappa_0 \mathsf{\Phi} \tag{2.15}$$

where κ_c is the continuum absorption coefficient and κ_0 is the line absorption coefficient. The line absorption matrix is given by:

$$\mathsf{\Phi} = \begin{pmatrix} \phi_I & \phi_Q & \phi_U & \phi_V \\ \phi_Q & \phi_I & \phi'_V & -\phi'_U \\ \phi_U & -\phi'_V & \phi_I & \phi'_Q \\ \phi_V & \phi'_U & -\phi'_Q & \phi_I \end{pmatrix} \tag{2.16}$$

with the components

$$\begin{aligned} \phi_I &= \tfrac{1}{2}\phi_p \sin^2\gamma + \tfrac{1}{4}(\phi_r + \phi_b)(1 + \cos^2\gamma) \\ \phi_Q &= \tfrac{1}{2}[\phi_p - \tfrac{1}{2}(\phi_r + \phi_b)] \sin^2\gamma \cos 2\chi \\ \phi_U &= \tfrac{1}{2}[\phi_p - \tfrac{1}{2}(\phi_r + \phi_b)] \sin^2\gamma \sin 2\chi \\ \phi_V &= \tfrac{1}{2}(\phi_r - \phi_b)\cos\gamma \\ \phi'_Q &= \tfrac{1}{2}[\phi'_p - \tfrac{1}{2}(\phi'_r + \phi'_b)] \sin^2\gamma \cos 2\chi \\ \phi'_U &= \tfrac{1}{2}[\phi'_p - \tfrac{1}{2}(\phi'_r + \phi'_b)] \sin^2\gamma \sin 2\chi \\ \phi'_V &= \tfrac{1}{2}(\phi'_r - \phi'_b)\cos\gamma \quad , \end{aligned} \tag{2.17}$$

where $\phi_{p,b,r}$ are the absorption profiles and $\phi'_{p,b,r}$ are the anomalous dispersion profiles. These equations show that the total absorption matrix (Eq. 2.15) depends via the line absorption matrix (Eq. 2.16), and thus via the absorption and anomalous dispersion profiles, in a complex way on the magnetic field vector $\boldsymbol{B}$, specified by the field strength B, inclination γ and the azimuth χ as shown in Figure 2.1. The letters p, b, r in Eq. 2.17 characterize the Zeeman components, letter p stands for the π component, while b and r represent the blue and red shifted components of the normal Zeeman effect. These components correspond to the energy levels of the line forming transition with the magnetic quantum numbers m_u, m_l in the following way:

$$\Delta m = m_u - m_l = \begin{cases} +1 \equiv b & (\sigma^+) \\ 0 \equiv p & (\pi) \\ -1 \equiv r & (\sigma^-) \quad . \end{cases} \tag{2.18}$$

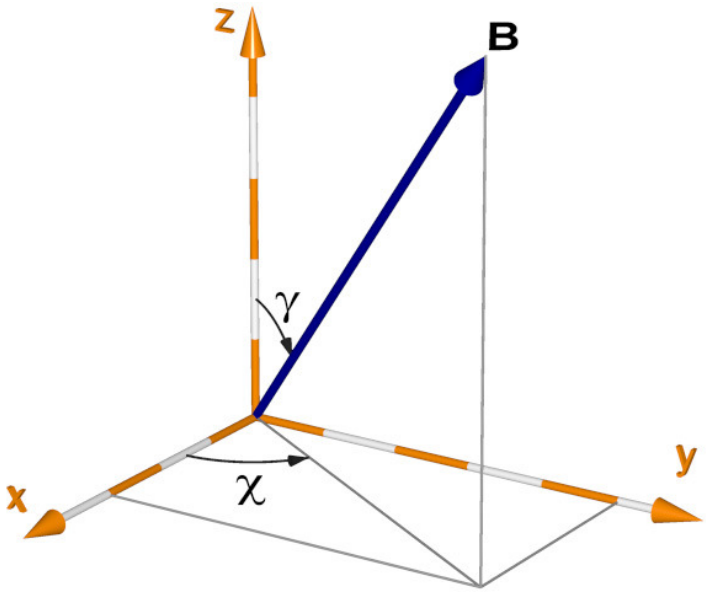

Figure 2.1: The reference frame for the definition of the magnetic field vector, in which the z-axis equals the line of sight. The inclination (γ) is the angular between the magnetic field vector and the line of sight (z-axis). The azimuth (χ) is the angle between the x-axis and the projection of the magnetic field vector on the xy-plane.

The absorption profiles and anomalous dispersion profiles are given by:

$$\begin{array}{ll} \phi_p = H(a,v) & \phi'_p = 2F(a,v) \\ \phi_b = H(a,v+v_B) & \phi'_b = 2F(a,v+v_B) \\ \phi_r = H(a,v-v_B) & \phi'_r = 2F(a,v-v_B) \end{array} \quad . \tag{2.19}$$

Here $H(a,v)$ and $F(a,v)$ are the Voigt and Faraday-Voigt functions, respectively, given by:

$$H(a,v) = \frac{a}{\pi} \int_{-\infty}^{\infty} \frac{e^{-y^2}}{(v-y)^2 + a^2}\, dy \tag{2.20}$$

$$F(a,v) = \frac{1}{2\pi} \int_{-\infty}^{\infty} \frac{(v-y)e^{-y^2}}{(v-y)^2 + a^2}\, dy \quad , \tag{2.21}$$

where

$$a = \frac{\Gamma_{\text{Rad}} + \Gamma_{\text{Stark}} + \Gamma_{\text{van der Waals}}}{4\pi c \Delta\lambda_D} \tag{2.22}$$

is expressed in units of the Doppler width $\Delta\lambda_D$ and contains contributions from radiation, stark, and van der Waals damping. The distance from the line center is given by

$$v = \lambda - \lambda_0 / \Delta\lambda_D \tag{2.23}$$

and the Zeeman splitting by

$$v_{ij} = \Delta\lambda_{ij}/\Delta\lambda_D \quad , \tag{2.24}$$

for transitions $i \rightarrow j$, which reduces to $v_B = \lambda_B/\Delta\lambda_D$ for a Zeeman triplet. The wavelength shift $\Delta\lambda_{ij}$ of the Zeeman components is given by:

$$\Delta\lambda_{ij} = \frac{e\lambda_0^2 B}{4\pi m_e c^2}(g_l m_l - g_u m_u)_{ij} \tag{2.25}$$

where e, m_e, and c are the electron charge, the electron mass and the speed of light, respectively.

2.3.1 Formal solution of the transfer equation

An analytical solution of the polarized radiative transfer equation (Eq. 2.12) is in general not possible, but Landi Degl'Innocenti & Landi Deglinnocenti (1985) give a formal solution:

$$\boldsymbol{I}(z) = \int_{z_0}^{z} \mathsf{O}(z,z')\mathsf{K}(z')\boldsymbol{S}(z')\,dz' + \mathsf{O}(z,z_0)\boldsymbol{I}(z_0)\,. \tag{2.26}$$

The attenuation operator $\mathsf{O}(z,z')$, a 4×4 matrix, fulfills the differential equation

$$\frac{d}{dz}\mathsf{O}(z,z') = -\mathsf{K}(z)\mathsf{O}(z,z') \tag{2.27}$$

and the condition

$$\frac{d}{dz}\mathsf{O}(z,z) = \mathsf{1} \quad , \tag{2.28}$$

where $\mathsf{1}$ is the identity matrix. For a semi-infinite atmosphere with $z_0 \rightarrow -\infty$, the Stokes vector is

$$\boldsymbol{I}(z) = \int_{-\infty}^{z} \mathsf{O}(z,z')\mathsf{K}(z')\boldsymbol{S}(z')\,dz' \quad , \tag{2.29}$$

where O is the evolution operator. If the absorption matrix K is constant, this operator can be written as

$$\mathsf{O}(z,z') = e^{-\mathsf{K}(z-z')} \tag{2.30}$$

and describes the attenuation of the Stokes vector.

2.4 Formal disk integration

The light we observe from a star, appearing as a point-like source, can be represented as the integral of local Stokes profiles emerging from each point $M(\eta, \rho)$ on the visible hemisphere, where η and ρ are the longitude and latitude, respectively. The individual local spectra are shifted in wavelength due to the Doppler effect, so the residual intensity can be written as

$$\boldsymbol{R}_{syn}(\lambda) = \frac{\iint \boldsymbol{I}_l[M, \theta, \lambda + \Delta\lambda_D] \cos\theta \, dM}{\iint I_c[M, \theta] \cos\theta \, dM} \, , \tag{2.31}$$

where I_c are continuum intensities and $\boldsymbol{I}_l$ is a four component vector representing the local unpolarized line intensity, as well as linear and circular polarized intensities (Stokes IQUV), represented by Eq. (2.29)

3 Stokes profile synthesis

A detailed analysis and study of stellar magnetic fields requires the synthesis of Stokes profiles and thus the precise solution of the polarized radiative transfer calculation. This implies a profound knowledge of atomic data, model atmospheres, line broadening mechanisms, as well as continuous and line absorption. The synthesis of local line profiles and their disk integration to form rotationally broadened Stokes profiles according to a stellar model is referred to collectively as *forward modeling*. To deal with the computationally expensive forward calculations, in case of DI, one usually makes use of pre-calculated tables of local line profiles. Such a table must cover a reasonable number of atmospheric models (effective temperatures) and line of sights, in order to yield a good approximation, when interpolating between the pre-tabulated profiles.

The look-up tables we employ in pure DI considerations, are sampled in $\cos\theta$, where θ is the line-of-sight angle, with a step width of 0.0125. With the temperature ranging from 3500 K to 7500 K (in 250 K steps) the table already contains 1377 local profiles. For ZDI such a table would have to comprise in addition the three magnetic field components. However, a proper sampling of the parameters would make a pre-calculated table unacceptable large. To provide ZDI with a fast synthesis method we developed an approximation method for the polarized radiative transfer, based on Artificial Neural Networks (ANNs), which are trained on the conventional radiative transfer method to find an approximation of the mapping between atmospheric parameters and the corresponding local Stokes profiles.

This chapter gives first a short introduction into the polarized radiative transfer (RT) module used throughout this work and assesses its performance. In the second part, the ANN approach is introduced and compared to the full numerical RT calculation.

3.1 Numerical solution of the polarized radiative transfer

In order to numerically solve the polarized radiative transfer equation under local thermodynamic equilibrium (LTE), continuous opacities are calculated, originating

from routines written by Wittmann (1974), with contributions from free-free and bound-free transitions of H^-, H I, He I, He^-, H_2^-, and H^+ as well as for neutral elements C, Na, and Mg. Scattering contributions are Thomson scattering by free electrons and Rayleigh scattering by neutral hydrogen, molecular hydrogen, and neutral helium.

Concerning the damping term a, given by Eq. (2.22), radiation, Stark, and Van der Waals damping are taken into account. Damping parameters for the given spectral line are extracted from the VALD atomic line database (Piskunov et al. 1995; Kupka et al. 1999), like all other atomic line data. These are: central wavelength, atomic number, ionization state, excitation energy of lower level, quantum numbers L, S, J for upper and lower level, statistical weight, and oscillator strength. Abundances, ionization energies, and partition functions (calculated according to Bolton 1970 and Aller & Everett 1972) are provided for 83 elements (Wittmann 1974). For the calculation of Zeeman splitting, LS-coupling (Russel-Saunders coupling) is assumed (see Sect. 2.2). Voigt and Faraday-Voigt functions are evaluated using the rational approximation method of Humlícek (1982). The underlying atmospheres are provided by ATLAS9 (Kurucz 1993) or Phoenix (Hauschildt 1992).

The numerical calculation of the evolution operator (Eq. 2.30) and the solution of the transfer equation is realized by the Diagonal Element Lambda Operator (DELO) method (Rees et al. 1989).

3.2 Disk integration

The previous chapters described the core radiative transfer calculations for the synthesis of local Stokes profiles that is the synthesis of a single pencil of rays. To simulate the observable Stokes profile of a whole stellar disk, a large number of local profiles has to be integrated. For that purpose, the stellar surface is partitioned either into equal area or equal degree segments. In any case, the minimal extension in longitude and latitude is 1°. For each surface segment the projected area, position (longitude, latitude) on the sphere, line-of-sight angle, radial velocity, temperature and local magnetic field components (radial, azimuthal, meridional) are pre-calculated for all rotational phases. In case of an equal degree setup, also the actual area of each surface zone has to be calculated in advance. To allow for a precise disk integration, each segment (*parent-segment*) can again be split into smaller segments (*child-segments*), for which the full radiative transfer calculation is performed. The child-segments carry the same temperature and magnetic field strength as their parent-segment but the other parameters are calculated according to their location and size. This sub-division is useful for the inversion process,

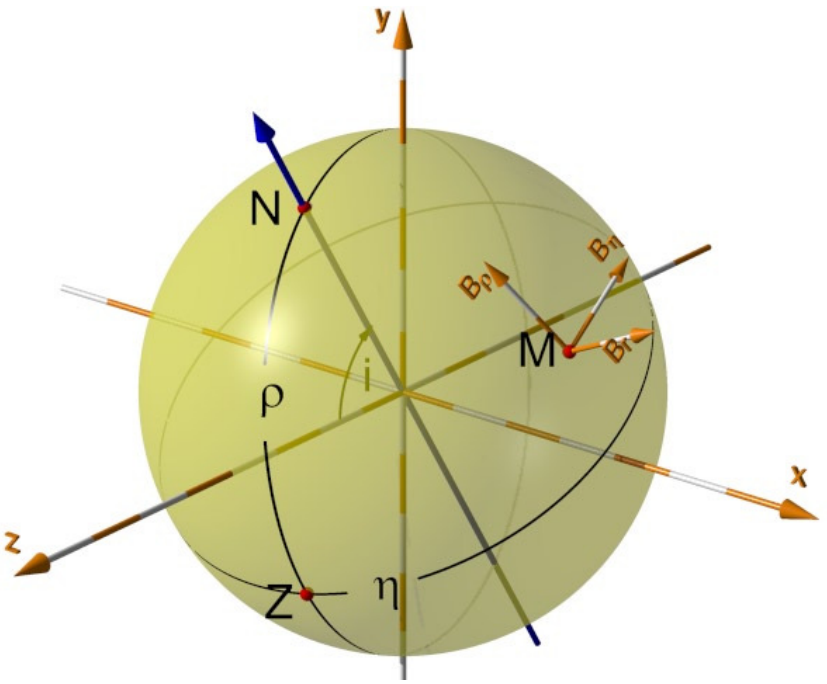

Figure 3.1: Setup of the stellar reference frame, where the z-axis is pointing towards the observer. The vector through the point of origin and N is the rotation axis, inclined about the angle i. For a detailed description see the text.

which is the subject of a later chapter. The inversion, which is restricted in terms of free parameters and thus by the number of surface segments, acts on the parent-segment basis, while the actual radiative transfer is calculated on the much more precise child-segment basis.

A setup of the stellar coordinate system is shown in Figure 3.1, where the stellar sphere is located in the center of a right-handed cartesian coordinate system. The rotation axis is indicated by the vector going through the point of origin and the stellar north pole N. At an inclination of $i = 0$ the observer who is located on the positive z-axis, is looking right on the counter-clockwise rotating north pole. The rotational phase (ϕ) is counted from the yz-plane towards the zero longitude ($\eta = 0°$). Z is the position of the zero longitude η and the zero latitude ρ. Longitudes are counted positive in counter-clockwise direction and negative in clockwise direction, thus ranging from $-180°$ to $+180°$. Latitudes are positive above and negative below the stellar equator and so range from $-90°$ to $+90°$. The magnetic field at any point $M(\eta,\ \rho)$ is specified with respect to a local cartesian coordinate system located at the center of any segment. It is expressed by the field strength B, local field inclination γ_{loc} measured from the positive B_r-axis (see Fig. 3.1), and local field azimuth α_{loc} measured from positive B_ρ-axis towards positive B_η-axis.

The transformation into local meridional B_η, azimuthal B_ρ, and radial B_r field components is given by

$$\boldsymbol{B}_{loc} = \begin{pmatrix} B\sin(\gamma_{loc})\sin(\alpha_{loc}) \\ B\sin(\gamma_{loc})\cos(\alpha_{loc}) \\ B\cos(\gamma_{loc}) \quad , \end{pmatrix}$$

where $\boldsymbol{B}_{loc} = (B_\eta, B_\rho, B_r)^\mathsf{T}$. These components also represent the free parameters in the inversion, which will be introduced in Chap. 4.

To calculate the Stokes profile for each segment, local magnetic field vectors must be further transformed into the observer's coordinate system, so that the inclination and azimuth angles (Fig. 2.1), which enter the radiative transfer equation, can be derived. Local Stokes profiles are then shifted in wavelength domain according to the Doppler velocity of the corresponding segment and weighted by its projected area. Finally all local profiles are summed and normalized by the total continuum intensity, to form the residual intensity given by:

$$\boldsymbol{R}_{\rm syn}(\lambda) = \frac{\sum_M \boldsymbol{I}_l[M, \lambda + \Delta\lambda_D(M)]\ \Delta M}{\sum_M I_c[M]\ \Delta M} \quad , \tag{3.1}$$

where $\Delta\lambda_D$ is the Doppler shift and ΔM the projected area of the surface element specified by $M(\eta,\ \rho)$. Center-to-limb variation is taken into account by adjusting the depth stratification of the atmospheric parameters for each surface segment with respect to the observer reference frame. The surface distribution of temperature and magnetic field can be either described on the basis of individual segments or by a global specification using spherical harmonics.

3.3 Validation

To demonstrate the reliability of our line synthesis code and assess possible errors, we compare it with Cossam, a freely available magnetic radiative transfere code developed by Stift (2000). The comparison study follows the interagreement study of Wade et al. (2001), in which three polarized radiative transfer codes were compared. Among them was Cossam. The other two were, Invers10 (Piskunov 1998) and Zeeman2 (Landstreet 1988; Wade et al. 2001). In this study we want to evaluate the agreement between iMap and Cossam and in doing so also indirectly the agreement with the other two codes.

3.3.1 Principle parameters

As mentioned before, we are particularly interested in the study of solar-type stars. Therefore, the solar ATLAS9 atmosphere (`asun.dat`, Kurucz 1993) became the model of choise. It has an effective temperature $T_{eff} = 5777\,\mathrm{K}$, a surface gravity $\log g = 4.44$ (cm/s^2), solar metallicity, and a micro-turbulence of 1.5 km/s. The

Parameter	Value
λ_0	6173.336 Å
$\log gf$	-2.88
E_l	2.223 eV
E_u	4.231 eV
$\log \gamma_{Rad}$	8.223
$\log \gamma_{Stark}$	-6.194
$\log \gamma_{vdW}$	-7.690
lower term	$^5P_1$
upper term	$^5D_0$
lower Landé	2.50
upper Landé	0.00

Table 3.1: Line data of Fe I 6173, taken from VALD.

spectral line chosen for this comparison was Fe I 6173, with specific parameters taken from VALD (Piskunov et al. 1995; Kupka et al. 1999) and listed in Tab. 3.1.

Continuous opacity For the comparison of the continuous opacities we picked a cool and a hot layer in the model atmosphere to calculate the total opacity and its main constituents in the wavelength range from $\log \lambda = 3.5$ to $\log \lambda = 4.3$ (Å) with both codes. Figure 3.2 shows in the upper panels the total continuous absorption coefficients and in the lower panels its main contributors (bound-free and free-free for H^- and H I, Rayleigh and Thomson scattering). The total continuous opacity differs at maximum for the cool layer by less than 7.5% and for the hot layer by less than 2.5%. The average deviation in the plotted wavelength range is about 1% and about 0.5% for the cool and hot condition, respectively. Like Wade et al. (2001), we also see the maximal deviation at higher wavelengths.

Damping parameters The next comparison regards the contributions to the damping parameter a (Eq. 2.22), which enters the Voigt and Faraday-Voigt functions

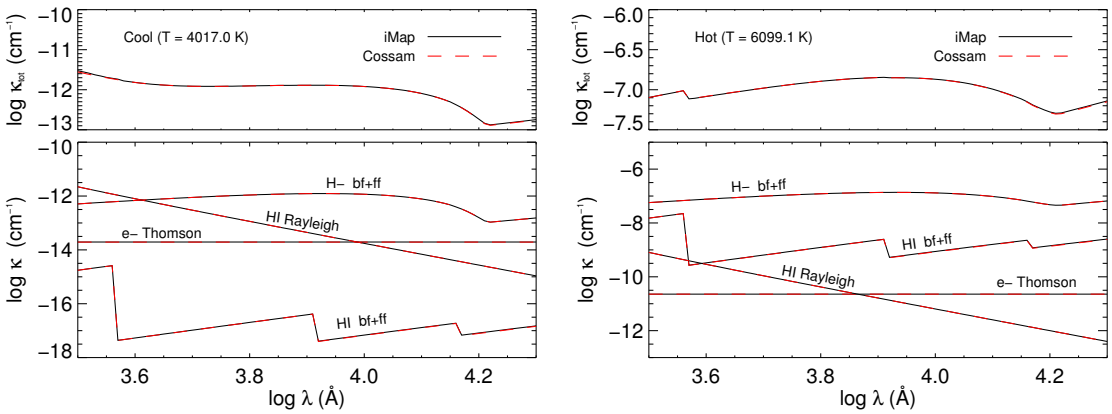

(a) (b)

Figure 3.2: Total continuous absorption coefficient in the two upper panels and contributions from the different sources in the lower panels, calculated by COSSAM (dashed line) and iMap (solid line). The plots on the left (a) are calculated for a cool atmospheric layer (see Tab. 3.2), those on the right (b) for a hot layer.

Parameter		Cool	Hot
ρ_x	(g cm^{-1})	$6.53009050 \times 10^{-03}$	3.63331745
T	(K)	4017.0	6099.1
n_e	(cm^{-3})	$3.140 \times 10^{+10}$	$3.482 \times 10^{+13}$
n_A	(cm^{-3})	$3.225 \times 10^{+14}$	$1.182 \times 10^{+17}$
ρ	(g cm^{-3})	6.975×10^{-10}	2.556×10^{-07}

Table 3.2: Cool and hot conditions in the solar atmosphere

(Eq. 2.20, 2.21). Figure 3.3 shows the Radiation, van der Waals and quadratic Stark broadening as a function of the column mass density. The difference in the mean total damping is less than 0.5%, while the quadratic Stark damping, with a maximum deviation of about 7% is introducing the main part of the difference. However, the maximum deviation occurs around $\log \rho_x = -3$ and thus has only marginal influence. Concerning the essential parameters opacity and damping, the agreement between iMap and COSSAM is comparable to that among COSSAM, INVERS10, and ZEEMAN2, presented by Wade et al. (2001).

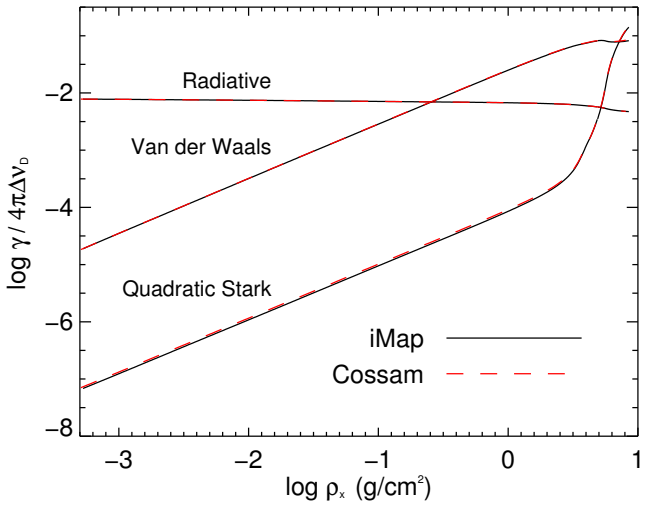

Figure 3.3: Contributions of the radiation, quadratic Stark, and van der Waals damping for the line Fe I 6173.

3.3.2 Local profiles

After probing the agreement of essential physical parameters, we check the final Stokes profile synthesis. This assesses the integration scheme of the RT calculation. Various test calculations for the line Fe I 6173 using the solar Kurucz atmosphere are shown in the following, for the non-magnetic case as well as for the magnetic case with different field strengths.

Zero magnetic field A local Stokes I profile of the line Fe I 6173 was calculated at the center of the stellar disc ($\mu = \cos\theta = 1$). Figure 3.4 shows the result of both codes, with the difference plot in the smaller upper panel. The relative Root Mean Square (RMS) error, with respect to the continuum intensity, is smaller than 0.1%. Again, the agreement is at the same level as the one reported by Wade et al. (2001).

Magnetic field In the magnetic test case, we synthesized local Stokes profiles with field strengths of $B = 0.1,\ 1.0,\ 2.5$ kG. The inclination and azimuth of the magnetic field vector (see Fig. 2.1) was set to 40° and 0°, respectively. Corresponding plots are shown in Fig. 3.5. For the calculation of the relative rms error all data points, where the corresponding Stokes I intensity was 10% of the maximum Stokes I profile depth below continuum level, were considered. The relative rms errors with respect to the full profile amplitudes are listed in Tab. 3.3. The profiles show very good

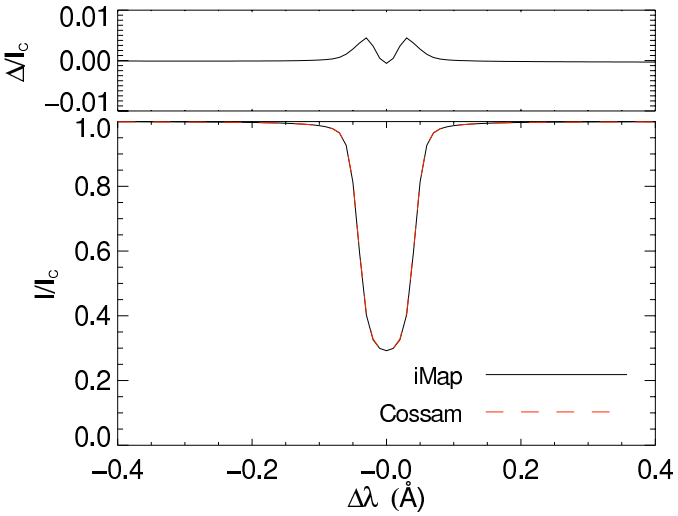

Figure 3.4: Local line profile of the line Fe I 6173 calculated without magnetic field. The difference between the two codes is illustrated in the upper panel.

Field strength	I	V	Q	U
0.1 kG	0.18	0.69	0.53	0.33
1.0 kG	0.19	0.41	1.06	0.98
2.5 kG	0.23	0.60	0.43	0.75

Table 3.3: Relative rms errors with respect to the full profile amplitudes. Those data points, where the corresponding Stokes I intensity was smaller than the maximum Stokes I profile depth, were considered.

agreement and error values are well in the regime of that reported by Wade et al. (2001).

3.4 A fast approximation method

Zeeman-Doppler Imaging, as an iterative optimization method, requires a tremendous number of polarized radiative transfer calculations. To cope with the high computational demands, one usually applies some approximation method. A look-up table, as often used in Doppler Imaging (e.g., Piskunov & Rice 1993; Rice 2002), would become unrealistically large for the required precision.

Another alternative is the weak-field approximation, in which the Voigt and Faraday-Voigt functions (Eq. 2.20 and 2.21) are written as a Taylor expansion. The dif-

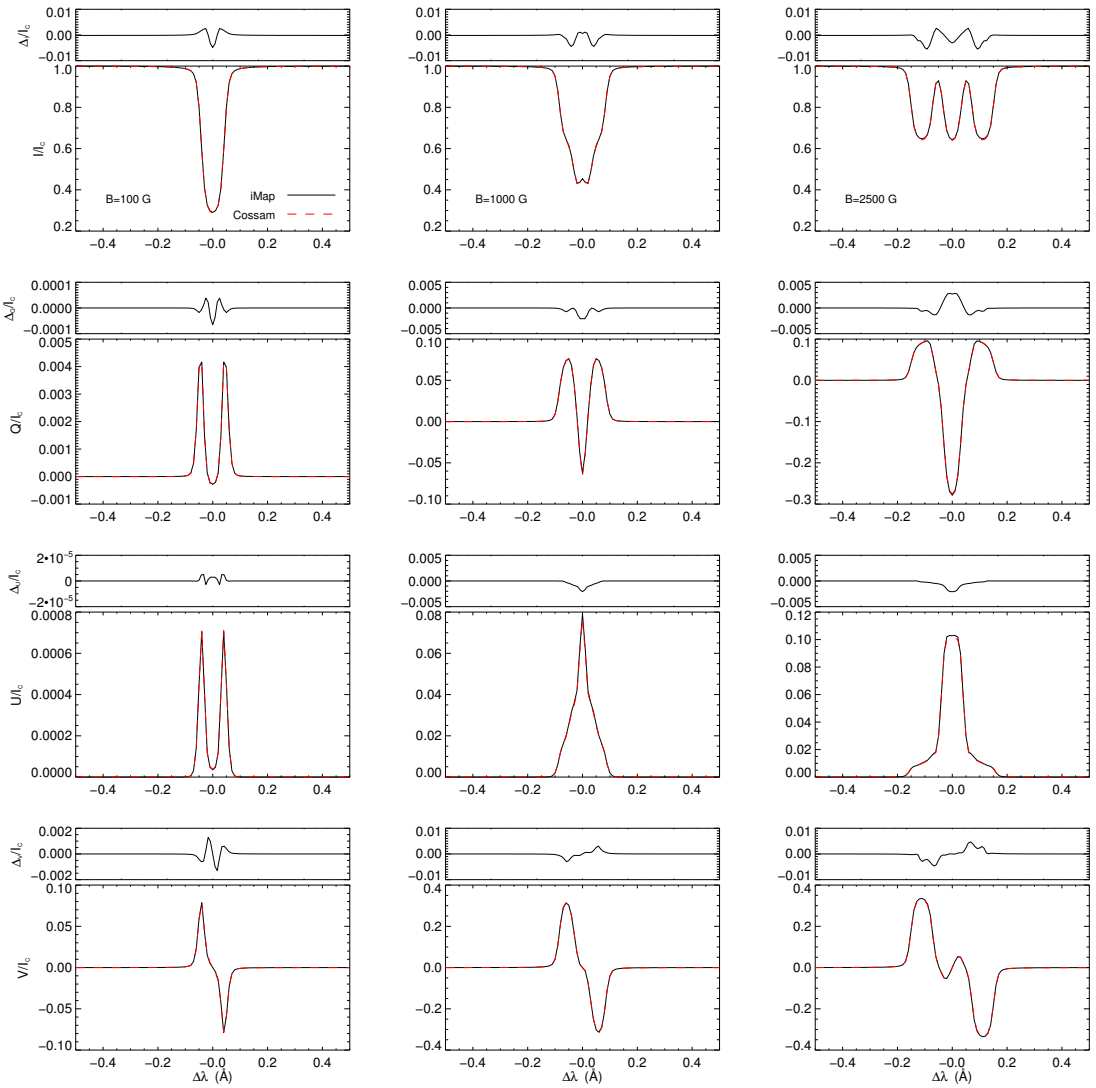

Figure 3.5: Local Stokes profiles of the line Fe I 6173 for a solar Kurucz atmosthere, at a field strength of $0.1, 1, 2.5$ kG. The angle between the magnetic field vector and the line of sight is 40°.

ferent terms can then be identified as the Stokes V, Q, and U profiles. While this is a reasonable assumption for Stokes V with field strengths up to about 1000 G, it is for Stokes Q and U a rather poor approximation. For a detailed discussion of the weak field approximation, see e.g. Landi Degl'Innocenti (1992); Stenflo (1994).

We have developed a fast approximation method, based on the Principal Component Analysis (PCA) and Multi-Layer-Perceptrons (MLPs). The PCA serves here as a dimensionality reduction while the MLPs approximate the radiative

transfer calculation. This method will be described in Sect. 3.4.2, but before a general introduction to Artificial Neural Networks is given according to Bishop (1995).

3.4.1 Artificial Neural Networks

Artificial Neural Networks (ANNs) were originally inspired by the way, the human brain processes information. The operating mode of memory cells (neurons) and their interconnections (synapses) is mathematically modeled by an abstract system of functions and weights. In the course of time, it became an own topic of research and several types of Artificial Neural Networks have been investigated. However, I will focus here on the probably most popular type of ANNs, the so called Multi-Layer-Perceptrons. Their successful application to similar astrophysical problems, such as Stokes profile inversions, was already demonstrated by, e.g., Carroll & Staude (2001) and Socas-Navarro (2005). Neural networks constitute a

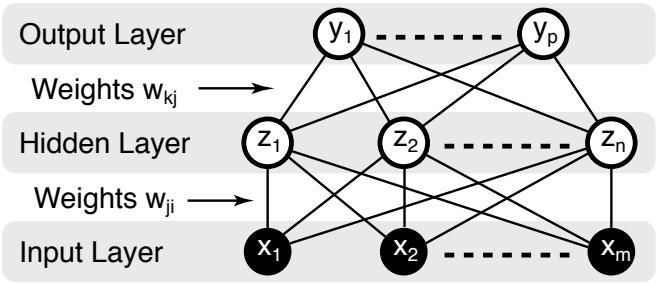

Figure 3.6: Schematic view of a Multi-Layer-Perceptron with m input units and p output units. It has two layers of adaptive weights (the interconnections) and thus one hidden layer with n units.

non-linear functional mapping between a set of input variables and a set of output variables. The basic building blocks are *units*, often also called *cells* or *nodes*, and weighted connections, simply referred to as *weights*. Figure 3.6 shows a schematic representation of such an ANN. An input node simply takes a presented value and transfers it by a weighted connection to any unit in the next hidden layer. Note, that there can be more than one hidden layer. Units in the hidden and output layers first sum all the weighted inputs, and, as a second step, process it by an activation function, which weights the power of the output depending on the sum of the inputs. This is also motivated by biological neurons where the activation function corresponds to a Heaveside step-function, giving only 1 or 0 as an output. This form of activation function can be interesting for classification problems, however, for practical reasons it is useful to have a monotonic and differentiable

function, as will be discussed later. Typically a logistic sigmoid function, given by

$$g(x) = \frac{1}{1 + e^{-(x+\theta)}} \tag{3.2}$$

is chosen. It maps the interval (-∞, ∞) onto (0, 1). The parameter θ is the so called *bias* or sometimes also referred to as threshold. It can be seen as a threshold required to activate a real neuron. Another common type is the hyperbolic tangent

$$g(x) = tanh(x) = \frac{e^x - e^{-x}}{e^x + e^{-x}} \quad , \tag{3.3}$$

having a similar shape as the logistic sigmoid function, but mapping the interval (-∞, ∞) onto $(-1, 1)$.

The mathematical realization of a network as shown in Figure 3.6 is as follows. As a first step, the j-th processing unit in the hidden layer adds up the weighted inputs values x_i to form

$$a_j = \sum_{i=0}^{m} w_{ji}^{(1)} x_i \quad , \tag{3.4}$$

where $w_{ji}^{(1)}$ are the weights between the i-th input node and the j-th hidden node. The $w_{j0}^{(1)}$ is a bias, which is connected to an extra input variable x_0 that is always set equal to 1. The superscript (1) of the weight denotes the number of the weight-layer. The value a_j then enters the activation function g to give the output of the j-th unit of the hidden layer:

$$z_j = g(a_j) \quad , \tag{3.5}$$

where g is the activation function. Throughout this work, the sigmoid function, as shown in Eq. (3.2) was used. The outputs z_i of the hidden layer are then processed in the same way as the inputs x_i. They are weighted and added up, following the equation

$$a_k = \sum_{j=0}^{n} w_{kj}^{(2)} z_j \quad , \tag{3.6}$$

where a_k is the input to the k-th output node. As a last step, this weighted linear combinations are transformed by the activation functions to the p final outputs given by:

$$y_k = \tilde{g}(a_k) \quad . \tag{3.7}$$

Note that the activation function $\tilde{g}$ can be different from g in the hidden layer. The equations (3.4) - (3.7) can be summarized in a compact equation, representing the network shown in Fig. 3.6. This looks like:

$$y_k = \tilde{g}\left(\sum_{j=0}^{n} w_{kj}^{(2)} g\left(\sum_{i=0}^{m} w_{ji}^{(1)} x_i\right)\right) \quad . \tag{3.8}$$

Following the notation of Bishop (1995), the presented network is called a *two-layer* notwork, indicating that there are two layers of adaptive weights. Some other authors specify the network structure by the number of layers, containing hidden units. Equation (3.8) can be easily extended to contain more layers of weights. It can be shown, that a network with two layers of weights allows to approximate any continuous functional mapping (Bishop 1995).

The weights are the essential part of a network function, since they finally cover the dependance between the input and the output data set of a given model. In the training process of a network, the weights are adjusted, given a representative data set of inputs $\boldsymbol{x}$ and known corresponding outputs $\boldsymbol{t}$, which are calculated according to the model the network is supposed to adopt. This involves some error function, which is minimized with respect to weights and bias. The most commonly used is the sum-of-square error function. Minimizing it can be done in several ways, one of the most simple methods for the minimization is the gradient descent method. Several algorithms for the training of artificial networks exist, but I will concentrate on only one common method, the method also used in this work. This is the so-called back-propagation algorithm.

The back-propagation algorithm is an iterative optimization process. It achieves the minimization of the total error over all training data by adjusting the adaptive weights successively in each (weight) layer, starting from the one next to the output layer and progressing towards the input layer. The error is propagated "backwards" through the network, thus its name. This is where the differentiability of the activation function (Eq. 3.2) comes into play, because the error minimization is based on gradient decent method, which involves the derivation of the sum-of-squares error function of the network, given by

$$E = \frac{1}{2} \sum_{n}^{N} \sum_{k}^{p} \left(y_k(\boldsymbol{x^n}) - t_k^n \right)^2 \quad , \tag{3.9}$$

where t_k^n are the n samples of the training data set. The gradient has the form

$$\nabla E(\boldsymbol{w}) = \left(\frac{\partial E(\boldsymbol{x})}{\partial w_1}, \cdots, \frac{\partial E(\boldsymbol{x})}{\partial w_q} \right)^{\mathsf{T}} \quad . \tag{3.10}$$

The distinctive feature of the back propagation algorithm is that it provides an efficient way to calculate the derivatives of the error function with respect to the weights.

Once the network is successfully trained, which means the error converged to an appropriate small value, the weights are fixed. The network now adopted the functional mapping between the input and the target data, and can be applied to unknown input data, that is within the same parameter range as the training data, to calculate the outputs.

3.4.2 PCA-MLP synthesis method

A representative data set, used for the training of the MLP's consisted typically of 20000 local Stokes profiles, randomly generated with the previously described polarized radiative transfer code, in the continuous parameter range given in Tab. 3.4. Same applies for the independent validation data set consisting of 13000 pro-

$$\begin{array}{rcccl} 4500\text{ K} & < & T_{eff} & < & 6500\text{ K} \\ 0^\circ & < & \theta_{loc} & < & 90^\circ \\ 0\text{ G} & < & B_{loc} & < & 2500\text{ G} \\ 0^\circ & < & \gamma_{loc} & < & 180^\circ \\ 0^\circ & < & \phi_{loc} & < & 180^\circ \quad . \end{array}$$

Table 3.4: Parameter range of the training data set. This is also the range of unknown parameters for which Stokes profiles shall be calculated.

files. The other parameters, characterizing the atmosphere were kept fixed. These static parameters are the abundance ($\epsilon_{Fe} = -4.54$), surface gravity ($\log g = 4.0$), micro-turbulence ($v_{mic} = 2.0\,\mathrm{km/s}$), and macro-turbulence ($v_{mac} = 2.0\mathrm{km/s}$). In principle they could be incorporated into the network structure as further free parameters, but not to further increase the complexitiy of the network model and its training, they were left out and set to a static value.

The calculated Stokes profiles are sampled within a 4 Å wide window with a step size of 10 mÅ, resulting in 401 data points. In principle, it is possible to directly map the raw input data onto the raw required output data (in the training also named as target data), but in practice, it is often useful to pre-process the input data and post-process the output data. Even a smaller spectral window, or a more coarse wavelength sampling, would result in a unfeasible large network topology, if these *raw* profiles were presented to the network. Therefore, the spectra were processed by a Principal Component Analysis (PCA), also known as Karhunen-Loève expansion (Bishop 1995). For the training, the inverse of the post-processing has to be applied to the target data. By applying the PCA method, the whole training data set is decomposed into their respective eigenspectra and each local profile is expressed in terms of principal components. The number of principal components that were used for representation of the profiles, was chosen in such a way that the relative RMS error introduced by the dimensionality reduction was smaller then 10^{-5}. This resulted typically in 9-15 principal components, which were the known outputs in the training process. Figure 3.7 illustrates exemplary the first four eigenvectors for Stokes I and V. The input of the networks consists of a combination of the parameters temperature, line of sight, as well as field strength, inclination, and azimuth, depending on the Stokes profile it is trained on, and the task (DI/ZDI) it is used for. In case of Stokes I, for example, it is only the temperature and line of

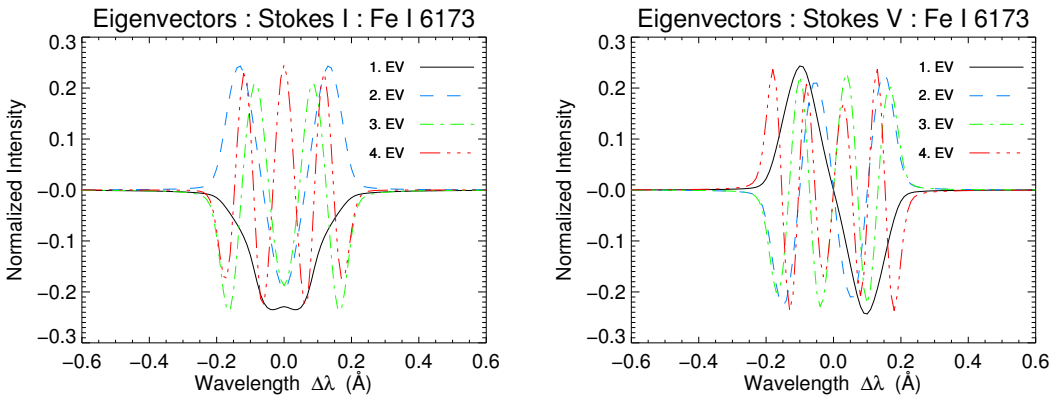

Figure 3.7: First four eigenvectors (principal components) resulting from the PCA of the Stokes I and V training data set for the spectral line Fe I 6173.

sight angle for DI, while for ZDI, also the three components of the magnetic field are required.

Beside the the dimensionality reduction of the Stokes profiles, also a pre-processing was applied, which consisted of the normalization of the input parameters. Of course an identical pre-processing as used in the training must be applied to the input data of the readily trained network.

Having transformed the input and target data, the network topology has to be set up. The neural networks used throughout this work were realized with the neural network modeler *Stuttgart Neural Network Simulator* (SNNS[1]). It has various network types, activation functions, and training algorithms implemented.

No strict rule for the dimensioning of MLPs exists. On one hand the number of weights must be large enough to map the complexity of the given model, on the other hand, the number should not be too large, otherwise the training is unnecessarily hampered. The number of inputs for the Stokes I, V, Q, and U networks are the 5 parameters temperature, line-of-sight, field strength, field inclination, field azimuth and for the continuum network the 2 parameters temperature and line-of-sight. The outputs are given by the number of principal components.

The number of outputs arises from the requirement, that the error, induced by the limited number of principal components, is smaller than 10^{-5}. Setting up hidden layers and weights therein is a tradeoff between achieving a good training error and keeping the net small enough so that the training process becomes not too CPU intense. Initital networks, trained on the whole parameter range as specified before,

[1]SNNS can be obtained from http://www.ra.cs.uni-tuebingen.de/SNNS/

resulted in a poor reproduction at low field strengths. Therefore, we separated the sampling into weak field (0-250 G) and strong field networks (250-2500 G). After testing various network topologies with different numbers of hidden layers and units therein, we found sufficiently good network setups. The final net topology is abbreviated as 'Number of inputs-...Number of weights in the hidden layers...-Number of outputs' and looks for the weak field MLPs as follows. Stokes I: 5-55-50-49-9, Stokes Q: 5-60-65-50-9, Stokes U: 5-80-60-50-9, Stokes V: 5-55-50-49-9, Continuum: 2-10-5-1. For the strong field networks: Stokes I: 5-55-50-49-8, Stokes Q: 5-60-65-50-8, Stokes U: 5-60-65-50-8, Stokes V: 5-55-88-8, Continuum: 2-10-5-1.

3.4.3 Validation - local profiles

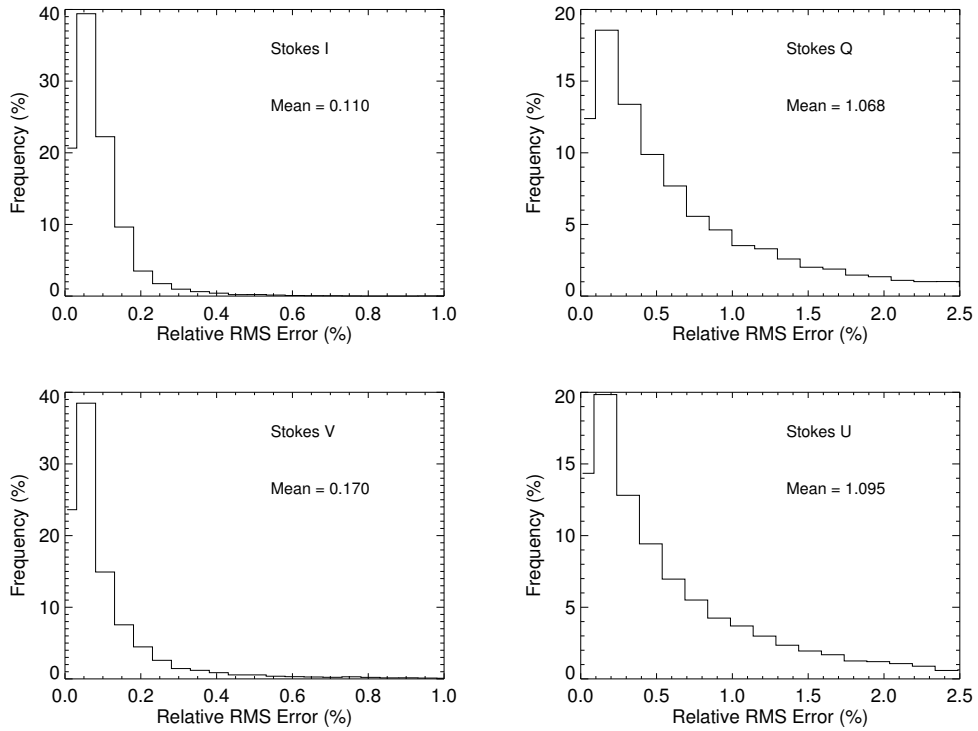

Figure 3.8: Histograms showing the relative rms error distribution for the 13000 local Stokes profiles in a validation data set, independnt from the training data set.

To asses the goodness of the approximation method, we compared it with the conventional polarized RT calculation and estimated the errors of the local Stokes profile calculation as well as of the disk integrated calculation. The left column of Fig. 3.8 shows the distribution of the relative rms errors for a test data set that

is independent from the training data. Stokes I and V show very good agreement

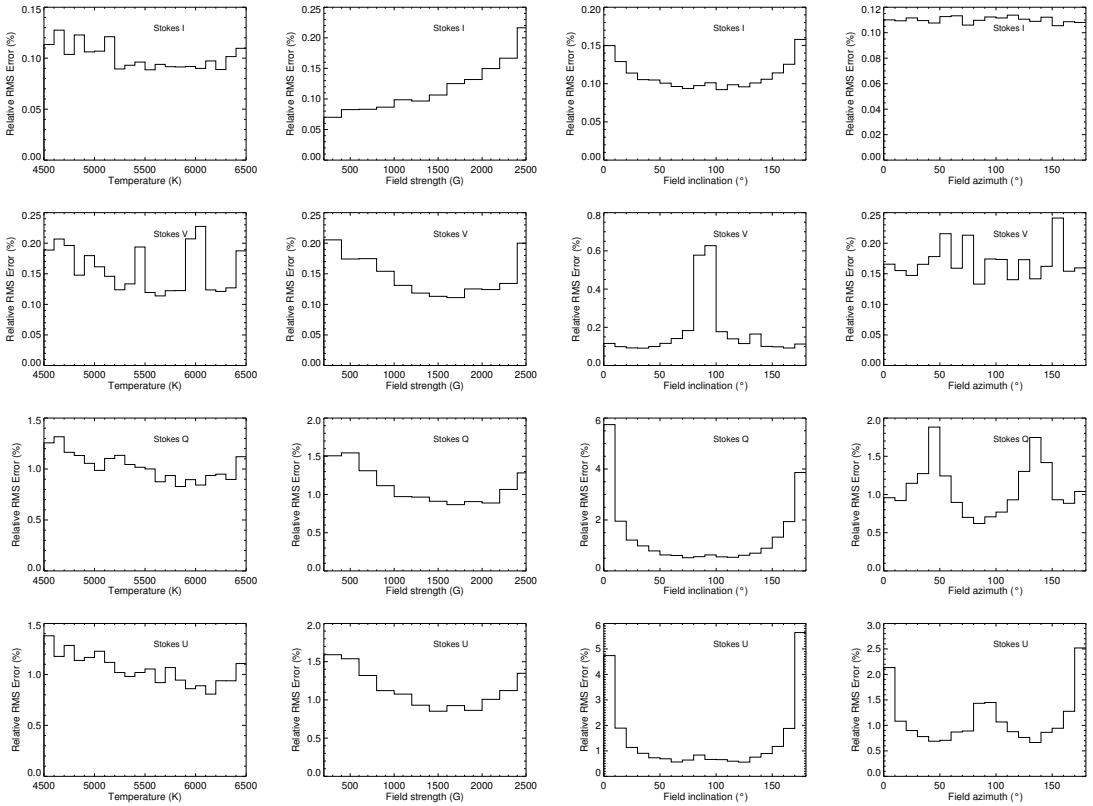

Figure 3.9: Histograms showing the relative rms error distributions as functions of the temperature and magnetic field strength and orientation. The underlying validation data set consisted of 13000 profiles for each Stokes parameter.

with a mean rms error of less then 0.2%. The two linear Stokes components exhibit a larger error due to the more complex dependance on the magnetic field and line of sight angle, but with a value of about 1% their agreement is remarkably good.

The plots in Fig. 3.9 show the relative rms errors over four individual atmospheric parameters. Considering Stokes I (first row, Fig. 3.9), the distribution of the temperature and magnetic field azimuth are relatively homogenous. Note however, that the dependnce of Stokes I on the field azimuth is very small. For the field inclination a small increase towards the longitudinal orientation (around 0° and 180°) occurs. This is a border effect of the uniform sampling of the training data in the field inclination range from 0° to 180°. The dependancy on the field strength shows an increase towards higher field strength. Intuitively one would rather expect an decrease, since the splitting of the Zeeman components increases with field strength

and the linear dependance on the field strength over a wide range should make it easier for the MLP to learn the underlying dependance. The contrary behaviour can be explained by the usage of the PCA decomposition of the spectra and not the raw spectra itself. Stokes I profiles with higher field strength (in the Zeeman saturated regime) are represented by higher-order eigenprofiles, which means that the values of higher-order projection coefficients increase and get more important with increasing field strength. A solution would be to increase the number of principal components or to further split the field strength range into subsets and create different networks. However, the maximum error at high field strength is lower than 0.22 % and for our purpose remarkable good. The setup of the MLP's for the Stokes profile synthesis is always a tradeoff between performance and precision and has to be customized to meet the requirements.

In the case of Stokes V, the mean relative rms error is 0.17 %. In the error versus temperature plot we see two peaks at about 5500 K and 6000 K (second row, Fig. 3.9). These can be explained by the accidental accumulation of field inclination angles around 90° in those temperature regions. At that angle we also see a peak in the plot showing the error distribution over the field strength. This reflects the $\cos\gamma$ dependance of Stokes V seen in Eq. (2.17). The signal around 90° gets very small and therefore the relative error gets high, even though the absolute error stays small. In the error versus field strength plot a slight increase towards small field strength is present, which is due to increasing signal that is more difficult to disentangle from effects like temperature and field strength. At higher field strength we are again facing the problem that stronger split spectral lines are predominantly reproduced by higher-order principal components and therefore the reconstruction error increases. Concerning the azimuthal angle, there is no significant change across the plot, as Stokes V is almost independent of the azimuthal angle, except for small magneto-optical effects.

For Stokes Q and U we see similar distributions. The error distribution over temperature as well as over field strength is relatively homogeneous. The slight increase toward small field strength and at high field strength is again (similar to Stokes V) due to the smallness of the signals and the PCA reconstruction, respectively. The plots for the inclination show a large increase at 0° and 180°. This is because of the $\sin\gamma^2$ dependancy (Eq. 2.17) which leads to small signals at these critical angles and therefore to an increase of the relative error. The same applies to the error distribution over the field azimuth which reflects the $\cos 2\chi$ and $\sin 2\chi$ in Eq. (2.17), leading to a small profile amplitude at those angles and therefore to an increase of the relative error. Even though the relative rms error peaks at these critical angles, the overall accuracy is remarkable good.

3.4.4 Validation - disk integrated profiles

As a final test, we also calculated disk integrated spectra with the DELO and the MLP method for two artificial stars. In the first case, the field structure was modeled by means of spherical harmonics and their derivatives with the Legendre parameters $l = 4$ and $m = 3$.

The peak value of the magnetic field strength was set to 1400 G and the rotational velocity was set to $v \sin i = 26$km/s with an inclination of 60°. A setup is shown in Fig. 3.10, where the radial field is color-coded. The plots show again the four Stokes profiles in the larger panels with the conventional RT and the PCA-MLP method, calculated for the Fe I 6173 line at a temperature of 5000 K (Kurucz atmosphere). In the smaller upper panels the deviation plots are shown. The synthetic spectra show a very good agreement that can be summarized again by the relative rms errors of 0.09% for Stokes I, 0.18% for the Stokes V profiles and 0.36% and 0.72% for Stokes Q, and Stokes U, respectively.

In the second test case a two-spot configuration where also the spot and photospheric temperature varied, was set up. The two spots, 120° apart from each other, with one spot close to the stellar equator and the other one near the pole comprised radial magnetic fields of 1500 G with opposite polarities. Spot temperatures were set to 4500 K in contrast to the 5500 K hot photosphere. An image of the synthetic star is shown in Fig. 3.11, where the temperature is color-coded and the field lines are represented by blue lines for positive and red lines for negative polarity. Relative rms errors have the order similar to those in the previous test calculation. The numerical values are 0.12% for the Stokes I profiles, 0.37% for Stokes V, 0.44% for Stokes Q and 0.43% for Stokes U.

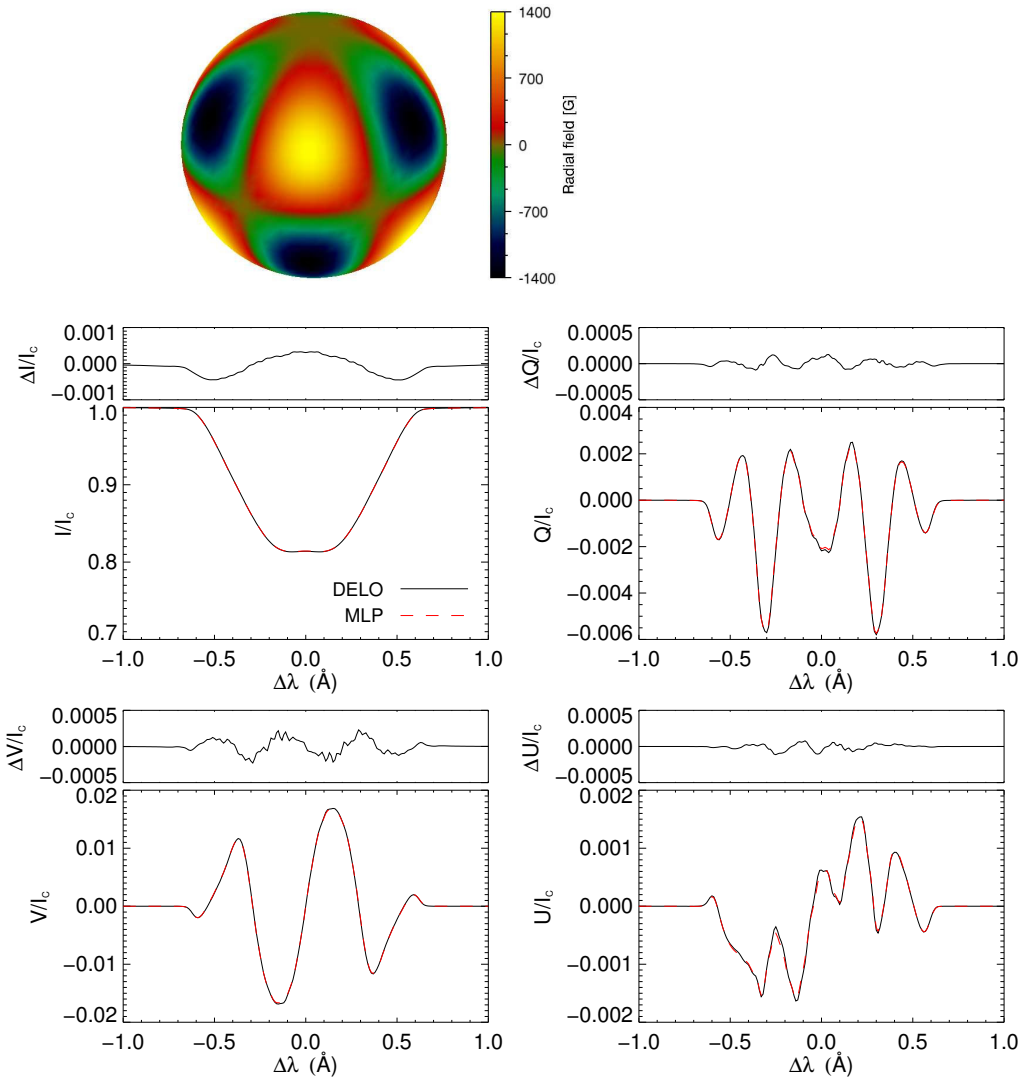

Figure 3.10: Disk integrated Stokes profiles for a global magnetic field setup (modeled by spherical harmonics) calculated by the conventional RT (black straight line) and the PCA-MLP (red dashed line) method. The smaller upper panels show the differences and the corresponding relative rms error. The top sphere shows the distribution of the radial magnetic field component.

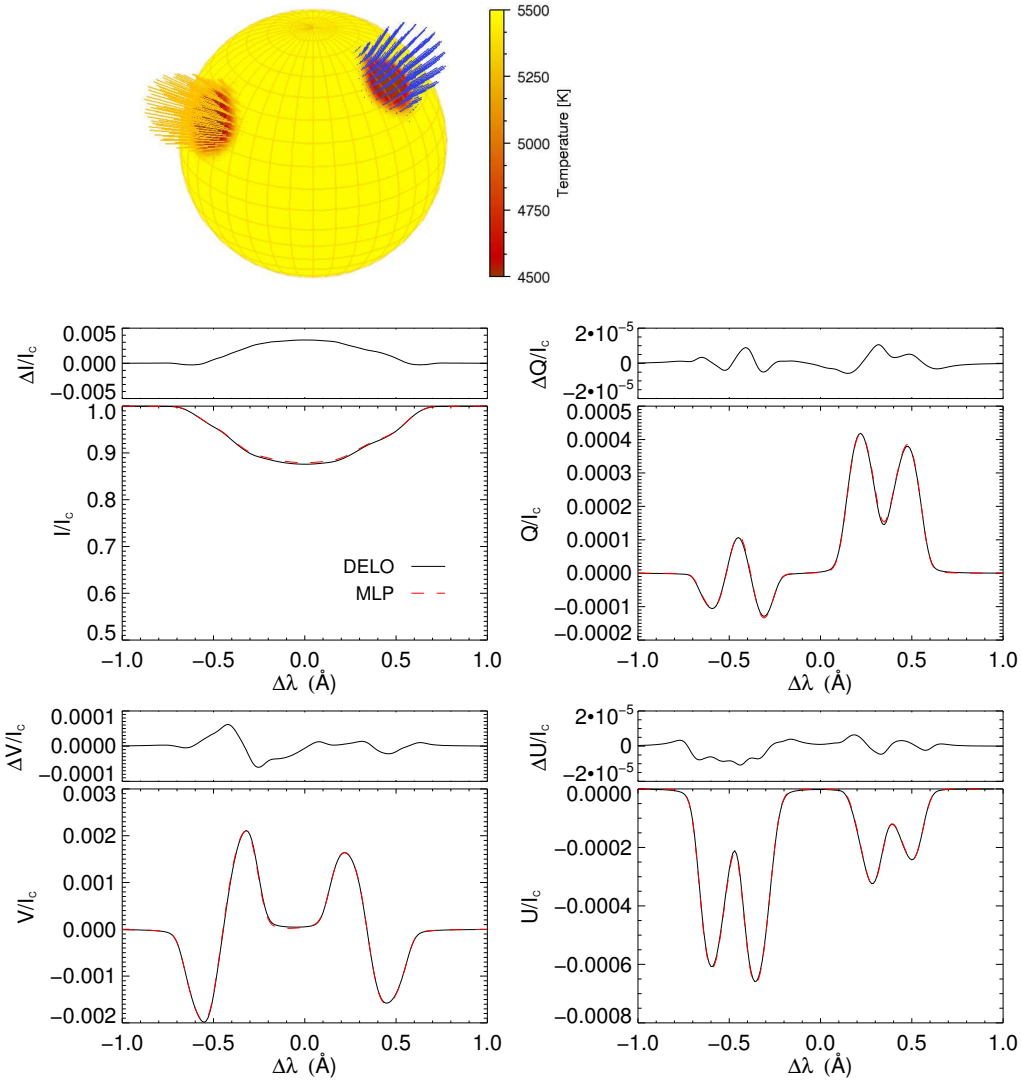

Figure 3.11: Disk integrated Stokes profiles for a two spot configuration calculated by the conventional RT (black straight line) and the PCA-MLP (red dashed line) method. The smaller upper panels show the differences and the corresponding relative rms error. The top image shows the two spot configuration where the temperature is color coded. The radial magnetic field is represented by the yellow (positive) and blue (negative) field lines.

4 Zeeman-Doppler Imaging

Summary In this chapter we describe a new Zeeman-Doppler Imaging scheme, which we have developed particularly with regard to the diagnosis and analysis of magnetic fields of active late-type stars. It is able to make use of all four Stokes components and allows for the reconstruction of an arbitrary temperature and magnetic field surface distribution. The inversion is based on the polarized radiative transfer calculation described in the previous chapter and makes use of a maximum entropy regularized conjugate gradient method. To asses the reliability and potential of the code, we have performed various test inversions of synthetic stellar Stokes profiles.

4.1 Principles and requirements

Zeeman-Doppler Imaging (ZDI) is an extension of the Doppler Imaging (DI) technique (e.g., Vogt & Penrod 1983; Rice et al. 1989; Piskunov & Rice 1993; Rice & Strassmeier 2000). While DI aims for the reconstruction of a temperature or abundance surface distribution, based on rotationally broadened absorption line profiles (Stokes I), ZDI pursues to reconstruct magnetic field maps utilizing polarization signatures in terms of rotationally modulated Stokes V/Q/U profiles (see Sect. 2.1).

The use of intensity line profiles for the mapping of stellar abundance distributions was first suggested by Deutsch (1958). Based on that, the use of polarimetric measurements for the magnetic field surface mapping was proposed by Semel (1989). A first implementation in the from of a numerical inversion was then presented by Brown et al. (1991).

The principle of Doppler Imaging relies on the fact that spots on a stellar surface, arising from temperature or abundance variations, leave characteristic distortions in rotationally broadened line profiles. This is because the line and continuum intensities originating from the spot-region are partly suppressed, relative to the non-spotted regions. Resultantly it appears a distortion in the normalized absorption profile at the Doppler shift, corresponding to the spot position.

There exists a one-to-one correlation between the spot position on the stellar surface and the wavelength position in the corresponding line profile, as illustrated in Fig. 4.1.

In a disk integrated line profile of a certain rotation phase, the wavelength position of a bump gives the distance from the rotational axis of the corresponding spot on the stellar disk. Profiles of different rotation phases thus let derive the longitudinal position of a spot. The behavior of the bump with time, assuming that there are many spectra at different rotation phases during a full rotation period, sets additional constrains to derive the latitudinal position. A spot, close to the visible pole, has an impact on most of the profiles and the corresponding distortion stays close to the line center. Contrary, a spot near the stellar equator results in a bump, moving all the way from the blue to the red wing in successive profiles, assuming anti-clockwise rotation, but is only visible in about half of the rotation period. Thus, by taking a time series during a full rotation period, a complete 2D surface map can be reconstructed. However, it is also obvious that, if the rotational axis coincides with the line of sight (LOS; $i = 0°$), there is no resulting line-of-sight (LOS) velocity and therefore no DI/ZDI possible. On the other hand, if $i = 90°$, there is a north-south ambiguity. No statement about the hemisphere at which a surface element is located can be made. So, the inclination should be at some intermediate stage.

In the same way, magnetic spots and their polarization signatures, expressed by the Stokes vector (see Sect. 2.1), are affected by rotation. Besides radiative transfer effects also the orientation of magnetic fields influences the polarization signals. As a magnetic region crosses the stellar disc, say from left to right for a counter-clockwise rotation, the polarization signature appears at increasing wavelengths in successive profiles and lets derive longitude and latitude of the active region. Additionally, the field orientation, with respect to the observer, changes, as the star rotates. This results in varying shapes in the circular and linear polarized Stokes profiles, as it is qualitatively illustrated in Fig. 4.1. In this example, both spots feature a lower temperature than the quiet atmosphere and exhibit a purely radial magnetic field of equal strength, but opposite polarity. The Stokes profiles of the three rotation phases reflect the correlation between amplitudes and field orientation, described by the angles γ (field inclination relative to the observer) and χ (field azimuth relative to the observer) in Eq. (2.17). In fact, Eq. (2.17) applies to local profiles, but since we have a not to large spot with homogeneous field orientation, this consideration approximately holds also here.

Let us have a look on the Stokes profiles in Fig. 4.1. From Stokes V of the first rotation phase it can be inferred that the two spots must have opposite polarity, because the signal corresponding to one spot possesses the opposite sign of the signal corresponding to the other spot. Furthermore, from the $\cos\gamma$ dependence of ϕ_V and

ϕ'_V in Eqs. (2.17), where γ is the field inclination with respect to the observer, it can be inferred that the Stokes V signal becomes smallest, if the field vector is perpendicular oriented to the observer ($\gamma = 90°$). This is roughly the case for the low latitude spot at rotation phase 0° and for the high latitude spot at rotation phase 60°. If the field vector is aligned with the line-of-sight $\gamma = 0°$, the Stokes V signal becomes maximal. This is particularly distinct for the low latitude spot in the last rotation phase. These simple considerations roughly point out to a more or less radially oriented field, at least in the low latitude spot.

The behavior of Stokes Q and U is more complex, since they depend not only on the field inclination via $\sin^2\gamma$, but also on the field azimuth via $\cos 2\chi$ and $\sin 2\chi$, respectively. In first place it can be stated that Stokes Q and U become smaller the more the field vector coincides with the line-of-sight. Further, the two components tend to become larger, the more the field vector is inclined with respect to the line-of-sight. However, at the same time, Stokes Q dissolves, due to the $\sin^2\gamma$ dependence, at field azimuth angles of $45°, 135°, 225°, \ldots$ and tends to become larger at $0°, 90°, 180°, \ldots$. Contrary, Stokes U dissolves at field azimuth angles of $0°, 90°, 180°, \ldots$ and tends to become larger, where Stokes Q disappears. Additionally, the signals scale with the projected area of a magnetic region. All this explains for example, why the low latitudinal spot produces a relatively large signal in the first rotation phase compared to the very small signal in the last rotation phase, despite the fact that the projected area lets assume the opposite. It is because of the inclination of the field vectors with respect to the observer. But why is then the Stokes Q signal of the high latitudinal spot in the last rotation phase so small? It is because the field vectors feature an azimuthal orientation where Stokes Q vanishes. The Stokes U signature for this spot is at the same time relatively large.

The discussed illustrative case, is of course a very simplified scenario and is far from any real situation. In reality temperature and magnetic field distributions are much more complex, polarization signals, resulting from bipolar regions, might mutually cancel out, and observational data is distorted by noise. In order to retrieve the complex and localized surface pattern it requires an elaborate inversion method.

A fundamental requirement for DI/ZDI is the rapid rotation of a star, so that the spectral lines are dominated by rotational broadening. The required rotational velocity depends on the line width (full width at half maximum) of the considered spectral lines, but in general the projected equatorial rotation velocity, $v \sin i$, should be at least 20 km s^{-1} (Vogt 1988) for DI to achieve a reasonable surface resolution. But also for slightly slower rotating stars successful DI were performed as for AG Dor with a $v \sin i$ of 17 km/s (Washuettl & Strassmeier 2001). To exemplify, the natural line width (disk integrated line for a non-rotating star) of the Ca I 6439

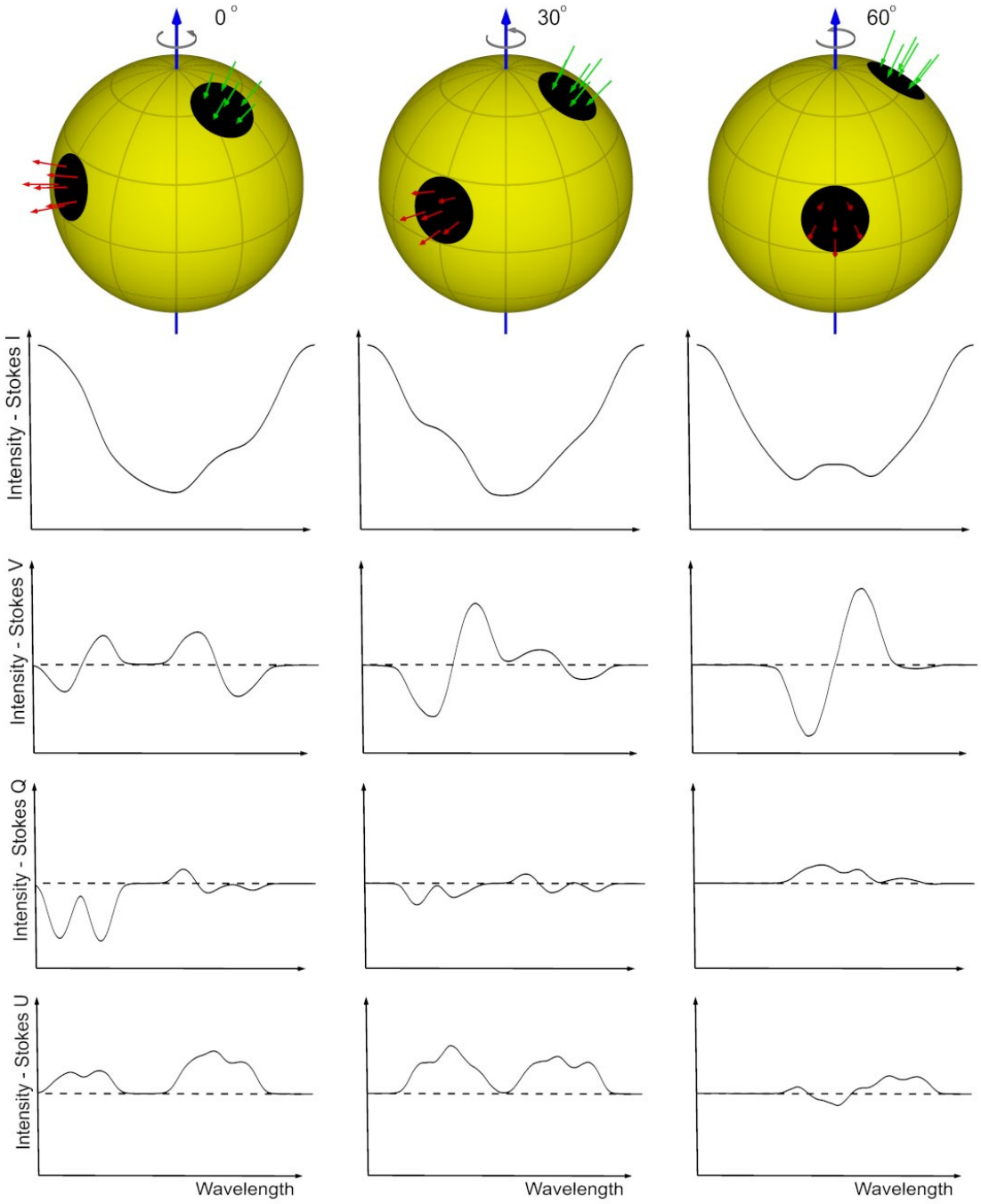

Figure 4.1: Illustration, showing the principle of Zeeman-Doppler Imaging. The two spots on the stellar surface feature a lower temperature than the quiet atmosphere and harbour a radial magnetic field. They leave characteristic fingerprints in the Stokes profiles, seen at three different rotation phases. For a description see the text.

line for an active late type star is already about 0.24 Å ≈ 11 km/s. With increasing velocity, the resolution gets higher, but at the same time the line becomes shallower due to the conservation of line equivalent width. So above 100 km/s it gets very difficult to still detect the signal in the noise. The limiting rotation velocity can be smaller for Zeeman-Doppler Imaging, where it is possible to still derive a meaningful magnetic field map for a star with a projected rotational velocity of a few km/s (Kochukhov & Piskunov 2002). This is because, the relative change in Stokes V, Q, and U between close rotational phases can be large even for slow rotators.

The consideration above on the line width leads also to the requirement of a high spectral resolution. The wavelength sampling across an observed spectral line must be high enough, to be able to instrumentally resolve a spot. Therefore the resolution of the spectrograph must be larger than 35 000. An upper limit is typically set by the limited amount of collectable light. The spectral resolution is virtually in competition with the signal to noise ratio and particularly a problem in polarimetry. Since the degree of polarization (Eq. 2.3) is for solar-type stars usually in the order of a few percent, the polarimetric signatures are rather small. About 10^{-3} for Stokes V but even smaller for Stokes Q/U with 10^{-4}. This requires the signal-to-noise ratio (SNR) to be in the order of several hundred.

4.2 Inversion

Inverse problems in general aim to retrieve some model parameters from observed data and thus represent the counterpart of the forward problem, as illustrated in Fig. 4.2. In our case the forward problem is the Stokes profile synthesis involving the disk integration of local Stokes profiles, computed by polarized radiative transfer calculations. It was explained in Chap. 3. The corresponding inverse problem, summarized under the name Zeeman-Doppler Imaging, is subject of this section.

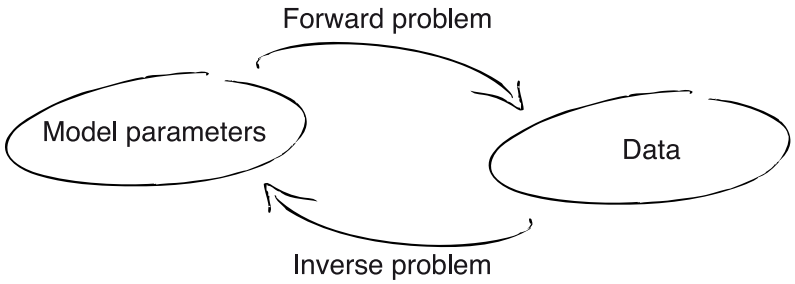

Figure 4.2: Illustration to exemplify the general task of a forward and its inverse problem.

Typically it is differentiated between linear and non-linear inverse problems. A linear inverse problem is the inverse of a linear forward system, which can be written in a discretized form as $d = \mathsf{A}m$, where A is a matrix, mapping the model parameters m to the data d. In the non-linear case, the forward mapping is expressed by $d = A(m)$, where A is a non-linear functional depending on the model parameters m. Therefor it can no longer be considered as a simple linear matrix multiplication. Since the polarized radiative transfer calculation is a non-linear system, we are dealing in case of ZDI with a non-linear inverse problem. For such problems the functional A can not be simply inverted to derive the model parameters from the data. They are typically addressed by an iterative method, which solves the inverse problem numerically.

While the idea of temperature and abundance mapping of stellar surfaces, based on rotationally broadened line profiles, was introduced by Deutsch (1958), it was first formulated as an inverse problem by Khokhlova (1976). A numerical solution was then given by Goncharskii et al. (1977). Semel (1989) proposed to make use of circular polarization profiles to deduce magnetic field distributions on rapidly rotating stars.

The inverse problem of stellar surface imaging works as follows. Starting from an initial temperature and magnetic field distribution, disk integrated Stokes spectra are synthesized and compared with the observed spectra in terms of a discrepancy function. The free parameters $\boldsymbol{x} = (x_1, \ldots, x_n)$ (temperature or abundance for DI, 3-component magnetic field and optionally temperature or abundance for ZDI of each surface segment) are adjusted in order to minimize the discrepancy function

$$E(\boldsymbol{x}) = \sum_k w_k \sum_\phi \sum_\lambda \frac{[R^{\mathrm{obs}}_{k,\lambda,\phi}(\boldsymbol{x}) - R^{\mathrm{syn}}_{k,\lambda,\phi}(\boldsymbol{x})]^2}{\sigma^2_{k,\lambda,\phi}} \quad , \tag{4.1}$$

where the first sum runs over the four Stokes components sampled by the index $k = 1, 2, 3, 4$, the second sum runs over all rotation phases ϕ and the third over all wavelengths λ. The parameters w_k allow to weight individual Stokes components differently according to their relative amplitudes or quality. $R^{\mathrm{obs}}_{k,\lambda,\phi}$ and $R^{\mathrm{syn}}_{k,\lambda,\phi}$ are observed and synthesized Stokes profiles respectively and $\sigma^2_{k,\lambda,\phi}$ are variances, corresponding to the observations. A suitable optimization algorithm carries out the minimization of the discrepancy function by adjusting the free parameters. Due to the large number of free parameters, this is a complex and computing intensive task.

We have implemented a conjugate gradient method for the minimization of the sum-of-squares error function. The conjugate gradient method is a sophisticated gradient descent method in a sense, that the search directions of two consecutive steps are conjugate to each other. It avoids that a minimization in the one step is partly retracted in the following step. This method proved to be reliable and robust even for

a large number of free parameters. In case of an equal degree surface grid with the three components of the magnetic field as the free parameters and a segment size of $5^\circ \times 5^\circ$, there are 7776 unknowns or if the temperature is as well inverted at the same time there are 10368 unknowns. A drawback of this method is its slow convergence when the error function is close to minimum.

A characteristic, which is often inherent to inverse problems is the fact that they are ill-posed. A problem is, according to Jacques Hadamard, called well posed, if 1) a solution exists, 2) the solution is unique and 3) the solution depends continuously on the data. If one of these requirements is not fulfilled, it is called ill-posed. But, a well-posed problem can still be ill-conditioned. This refers to the fact that small changes in the data can result in large changes in the solution. So the continuous dependence of the solution on the data does not necessarily mean that the solution is robust against noise.

Concerning the ill-posedness Piskunov (2005) in fact showed heuristically that an ideal, so purely theoretical, ZDI is actually well posed. In his consideration, radiative transfer was omitted and a continuous wavelength distribution in all four "observed" Stokes components, covering an infinite number of data points as well as an infinite number of rotation phases and being free of noise, was assumed. However, real spectropolarimetric data, the observational basis for ZDI, is in any case discrete in wavelength domain, and possesses a limited number of rotation phases. From the finite number of data points, we aim to reconstruct, in fact, a certain number of free parameters. These are continuous and therefore represent an infinite parameter space.

It can not be stated for sure weather this problem is ill-posed in a strict mathematical form or not. Though, what can be stated is that the numerical implementation is certainly ill-conditioned. Due to numerical instability in terms of discretization and round of errors, more than one solution can be found for given data. This is in particular the case, when an inversion is carried out only on the basis of Stokes I and V. Many possible field configurations can be found, which fit the observations within an equal error or numerical precision. Additionally small perturbations in the data in terms of noise may lead to large changes in the parameter estimates.

The ill-posedness and ill-conditioning is typically accounted for, by imposing additional information in the form of a regularization term Λf, added to the sum of squared error in the discrepancy function in Eq. (4.1), where the regularization parameter $\Lambda > 0$ weights the regularization function f. It applies further constraints, which should present some physical meaning. Another reason that demands a regularization is noise, always present in real observations. In this case, the role of regularization is to stabilize the inversion and prevent it from fitting all the small contaminations. In DI/ZDI basically two common regularization functions exist.

These are Tikhonov and Maximum Entropy regularization, which will be discussed in section 4.3.

Before the discussion of the regularization functional, I will present the optimization algorithm used in this work. One of the simplest methods we can think of is a plain line minimization that makes no assumption about the function and does not make use of gradient information. All free parameters are minimized sequentially with a fixed step-width until a minimum is reached. This was our first implementation on the way to a gradient based algorithm and worked relatively well, considering its simplicity even though it is a very inefficient and time consuming way.

Making use of the gradient, the multidimensional minimization we are dealing with, can be reduced to a one dimensional problem in terms of line search, where the direction is given by the gradient (partial derivatives with respect to the free parameters). This involves a one dimensional minimization sub-algorithm, which consists of a bracketing scheme and Brent's parabolic interpolation method and is explained in the following section.

4.2.1 Brent's method

Finding the minimum of a function $f(x)$ implies finding the point, where the functions derivative becomes zero ($\nabla f(x) = 0$). If an analytical solution does not exist, a numerical root finding algorithm must be applied. To avoid unnecessary, often very computing intensive function evaluations, the algorithm should be efficient in terms of the number of function calculations. Brent's method is such an elaborate root finding algorithm that relies on the bisection method and the parabolic interpolation method (Press et al. 1992).

At first it searches for two points, whose corresponding function values are of opposite sign so that the root lies necessarily between them. Then the function is evaluated at the midpoint and its sign is ascertained. The one bracketing point with the same sign is discarded and the midpoint becomes the new bracketing point of the new smaller interval. This process is repeated, until the interval size reaches a sufficiently small limit. However, by doing so only an extremum is found not necessarily a minimum. To make sure that we are searching for a minimum, a third point is needed, resulting in two intervals. An efficient bracketing algorithm that keeps track of the triplet of points is the *golden section search*. Following this method, a new sectioning point is always chosen in such a way that it falls into the larger of the two intervals and here a fraction of 0.38197 (golden ratio) away from the central point of the triplet (Press et al. 1992).

This method is fairly robust and straight forward, but since each function evaluation is rather computing intensive we want to avoid as much of them as possible. If we presume the function to be quadratic near the minimum, which is in most cases a reasonable assumption, a parabola can be fitted through any three points, and help to find more quickly to the function minimum, because the parabolas minimum should be then very near to the actual function minimum.

Brent's method represents a sophisticated way, to switch between golden section search and parabolic interpolation depending on the behavior of the function. For that purpose, it keeps always track of six function points, the current bracketing triplet described before and the most recent points of function evaluations.

4.2.2 Conjugate Gradient method

One way of minimizing a function $f(x)$ is to take successive gradients $\nabla f(x)$ in the multi dimensional parameter space as the search directions and move along each of them down from one local minimum to the next until the global minimum is reached. This is known as the gradient descent or steepest descent method (Bishop 1995). However in this approach only two consecutive search directions are always perpendicular to each other, but the knowledge about previous directions is not taken into account. This can lead to a partly retraction of a previous step and to very slow convergence. A more sophisticated way of choosing the search directions is given by the conjugate gradient method. Here, successive search directions are not the local negative gradients but rather constructed in such a way, that they are conjugate to each other. The derivation hereafter follows for most part Press et al. (1992). The conjugate gradient method assumes the error function $E(\boldsymbol{x})$ with the free parameters $\boldsymbol{x}$ to be quadratic close to the minimum. The error function can be expressed as a Taylor series:

$$E(\boldsymbol{x}) \approx E_0 - \boldsymbol{b}^\mathsf{T}\boldsymbol{x} + \frac{1}{2}\boldsymbol{x}^\mathsf{T}\mathsf{H}\boldsymbol{x} \tag{4.2}$$

where $\boldsymbol{b}$ is a constant vector and H is a matrix, assumed to be positive definite. The gradient of E is

$$\boldsymbol{g} = \nabla E = \mathsf{H}\boldsymbol{x} - \boldsymbol{b} \tag{4.3}$$

so the error function finds its minimum at $\mathsf{H}\boldsymbol{x} = \boldsymbol{b}$. Starting with an initial vector $\boldsymbol{g}_0$ and an initial search direction $\boldsymbol{d}_0 = -\boldsymbol{g}_0$, the conjugate gradient method successively constructs the vectors

$$\boldsymbol{g}_{i+1} = \boldsymbol{g}_i - \alpha_i \mathsf{H}\boldsymbol{d}_i \qquad \boldsymbol{d}_{i+1} = \boldsymbol{g}_{i+1} + \beta_i \boldsymbol{d}_i \tag{4.4}$$

where α and β are scalars, defined below. The vectors $\boldsymbol{d}$ are supposed to satisfy the conjugacy relation

$$\boldsymbol{d}_i^{\mathsf{T}} \mathsf{H} \boldsymbol{d}_j = 0 \qquad i \neq j \tag{4.5}$$

and the orthogonality relation with the vectors $\boldsymbol{g}$

$$\boldsymbol{g}_i \boldsymbol{d}_j = 0 \tag{4.6}$$

The alley that leads us there can be written as a succession of steps from the points $\boldsymbol{x}_i$ to the points $\boldsymbol{x}_{i+1}$ along the search directions $\boldsymbol{d}_i$ in the form:

$$\boldsymbol{x}_{i+1} = \boldsymbol{x}_i + \alpha_i \boldsymbol{d}_i \quad , \tag{4.7}$$

where the step size is controlled by the parameter α. It is given by

$$\alpha_i = \frac{\boldsymbol{g}_i \boldsymbol{d}_i}{\boldsymbol{d}_i \mathsf{H} \boldsymbol{d}_i} \quad . \tag{4.8}$$

Further it is

$$\beta_i = \frac{\boldsymbol{g}_{i+1} \boldsymbol{g}_{i+1}}{\boldsymbol{g}_i \boldsymbol{g}_i} \quad . \tag{4.9}$$

By successively constructing the search directions $\boldsymbol{d}_i$ as given in Eq. (4.4) and proceeding from the point $\boldsymbol{x}_i$ to $\boldsymbol{x}_{i+1}$ and calculating a new gradient by $\boldsymbol{g}_i = -\nabla E(\boldsymbol{x}_{i+1})$, we can calculate the same gradient as given in Eq. (4.4), but without the knowledge of H.

Moving along the conjugate search directions to a minimum involves the one-dimensional sub-minimization algorithm, which was explained in the previous chapter.

4.3 Regularization

In the minimization task of stellar surface imaging we are dealing with two major problems. One is the ill-posedness of the nonlinear inverse problem and the other is the ill-conditioning, due to the fact that there is alway noise present in the data. This likely gives rise to several local minima in the multidimensional parameter space, in which the iterative minimization algorithm might end up.

The ill-posedness and ill-conditioning is typically accounted for by regularization. In case of least-square error minimization a regularization function superimposes

further constraints on the squared error function, which helps to guide the minimization algorithm through the error space. It is realized by an additional term to the χ^2, so the total error function becomes

$$E = \chi^2 + \lambda R \quad , \tag{4.10}$$

where λ is the so called regularization parameter that controls the weighting of the regularization function. The regularization function should incorporate physical properties of the given object of investigation as a form of prior knowledge. In the present case of ZDI it arises for example the question wether neighboring surface elements can have very different field strengths or not. This can be addressed by some smoothing or contrast-enhancing functional. In astrophysical image processing in general, the Tikhonov and Maximum Entropy method are common forms of regularization. In the absence of noise as in synthetic test cases, regularization has only marginal influence, but usually it can not completely avoided, since we are still facing the problem of incomplete data. The finite number of rotation phases or the wavelength sampling of the spectra allows for ambiguities in the reconstruction process. Also round of errors and the numerical precision make it necessary to apply some regularization.

4.3.1 Maximum Entropy

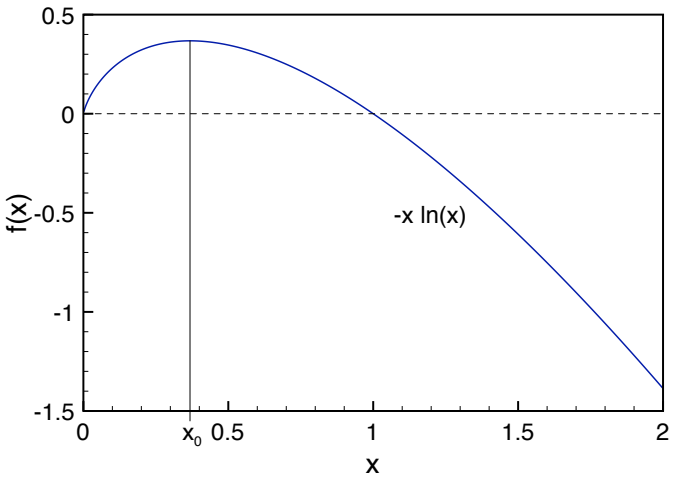

Figure 4.3: Graph of the function $-x \ln x$.

This section gives a short description of the Maximum Entropy method and the particular implementation in our inversion code. A good introduction into the theory of Maximum Entropy and its employment in Astronomy can be found in Narayan & Nityananda (1986).

In the picture of Entropy as a probability measure, the purpose of the Maximum Entropy method is to reconstruct the most probable nonnegative image that is consistent with the data. To get an idea of the properties of the entropy functional typically used in DI and ZDI, it is worth to have a look on its basic form, given by:

$$f(x) = -x \ln x \quad . \tag{4.11}$$

A plot of the function is shown in Fig. 4.3. It becomes clear that, when maximizing Eq. (4.11) or minimizing its negative, the function finds its maximum or minimum respectively at $x_0 = e^{-1}$. This is important for the understanding of the default image in the following consideration. Multiplying the argument of the ln in Eq. (4.11) by e^{-1}/d, where d is a constant yields the equation

$$f(x) = -x \left(\ln \frac{x}{d} - 1 \right) \quad . \tag{4.12}$$

This modified function has the property to become maximal for $x = d$. Thus when maximizing Eq. (4.12) or minimizing its negative respectively, it aspires to the default value d.

We use a regularization function, similar to that formulated by Brown et al. (1991), which is:

$$S = -\sum_i (|P_i| + \alpha) \left[\log \left(\frac{|P_i| + \alpha}{|m_i| + \alpha} \right) - 1 \right] \ , \tag{4.13}$$

where m_i is the default value of the parameter P_i, with i running over all surface elements. The parameters P represent either temperatures or one of the three magnetic field components. The latter can be negative, this is why the absolute values of P and m are taken. To ensure, that the entropy is also defined for zero values of the surface distribution P or the default distribution m, the value of α is set to a small positive number.

In ZDI literature, not much details about the default image, sometimes also named *prior*, can be found, even though effects can be rather drastic, depending on its definition. The small scale variations with great local differences in the magnetic field of late-type stars, require an appropriate regularization scheme. We therefore propose an adaptive local entropy function where the default values m_i are retrieved during the iteration process by the actual mean values of the neighboring segments:

$$S = -\sum_i (|P_i| + \alpha) \log \frac{|P_i| + \alpha}{\frac{1}{k} \sum_{j=0}^{k} \beta(j) |m_j| + \alpha} - 1 \quad . \tag{4.14}$$

The sum in the logarithm runs over the k neighboring segments of segment i and $\beta(j)$ is an extra term which includes a Gaussian weighting. This is particularly useful for the magnetic field components. Imaging having a bipolar spot configuration with the same radial field localized within each spot but of opposite sign. A

entropy function with the mean as the default image would force the field to become zero. Of course the regularization parameter λ still controls the contribution of the entropy function in the error function, but if we create the default image as an average over the local surrounding, we force the field outside of the spot to become zero while we allow the field inside the spot to increase.

4.3.2 Tikhonov

The Tikhonov regularization functional has the form:

$$R = \sum_i \|\nabla P_i\|^2 \quad , \tag{4.15}$$

where P_i are the surface parameters, with the index i running over all surface elements. Tikhonov regularization implies a strong correlation between neighboring surface elements and it aims for the smoothest possible solution that is within the error limits in agreement with the data (Piskunov et al. 1990).

In contrast to Maximum entropy, the Tikhonov functional is also defined for negative parameter values, which has the advantage when the free parameters are constituted by magnetic field components. No special care has to be taken for negative polarity or for zero magnetic field values.

4.4 Practical implementation

Let us keep in mind that the focus of our consideration is on Eq. (4.10) and accordingly Eq.(4.1), which has to be minimized. First we set up the vector $\boldsymbol{R}^{obs}_{k,\lambda,\phi}$, containing the observational data of all rotation phases.

Depending on the inversion task (DI / ZDI) and on the availability of linear polarized components, different Stokes components enter this vector. Present polarimetric observations are usually carried out only in Stokes I and V, due to instrumental limitations or the insufficient SNR in the achievable data. Unfortunately also the observational data of II Peg, presented in a later chapter, contain only Stokes I and V. With the forthcoming polarimeter PEPSI at LBT however, observations in all four Stokes components will become available, even for late type stars with their small degree of polarization. For DI, only Stokes I constitutes $\boldsymbol{R}^{obs}_{k,\lambda,\phi}$. In case of ZDI it is the Stokes V and possibly Stokes Q and U. If a simultaneous temperature and magnetic field inversion is performed, the data vector consists of Stokes I and V or all four Stokes components.

The free variables $\boldsymbol{x}$ in Eq. (4.1) are constituted by the parameters characterizing each segment. These can be temperature for DI, magnetic field components (radial, azimuthal, meridional) for ZDI or temperature and magnetic field components for a simultaneous temperature and magnetic inversion. Technically it is realized in such a way that a parameter vector contains temperatures and all three magnetic field components of all segments. Another vector controls which parameters are free and which are fixed. This enables to easily fix individual parameters within the inversion process. For example one could think of a scenario where in a magnetic inversion it can be useful to allow, for the first few iterations, only the radial component to be varied.

The inversion can be carried out either to obtain simultaneously temperature and magnetic field distributions or to first derive a temperature map and take this as prior knowledge in the magnetic inversion. Initially the temperature of all surface segments is set to the effective temperature, which therefore has to be known or must be estimated before. The magnetic field is uniformly set to zero. In a ZDI however with a preceding DI, the segment temperatures are initialized with the previously retrieved temperature information. Starting with this initial guess, Stokes profiles are synthesized for all rotation phases and the error function is evaluated. The total error is calculated by adding the entropy of the given parameter set to the χ^2 error, weighted by the Lagrange parameter λ. Note that we use here, if not other stated, the entropy function given by Eq. (4.13), where the default image is redetermined after each iteration.

The gradient vector is build up by partial derivatives, calculated by difference quotients, with respect to the free parameters. In case of an equal degree segment set up, each partial derivative has to be weighted by the reciprocal total surface area of the corresponding segment, because the contribution to the total flux is smaller for segments near the pole than for segments close to the equator. If the weighting by the area is not taken into account, the partial derivatives for poleward segments can be very small so that their values can stay almost unchanged and by this mimic some artifacts e.g. a polar spot.

In the first iteration an initial gradient vector is estimated and the error is minimized along its direction, using Brent's one-dimensional sub-minimization algorithm (Sect. 4.2.1). This involves many error-function evaluations for the bracketing of the local minimum, and thus the synthesis of many disk integrated stokes profiles. With the help of this gradient, a new conjugate direction is estimated to proceed to the next local minimum, representing the new segment configuration.

This procedure is repeated, until a sufficient lower limit of the error, a maximum number of iterations or an adequate small relative change between two consecutive iterations (convergence) is reached. The usual stopping criterium is conver-

gence, which is typically achieved after 30 to 50 iterations for DI and 80 to 150 for ZDI.

4.5 Numerical tests

To evaluate the performance of the inversion code and assess the potential of gradient based Zeeman-Doppler Imaging, we have set up an artificial star with known temperature and magnetic field distribution. For this configuration we synthesized corresponding Stokes profiles under ideal (infinite SNR) conditions and inverted them with iMap, in order to reconstruct temperature and magnetic field distributions and compare it with the true images. The chosen specific test cases are supposed to also asses intrinsic limitations of gradient based ZDI methods. The various calculations for differing inversion strategies and settings are referred to as *Test 1, 2, ...*

For all numerical tests, we used Kurucz model atmospheres with solar abundance and $\log g = 4.0$. If not other stated, the spectral line Fe I 6173 with its high effective Landé factor of 2.50 is used for magnetic inversions, while the Ca I 6439 line is used for temperature inversions. The stellar surface grid for all test calculations is $5^\circ \times 5^\circ$.

To quantify the error of the test inversions we use the expression

$$\delta P = \sqrt{\sum_j (w_j \Delta P_j)^2 / \sum_j (w_j)^2} \quad , \tag{4.16}$$

where j runs over all surface elements, w_j represents some weight and ΔP the difference between true and reconstructed parameters. For the error of temperature and field strength, the weights w are simply zero for surface elements, which are completely invisible, due to the star's inclination, and one for all the rest. Thus the resulting error corresponds to the root mean square error (RMS) per surface pixel.

For the error of field orientation, expressed by the azimuthal and meridional angle, weights are again zero for invisible segments but equal to the field strength ($w = B$) for all others. This gives a larger contribution to segments with a higher field strength.

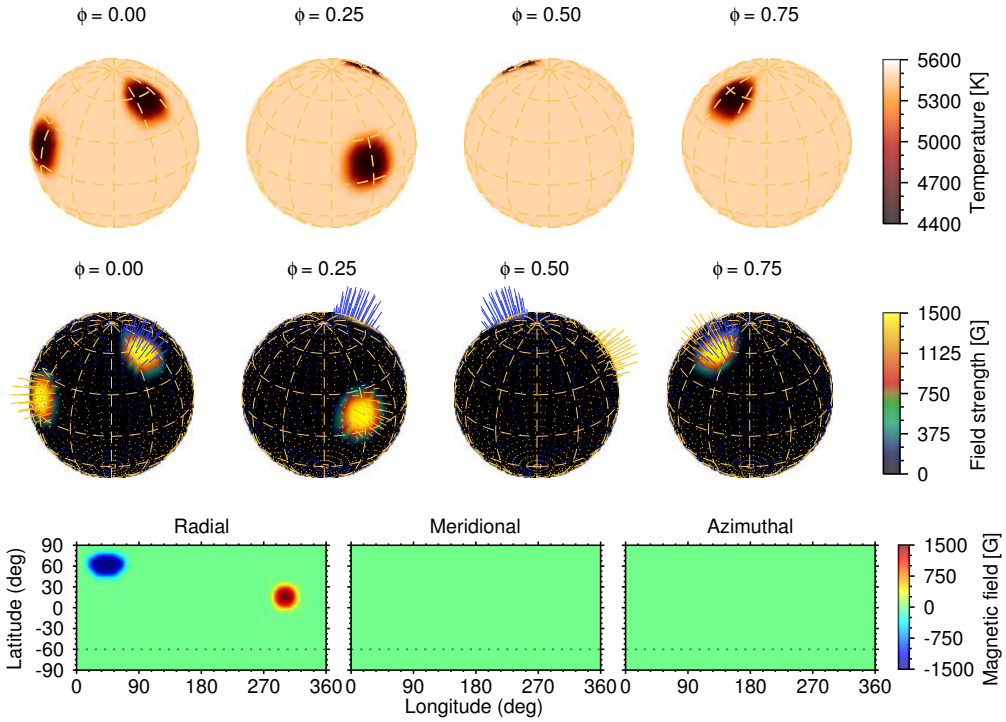

Figure 4.4: True temperature (top row) and magnetic field distribution (middle row) of the two spot configuration of Setup A. The distribution of field strength is shown in the middle row as orthographic maps for four rotation phases, where blue field lines represent a positive and red field lines a negative magnetic field, respectively. Individual magnetic field components are shown as pseudo mercator projections in the bottom row. A purely radial field of opposite polarity is located within the spots.

4.5.1 Stellar setup

The stellar setup consists of a 2-spot configuration with well separated spots, where one spot is located near to the equator and the other close to the pole. They harbour magnetic fields of opposite polarity. While the meridional and azimuthal field components are zero, the radial component has a peak value of 1500 G and −1500 G in the spot centers. To emulate a more realistic spot structure, the field strength declines towards the spot edge as a result of a Gaussian convolution with a FWHM of 2 pixels (surface elements). Same accounts for the temperature with a central spot value of 4500 K and a photospheric temperature of 5500 K. Figure 4.4 shows the setup of temperature and magnetic field distribution for this test case. Synthetic Stokes profiles were calculated with a micro-turbulence $v_{mic} = 2$ km/s and a macro-turbulence $v_{mac} = 1$ km/s. The projected rotational velocity is $v \sin i = 30$ km/s with an inclination of $i = 60°$. Stellar and atmospheric parameters are input parameters to the inversion and are assumed to be known.

4.5.2 Test 1: using Stokes IVQU and true temperature

In a first test inversion, all four Stokes profiles of the Fe I 6173 line are used, to derive the magnetic surface map by taking the true temperature distribution as prior knowledge. In doing so we demonstrate the performance of the magnetic inversion only and make sure that a possibly wrong reconstruction is not due to a wrong underlying temperature distribution. Results of this first test are shown in Fig. 4.5, which are to be compared with the true images in Fig. 4.4. It can be seen that the locations of spots as well as their size is remarkably well recovered. Also the field strength matches nicely the true image, only the low latitude spot exhibits a slightly smaller field than the true configuration. The error of field strength is in average 37 G per segment, while errors of meridional and azimuthal angle are 2.7° and 2.2°, respectively. The quality of the magnetic field reconstruction can also be inferred from the fits, shown as red dashed lines in the lower panel of Fig. 4.5, to the true Stokes profiles, plotted as black straight lines.

4.5.3 Test 2: using Stokes IV and true temperature

In stellar spectropolarimetry it is generally the case that one has only Stokes I and V available to reconstruct a surface magnetic field. Therefore, the second test addresses the ability to reconstruct the three component magnetic field by using only

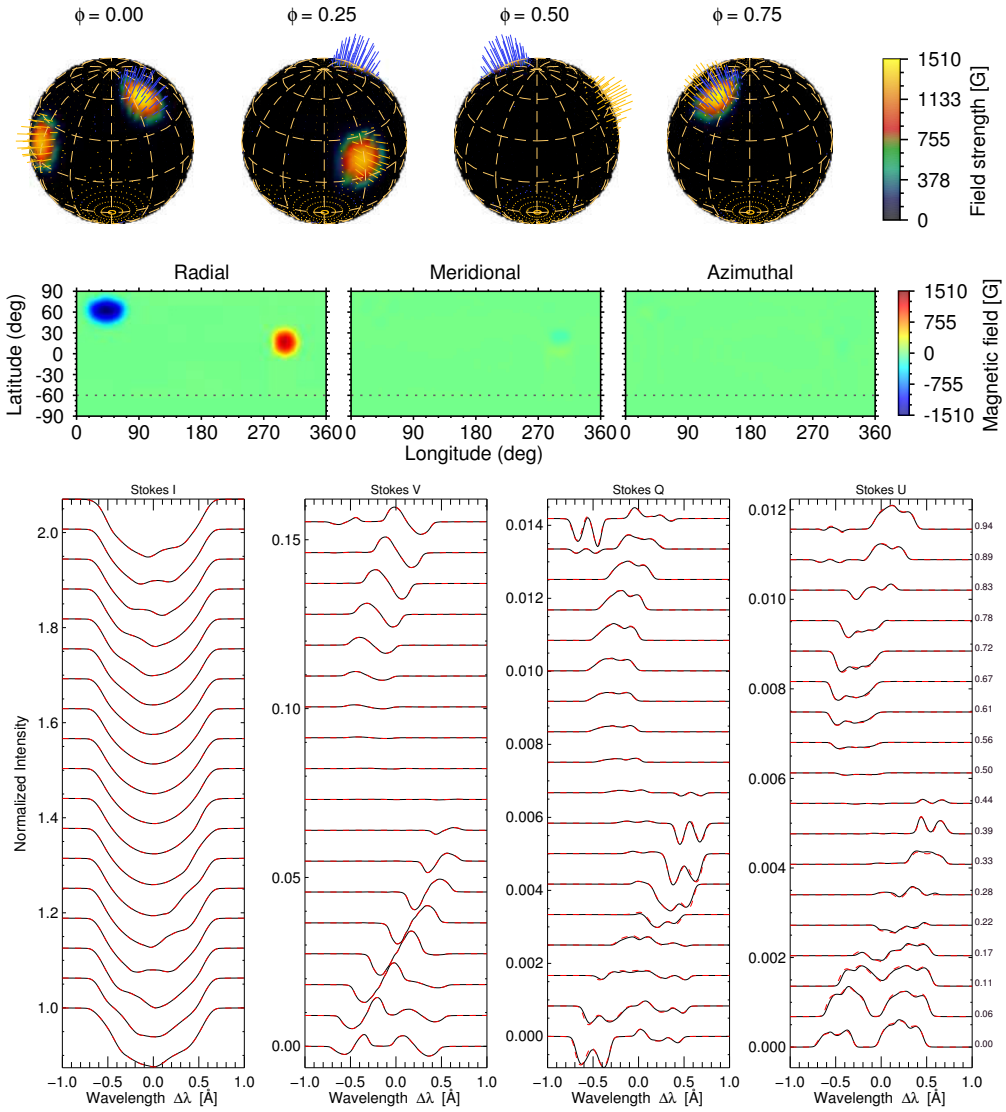

Figure 4.5: Reconstructed magnetic field for the 2-spot configuration with the true temperature distributions underlying (Test 1). The inversion is based on all four Stokes components, but temperature is kept fixed. In the top row orthogonal projections of field strength for four different rotation phases is shown. Blue field lines indicate a positive magnetic field, red field lines a negative. The three components of the vector magnetic field are shown as pseudo mercator plots in the middle row. Lower plots show the observed (black) and fitted Stokes profiles (red).

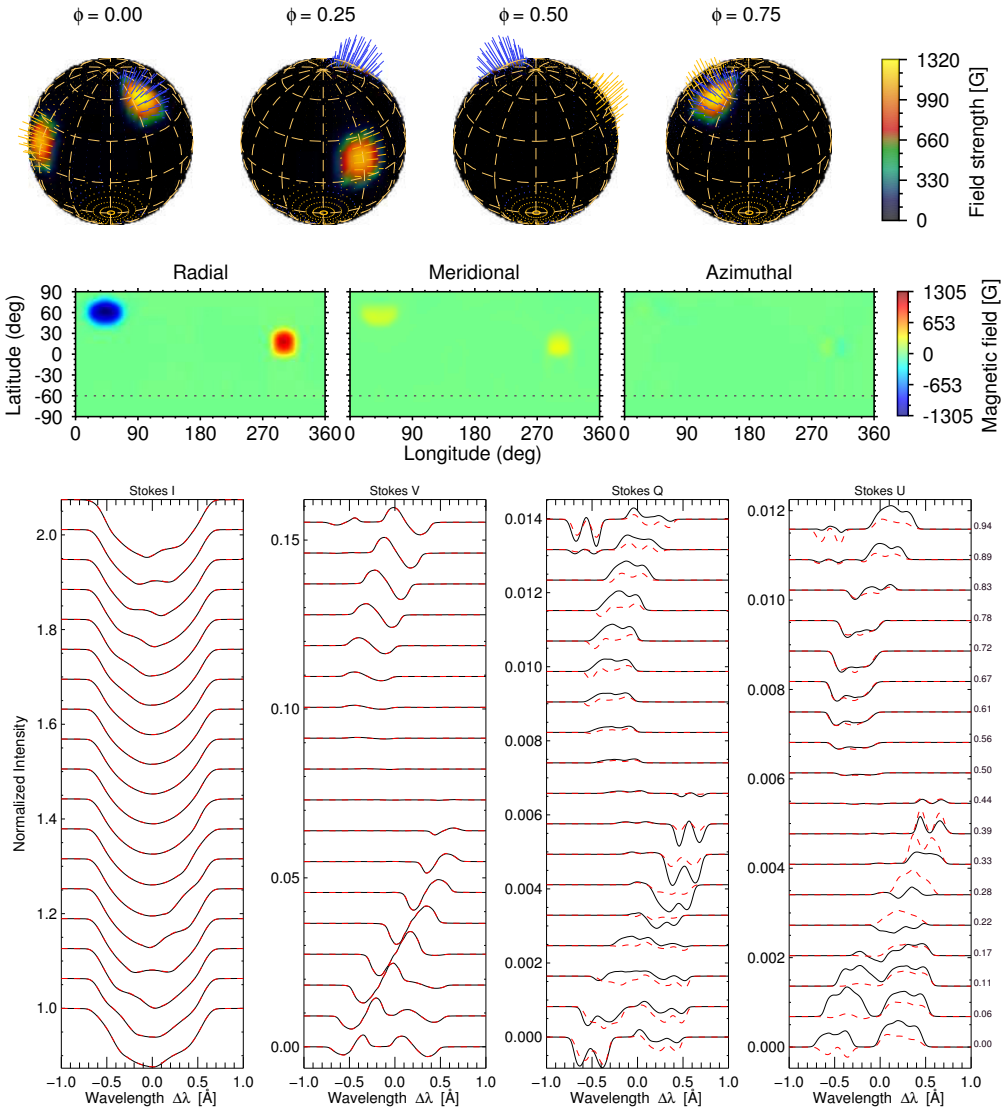

Figure 4.6: Reconstructed magnetic field for the 2-spot configuration with the true temperature distribution underlying (Test 2). The inversion is based on Stokes I and V, but the temperature is kept fixed. In the top row orthographic projections of field strength for four different rotation phases are shown. Blue field lines indicate a positive magnetic field, red field lines a negative. The tree components of the vector magnetic field are shown as pseudo mercator plots in the middle row. Lower plots show observed (black) and fitted Stokes profiles (red). Note that Stokes Q and U did not enter the error function. They are shown only to demonstrate the discrepancy.

Stokes I and V. It is the same condition as before only that we use now Stokes I and V. Also here the true temperature distribution is taken as prior knowledge so that we can directly compare it to the full Stokes inversion.

The Reconstructed magnetic field components are plotted in Fig 4.6 together with the fitted Stokes profiles. Note that also Stokes Q and U are shown, even though they did not enter the error function. Positions and sizes of the spots are again well reconstructed. Also the magnetic field is fairly good reproduced. The peak value of the radial component is about 200 G below its reference value. This is due to the crosstalk between radial meridional and azimuthal component. Average errors are 58 G in field strength 2.7° for meridional angles and 3.7° for azimuthal angles. Mercator plots in Fig. 4.6 reveal that there are small meridional and azimuthal components, which are however limited to spot locations. Nevertheless it nicely shows, that there is a crosstalk between the tree field components, indeed small but noticeable. This test calculation emphasizes the importance of the linear components for a precise reconstruction of field strength and orientation.

4.5.4 Test 3: using Stokes V and effective temperature

Since temperature can have significant impact on the formation of Zeeman signatures, we want to assess the influence of surface temperature on a magnetic inversion. Therefore we neglect in this test case the true underlying temperature distribution. It is the same setup as before, but the temperature is homogeneously set to the effective temperature $T_{\rm eff}$ and is fixed. Same Stokes V profiles as in previous test cases are then inverted to derive the magnetic field. Again, spot locations are well recovered, whereas sizes are slightly to large. This is partly due to the missing Stokes I profile in the inversion, which otherwise would have additional constraining effects on the spot size. Regarding the field strengths within the spots, they are largely underestimated. The mean deviation in field strength is 154 G, in the meridional angle 2.7°, and in the azimuthal angle 3.7°.

To some extents this is due to the larger spot size, as larger magnetic areas can be compensated by smaller field strengths. But when comparing it with Test 2 it becomes obvious that the higher underlying temperature within the spots, results in a crucial underestimation of the field strength. The reason for that is the photon flux, which is, at equal field strengths, larger for hot than for cool temperatures.

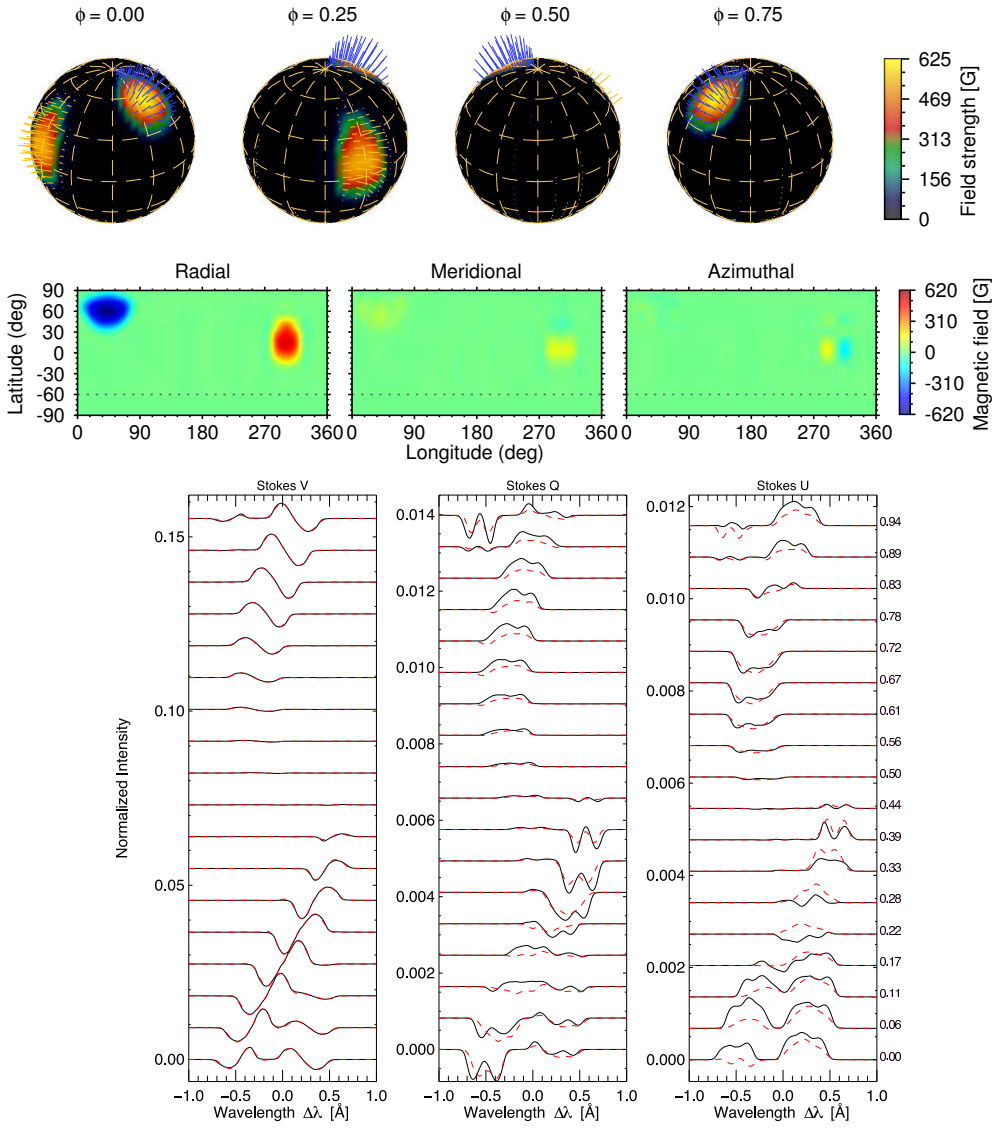

Figure 4.7: Reconstructed magnetic fields corresponding to Test 3. Only Stokes V of spectral line Fe I 6173 was inverted while surface temperatures were set to the effective temperature value of 5500 K. In the top row orthographic projections of field strength at four different rotation phases are shown. Blue lines indicate fields pointing inwards, red lines represent fields pointing outwards. The tree components of the vector magnetic field are shown as pseudo mercator plots in the middle row. Lower plots show observed (black, continuous) and fitted Stokes profiles (red, dashed). Note that Stokes Q and U did not enter the error function. They are shown only to demonstrate the discrepancy.

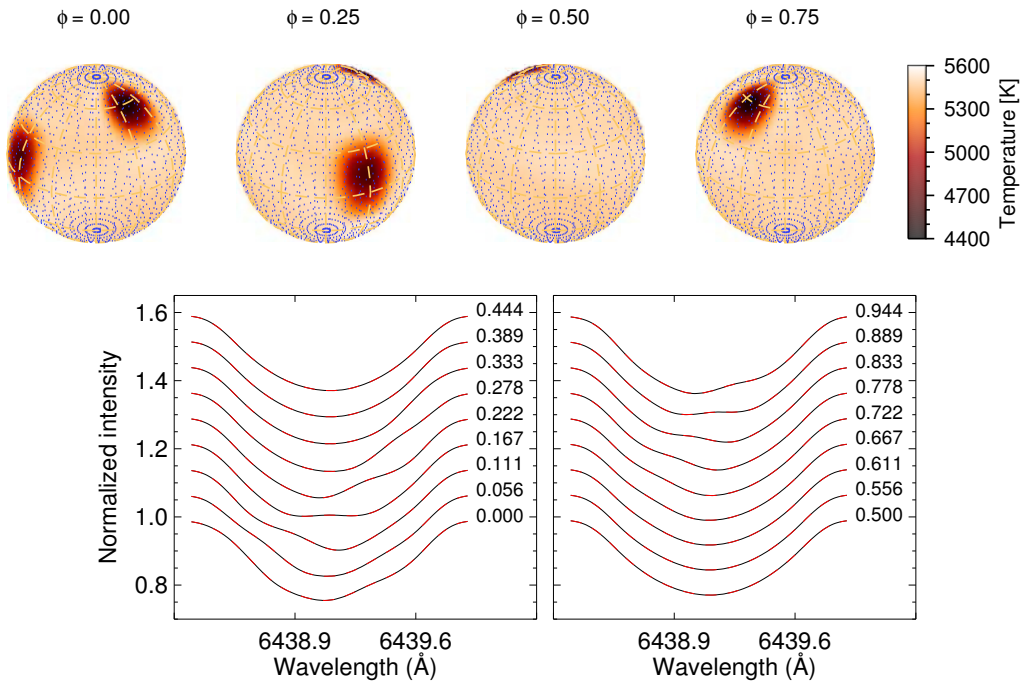

Figure 4.8: Test 4: Inversion of Stokes I profiles of spectral line Ca I 6439. Orthographic plots show the temperature distribution for four sequential rotation phases. In the plots below, true (black) and fitted (red) Stokes profiles can be seen.

4.5.5 Test 4: Temperature Inversion

As mentioned before, our strategy for the inversion of real data is to perform a DI to derive a temperature distribution on the basis of a temperature sensitive line. Using this temperature information as prior knowledge in a ZDI, we reconstruct the magnetic field using a magnetic sensitive line. We therefore invert Stokes I profiles of the Ca I 6439 line, for the two spot setup, to derive a Doppler map.

Resulting Doppler maps are shown in Fig. 4.8 together with the true and fitted spectra. Locations and temperatures of both spots are well recovered as it is also expressed by the mean error of 34 K. Only the low latitude spot extends slightly to much in latitudinal direction. However, this is a general trend in Doppler images that spots tend to be elongated in latitude (e.g. Rice et al. 1989). It is due to the limited rotational phase coverage. So there is a lack of information in the observational data, to further constrain a spot. While the longitudinal extension can be already inferred relatively good from a single rotation phase, it needs several rotation phases to reasonably constrain it in latitude. This accounts particularly

for low latitude features, which are not in as many rotational profiles present, as high latitude features.

4.6 Discussion

The previously presented test scenarios were supposed to demonstrate the capabilities of the inversion code and incorporated methods, introduced in Sec. 3.4.2 and 4.3.1. At the same time they were aimed to asses limitations of conjugate gradient based inversions in general. Of course these test cases are far from reality, but nevertheless they are adequate for the tests we aimed to perform.

The first conclusion we can draw from the test inversions is that *iMap* is able to successfully retrieve very precisely the magnetic field distribution in the ideal case, where all four Stokes components are present and the profiles are free of noise. Having only Stokes I and V available, which is in reality most often the case, reconstructions are still very good, but it becomes evident that there is a crosstalk between the three field components, mainly between radial and meridional component. In fact the longitude and latitude of active regions is well recovered, but to constrain the field strength and orientation more precisely, the two linear components would be needed.

The tests further show that high latitude spots are always better reproduced than low latitude features. This is an intrinsic limitation of DI / ZDI as discussed for example by Rice et al. (1989) or Brown et al. (1991). It is due to the fact that the signature corresponding to a high latitude spot is in more profiles of the different rotation phases present and therefor better constrained, than signatures of low latitude spots. Consequently low latitude spots tend to be more elongated in latitudinal direction. Our findings regarding the recovery of low latitudinal magnetic features as well as the crosstalk between the different field components matches with those of Donati & Brown (1997) and Kochukhov et al. (2002).

What we also see is that the underlying temperature distribution has significant influence on the magnetic inversion. Test 1 showed that the inversion algorithm is well able to reliably recover the field distribution when the true temperature distribution is incorporated. In contrast the field is largely underestimated when a homogeneous temperature distribution set to the effective temperature is used. This is due to the fact that we measure intensities, in other words photon flux. The photon flux is larger for higher temperatures than for lower temperatures at constant field strength. Consequently, in order to fit the "observed" Stokes V profiles in presence of a homogeneous effective temperature, a smaller field strength is required.

We conclude that the temperature information must be derived prior to a magnetic inversion or both should be simultaneously inverted.

When interpreting ZDI maps where only Stokes I and V are available for an inversion, which is unfortunately most often the case, it should be kept in mind that the magnetic field is subjected to crosstalks between the different field components. Most likely the field strength is underestimated on the cost of the area of the magnetic region, which tends to be overestimated.

5 Multi-line PCA reconstruction

The small degree of polarization in stellar spectropolarimetric observations led to the development of multi-line techniques proposed by Semel & Li (1996) and the Least-Square Deconvolution (LSD) introduced by Donati et al. (1997), for detecting and increasing polarization signals. The former method co-adds several hundred spectral lines to form a mean profile. Resultantly, incoherent features, such as noise, cancel out to a large extent. Basically, in a Zeeman-Doppler Imaging (ZDI) the same co-adding strategy, applied to observational data, could be used for the co-adding of synthetic line profiles. However, this would lead to tremendous polarized radiative transfer calculations for several hundred spectral lines and is therefore unrealistic. The method proposed by Donati et al. extracts, out of several hundred or even thousand lines a mean profile with artificial mean line parameters. Such a line is difficult to interpret and excludes the application of full polarized radiative transfer calculations. Instead it uses artificial Gaussian line profiles and furthermore utilizes the weak-field approximation.

As it was revealed through test inversions in the previous chapter, the consideration of temperature in an inversion of polarization profiles is essential for a reliable reconstruction of surface magnetic fields. However, this means that polarized radiative transfer calculations must be incorporated to account for the delicate interplay between temperature and magnetic field. Thus, a multi-line technique such as LSD is not reasonable as it provides only a mean profile. A denoising method is required which provides Stokes I as well as Stokes V of individual spectral lines. But it was also our ambition to have a technique allowing for a useful denoising of the linear Stokes components. This led to the development of a new multi-line denoising method, based on Principal Component Analysis (PCA).

Having a closer look on observed Stokes profiles of different spectral lines, it can be seen, that Zeeman signatures in Stokes V, Q and U, but also the imprints of temperature variations on Stokes I are to a certain degree similar for most of the spectral lines. Our aim was to make use of this resemblance of Stokes profiles and to find a new representation in terms of an orthonormal basis. This can be achieved by PCA and can be applied to any of the Stokes components. It allows to decompose each observed Stokes profile into a set of signal specific, orthonormal eigenprofiles.

In the following, we assume Stokes profiles of individual spectral lines to be given in velocity space according to $v = c\Delta\lambda/\lambda$, where c is the speed of light, λ the wavelength at line center and $\Delta\lambda$ the distance from the line center. The representation in velocity domain is important, as the Doppler shifts are equal for all spectral lines. In wavelength domain, however, the Doppler shift is larger for lines in the red part of the spectrum than for lines in the blue part, due to its λ dependence.

Let us define signal vectors x_n, representing $n = 1, \ldots, N$ observed Stokes profiles either of component I, V, Q, or U. The vectors consist of M velocity points, where $j = 1, \ldots, M$ is the index. In order to establish the covariance matrix C of the Stokes profiles corresponding to N individual spectral lines, we subtract from each signal vector the mean of all signals and get

$$\mathsf{C} = \sum_n (\boldsymbol{x}_n - \overline{\boldsymbol{x}})(\boldsymbol{x}_n - \overline{\boldsymbol{x}})^{\mathsf{T}} \quad , \tag{5.1}$$

where T is the transpose operator. C_x is of size $M \times M$. The eigenvectors $\boldsymbol{s}_i$ of the covariance matrix are the coordinate axes of the new representation of Stokes profiles. They can be derived according to

$$\mathsf{C}\boldsymbol{s}_i = \lambda_i \boldsymbol{s}_i \quad , \tag{5.2}$$

by Singular Value Decomposition (SVD; Press et al. 1992) and constitute an orthogonal basis. The most coherent features in the Stokes profiles are represented by the eigenvectors with the largest eigenvalues, while incoherent features such as noise are covered by those eigenvectors with the smallest eigenvalues. The entire set of observed Stokes profiles can be decomposed into its eigenvectors according to

$$\boldsymbol{x}_n = \sum_i^N \alpha_{n,i} \boldsymbol{s}_i \quad , \tag{5.3}$$

where $\alpha_{n,i} = \boldsymbol{x}_n \boldsymbol{s}_i$ is the projection (scalar product) of the n-th signal vector onto the i-th eigenvector.

So far we only expressed the observations in a new, data specific way. But the denoising is now as simple as taking only the first few, most significant eigenvectors in Eq. 5.3 for the reproduction of observations:

$$\boldsymbol{x}'_n = \sum_i^L \alpha_{n,i} \boldsymbol{s}_i \quad . \tag{5.4}$$

The number L of the most significant eigenvectors, also named principal components, is specified by $L < M$. Of course, the outcome $\boldsymbol{x}'$ is then no longer identical

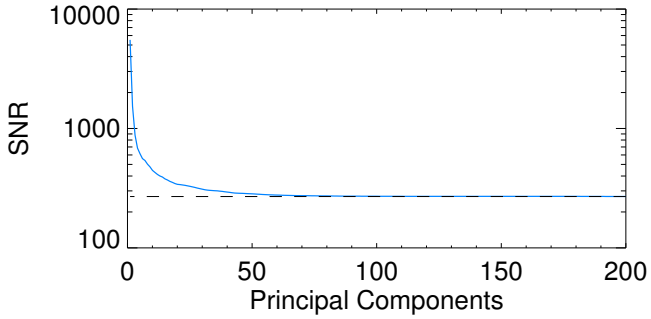

Figure 5.1: SNR of reconstructed Stokes V profiles as a function of the number of principal components.

with the original observations, but this is not the aim, because we want to get rid of the noise. This is achieved by selecting only the significant eigenvectors - the principal components, which means those with the largest eigenvalues. It is a characteristic of the covariance matrix that eigenvectors associated with the largest eigenvalues represent directions of highest correlation. Thus, random noise, which is uncorrelated is represented by the eigenvectors with the lowest eigenvalues. In our case, correlation means that the line formation in a stellar atmosphere is similar for each spectral line.

By performing a principal component analysis on the basis of several hundred spectral lines, we are able to reconstruct Stokes profiles of individual spectral lines, in which common and systematic features are retained, but uncorrelated signatures such as noise are removed. Note that this method uses only observational data itself to reduce the noise in individual spectral lines.

The basic free parameter of this method is the number of principal components (L). No strict rule can be given for the choice of this value, but the following gives an appropriate strategy (Martínez González et al. 2008).
To each signal vector a noise vector is constructed, containing purely noise with the same variance as it is present in the observation. All these noise vectors can be written as a matrix, whose eigenvalues can be estimated. While the eigenvalues of the noise matrix are almost equal, those of the data matrix show a declining distribution and run into a plateau. The plateau has about the same value as the eigenvalues of the noise matrix. The basic idea is to select those eigenvectors, whose eigenvalues are higher than those of the noise matrix.

When using only the first eigenprofile, which very closely matches the mean profile, the SNR approximately scales, like LSD, with the square root of the number of used spectral lines. The more principal components are used, the smaller the gain

in SNR becomes. This is shown in Fig. 5.1, where the SNR of reconstructed Stokes V profiles is plotted as a function of the number of principal components. The graph corresponds to the PCA-denoising of the II Peg data from 2004, presented in a later chapter (6.1). For an example of PCA denoised Stokes V profiles see Fig. 6.1.

6 Application to II Pegasi

II Pegasi (HD 224085) is known as one of the most active RS CVn type stars. This class of stars shows a strong photometric variability, which is interpreted as cool star spot variation along the rotational cycle. Due to its particularly strong activity II Peg had received much attention since the 1970s. Its photometric variability was first detected by Chugainov (1976) and identified as rotational modulation by large cool surface spots. Furthermore, II Peg shows also strong emission at Ca II H, K, and Hα lines (Rucinski 1977). On the sun these are generally indicators for chromospheric activity and correlate with regions of strong magnetic fields. Strong correlations were found between Hα emission and the occurrence of spots. The emission strength was largest when the spot was best visible (Vogt 1981b). Such a spatial correlation was also found for UV emission line flux by Rodonò et al. (1987), who interpreted this as large photospheric spots with overlaying magnetic loops, forming plages in the outer atmosphere.

Vogt (1981a) was the first who attempted to assess the magnetic fields on II Peg. From photometric and spectroscopic observations in 1977-1978, including Zeeman analysis, he derived not just starspot temperatures and areas, but he also estimated the longitudinal magnetic field at different rotation phases (Vogt 1980). It was done by measuring the circular polarization in the wings of the Hα emission line and then deriving the longitudinal field according to the weak field approximation (see e.g. Landi Degl'Innocenti 1992). This method is only sensitive to the line-of-sight component of the magnetic field, averaged over the whole stellar disk. At one rotation phase Vogt found a substantial field strength of $-515\,\mathrm{G}$, while fields at the other rotation phases were rather weak. However, following an error estimation he also states that even though it would be tempting to claim the $-515\,\mathrm{G}$ result as an actual detection, it would be not regarded as highly significant (Vogt 1980).

Another work by Donati et al. (1992) aimed at ascertaining the magnetic field from Stokes V measurements, by means of Zeeman-Doppler Imaging (ZDI). However, in this case ZDI did not yet refer to a surface mapping by the inversion of Stokes profiles observed at different rotation phases during a full rotation, but rather to the original concept proposed by Semel (1989). Accordingly, the longitudinal fields of iso-radial velocity stripes are derived from Stokes V profiles of individual rotation

Parameter	Value
T_{eff}	4600 K
$\log g$	3.2
$v \sin i$	22.6 km/s
[M/H]	-0.4
Microturbulence ξ_t	2.0 km/s
Macroturbulence ζ_t	3.5 km/s

Table 6.1: Stellar Parameters of II Peg.

phases. Donati et al. (1992) only give an upper detected effective field value of 70 G.

First surface resolved temperature distributions in terms of 2-dimensional maps were derived by Doppler Imaging (DI) and presented by Hatzes (1993). A more recent study by Berdyugina et al. (1998a, 1999a) revealed a series of Doppler maps for the years 1992 to 1998. They claimed to have found a flip-flop on II Peg (Berdyugina et al. 1999a). This was shortly after confirmed by Rodonò et al. (2000).

So far, no surface resolved magnetic field maps were obtained for II Peg. In order to invert Stokes I and V profiles with iMap several stellar parameters must be known a priori. Since it is beyond the scope of this thesis to derive new independent parameters from our data, we rely on those of other authors. Therefore we make use of the stellar parameters obtained by (Berdyugina et al. 1998b).

The primary of II Peg is a subgiant (luminosity IV) of spectral type K2, featuring a rotation period of 6.72 days and, according to Berdyugina et al. (1998b), an effective temperature of $T_{\text{eff}} = 4600\,\text{K}$, a surface gravity of $\log g = 3.2$, a metalicity of $[\text{M/H}] = -0.4$ and a micro turbulence of $\xi_t = 2.0\,\text{km/s}$. Furthermore the mass was estimated to be $M \approx 0.8\,M_\odot$, the radius $R \approx 3.4\,R_\odot$ and the inclination $i \approx 60°$.

To use the fast Stokes profile synthesis method, we trained a set of neural networks on local Stokes profiles of the spectral line Fe I 5497, whose atomic data is listed in Tab. 6.2. The underlying atmosphere is specified by the parameters in Tab. 6.1 and was interpolated within the Kurucz grid (Kurucz 1993). The fast synthesis method was presented in Chap. 3.

Parameter	Value
λ_0	5497.516 Å
$\log gf$	-2.849
E_l	1.011 eV
E_u	3.266 eV
$\log \gamma_{Rad}$	7.152
$\log \gamma_{Stark}$	-6.302
$\log \gamma_{vdW}$	-7.751
lower term	$^5F_1$
upper term	$^5D_2$
lower Landé	-0.01
upper Landé	1.50
mean Landé	2.26

Table 6.2: Line data of Fe I 5497, taken from VALD.

6.1 Observations

Observations were obtained in the summer of the years 2004 and 2007 with the SOFIN spectrograph (Ilyin 2000a; Tuominen et al. 1999) at the Nordic Optical Telescope (NOT), a 2.56 m telescope on La Palma, Canarian Islands.

SOFIN is a high resolution échelle spectrograph equipped with a cross-dispersion prism. A polarimetry unit can be installed in front of the entrance slit to allow for the observation of two polarization (left and right circular) states at a time and thus gives, according to Eq. (2.4), Stokes V. Three different cameras, corresponding to spectral resolutions $R = \lambda/\Delta\lambda =$ 30 000, 80000, and 170000 are provided. For the observations of II Peg, the second camera with the medium resolution was selected for Stokes I as well as for Stokes V. All II Peg spectra were reduced with the reduction package *4A* (Ilyin 2000b). Observations and data reduction were carried out by Ilya Ilyin.

The 2004 and 2007 observations exhibit 8 and 10 rotation phases respectively, and feature a wavelength range from about 4500 Å to 6135 Å with some gaps at the boarders of neighboring échelle orders. Unfortunately, the preferred Fe I 6173 line, which was used in the synthesis study (Sec. 3.4.2), was not available by the observational data. Therefore, we chose the strong spectral line Fe I 5497, which has a relatively large mean Landé factor of 2.26. It was used for both, DI and ZDI. The average SNR of the data are 250. Individual SNRs for each

observation are shown in Tab. 6.3 together with observation dates and rotation phases.

II Peg observations

Date	HJD +2400000	Phase	Peak SNR
30/07/2004	53216.6143	0.379	188
31/07/2004	53217.6364	0.531	257
01/08/2004	53218.6518	0.682	260
02/08/2004	53219.6233	0.826	260
03/08/2004	53220.6305	0.976	212
05/08/2004	53222.6133	0.271	240
10/08/2004	53227.7140	0.030	284
11/08/2004	53228.6079	0.162	292
19/07/2007	54300.6973	0.597	247
20/07/2007	54301.6858	0.744	283
21/07/2007	54302.6688	0.890	293
22/07/2007	54303.6120	0.030	287
23/07/2007	54304.6795	0.189	261
24/07/2007	54305.6666	0.336	321
25/07/2007	54306.6430	0.481	336
26/07/2007	54307.7142	0.640	264
27/07/2007	54308.6469	0.779	298
28/07/2007	54309.6769	0.932	239

Table 6.3: Spectropolarimetric observations of II Peg for the years 2004 and 2007. First column: UT date, second: heliocentric Julian date, third: rotation phases, last column: signal-to-noise ratio.

6.2 Denoising

The PCA denoising, described in Sec. 5 was applied in a consistent manner to Stokes I and V observations of II Peg. First, a list of significant spectral lines that are present in II Peg observations was extracted from VALD. For all these

lines local Stokes I and V profiles were synthesized with a Kurucz atmosphere as specified by the parameters in Tab. 6.1. In the computation of Stokes V, a field strength of 1000 G was assumed. To select the lines for the PCA decomposition, in case of Stokes I a central line depth greater then 0.6 was required. This resulted in 1000 spectral lines. In case of Stokes V the selection criterium was the profile amplitude, which had to be larger then 0.01. The resulting number of lines was 883.

When reproducing Stokes profiles of individual spectral lines with reduced noise level, the fundamental free parameter in this method comes into play. It consists in the choice of the number of principal components. A selection criterion for this principal components was given in Chap. 5. Accordingly, we used here for the reconstruction of the Stokes I profiles of spectral line Fe I 5497 the first 16 principal components. Stokes V was reconstructed with 3 principal components.

6.3 Temperature distribution

As mentioned before, the strategy of our inversion process was to sequentially perform DI and ZDI. At first a temperature distribution was derived, which was then used in a following magnetic inversion. In doing so, we assured that the complex interplay between temperature and magnetic field is accounted for. Test 3 in Sec. 4.5 revealed that the temperature has significant impact on the formation of Zeeman signatures. In contrast, the localized magnetic fields of strength as expected for late-type stars, have only marginal influence on the intensity profiles and their consideration in the formation of Stokes profiles is irrelevant. This legitimates the consecutive determination of temperature first and then magnetic field instead of a simultaneous inversion.

Thus, we first applied the inversion code in DI mode to the Stokes I profiles. In a wavelength range of 2 Å about the line center of the spectral line Fe I 5497, all blends falling in this region were accounted for. Extracted from VALD, these were 35 in number. Required stellar parameters are listed in Tab. 6.1. An equal-degree surface grid with a resolution of $6^\circ \times 6^\circ$ was initialized with a homogeneous temperature set to the effective temperature of 4600 K. In comparison to the test inversion the segment size was chosen to be slightly larger, since the wavelength sampling of the observational data is coarser. The benefit is a smaller number of free parameters. The inversion was performed until convergence was reached, which took in average 50 iteration cycles.

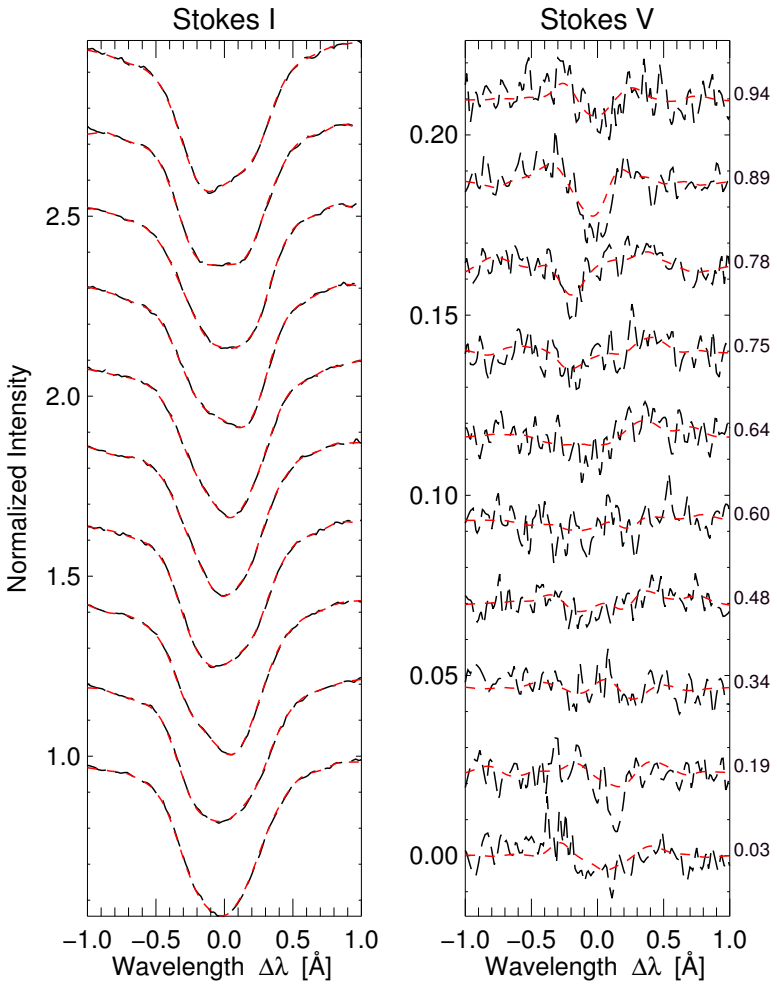

Figure 6.1: PCA denoised Stoke I and V profiles (Fe I 5497) of the II Peg observations for the year 2007. Observations are plotted in black, denoised profiles in red.

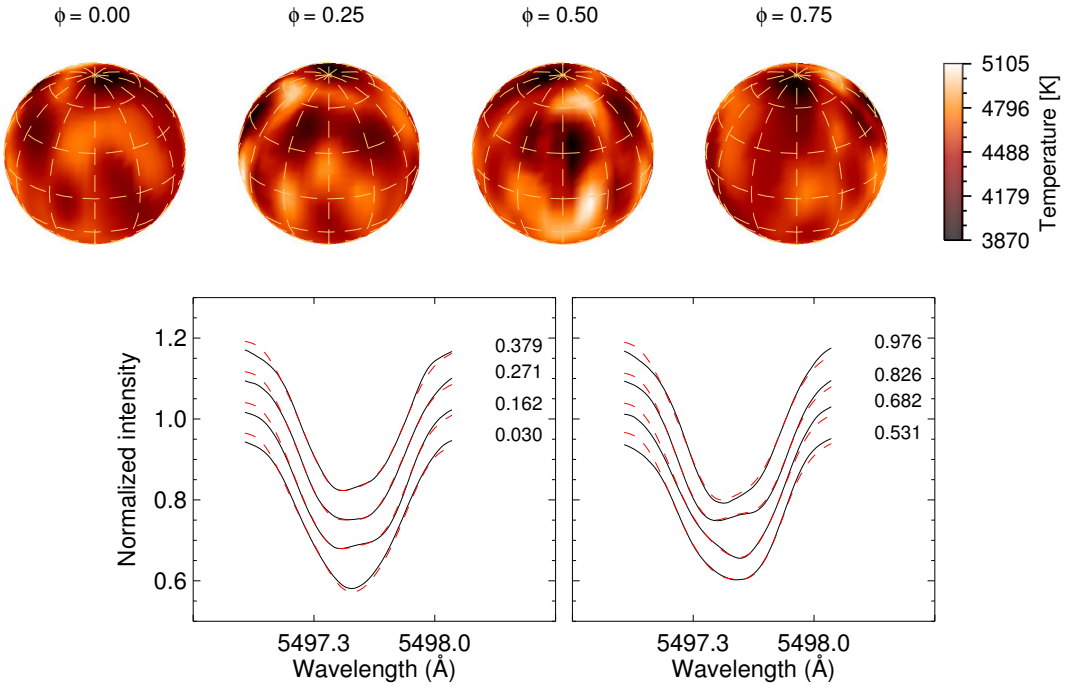

Figure 6.2: Doppler images of II Peg for the 2004 data. Stokes profiles below the orthographic maps show observed data as black continuous lines and the fitted data as red dashed lines. On the right of each profile the corresponding rotation phase is plotted. For representation purposes, profiles are plotted with a constant offset from each other.

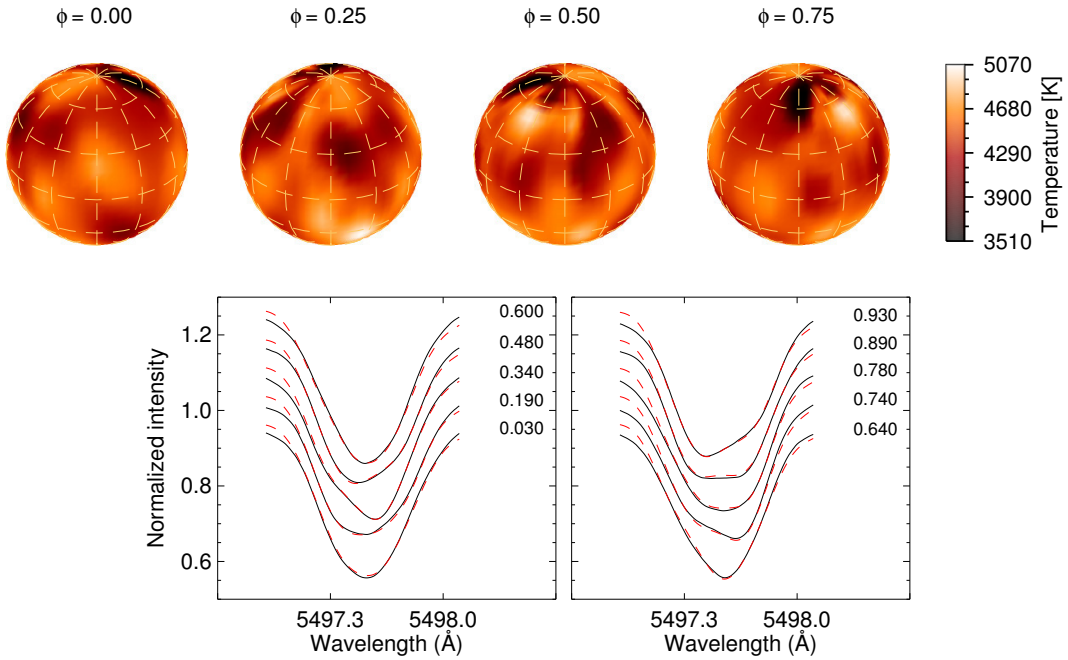

Figure 6.3: Doppler images of II Peg for the 2007 data. Stokes profiles below the orthographic maps show observed data as black continuous lines and the fitted data as red dashed lines. On the right of each profile the corresponding rotation phase is plotted. For representation purposes, profiles are plotted with a constant offset from each other.

Resulting Doppler maps are shown in Figures 6.2 and 6.3 together with the denoised observations and corresponding fitted profiles. The fits reproduce the observed profiles very well. The temperature distribution is plotted in orthographic projection at four equidistant rotation phases.

In 2004, there are essentially 2 cool spots at high latitudes, one between 30° and 60° and another between 60° and 90°. In 2007, there was one dominating spot at a latitude of about 60°. Spot temperatures are around 3870 K in 2004 and 3510 K in 2007. The results agree with those of Hatzes (1993) and Berdyugina et al. (1998a) who also obtained Doppler images but also with others like Vogt (1981a) who derived spot positions from photometric observations. Cool spots were always found at intermediate to high latitudes.

6.4 Magnetic field distribution

We obtained for the first time magnetic field maps of II Peg by means of ZDI. Previously obtained Doppler images assured that the influence of the temperature on the formation of Zeeman signatures was accounted for.

Required stellar input parameters to the magnetic inversion are the same as for the temperature inversion. The configuration of the initial surface distribution consisted of setting the segment temperatures to the corresponding values of the Doppler images and the three component magnetic fields to zero. Azimuthal, meridional, and radial magnetic field components of all visible surface elements were considered as free parameters. The denoised Stokes V profiles of the spectral line Fe I 5497, which were supposed to be inverted, covered 8 rotation phases for 2004 and 10 rotation phases for 2007.

Resulting maps for 2004 are shown in Fig. 6.4 and for 2007 in Fig. 6.5. Both years show high latitude magnetic spots with predominantly radially oriented fields. In 2004, there is one single large spot at a latitude of 60°, which is centered at a longitude of about −140° and extends towards higher longitudes. Its central field strength is around 1000 G. The computation of the longitudinal magnetic field is at maximum 71 G. The total surface magnetic flux density yields a value of −42.4 G. Interestingly, in 2007, there are two pronounced spots of opposite polarity again at high latitude of about 60°. In longitudinal direction they are roughly 100° apart. While one spot features field strengths of up to 700 G the other of opposite polarity has field strengths around 600 G. Here the total magnetic flux density is 17.8 G. An estimation of the longitudinal magnetic field for the rotation phase $\phi = 0.0$, where both spots are facing the observer, yields a value of 5.7 G. The longitudinal field

for the rotation phase $\phi = 0.75$, where one spot is well exposed to the observer and the other is nearly invisible, yields 76.7 G.

6.5 Discussion

II Peg has always been of particular interest due to its strong surface activity and its relatively large luminosity. The large cool spots detected in the beginning by photometric observations and later spatially resolved by DI were always addressed to magnetic fields (e.g. Vogt 1980; Berdyugina et al. 1999a). However, surface magnetic fields were never directly measured in the sense that individual field components were assessed and spatially resolved. Only the longitudinal field over the stellar disk was estimated (Vogt 1980; Donati et al. 1992). This study gives for the first time detailed magnetic field surface topologies of II Peg for the years 2004 and 2007.

Our derived temperature maps, showing high latitude spots with distinct longitudinal migration, agree well with previous studies (Hatzes 1993; Berdyugina et al. 1998a). However, the most interesting and important results come from the magnetic inversions, as they provide for the first time information on magnetic field locations, polarities and field strengths. The derived magnetic field maps allow us to give evidence to some open questions: Are cool spots associated with magnetic fields? What is the approximate field strength of II Peg? Are there indications for active longitudes and the flip-flop phenomenon?

The derived surface maps show only a small overlap of the pronounced cool temperature spots and the magnetic regions. Such small correlations were also observed by former ZDI approaches (Donati et al. 1999). By solar analogy, one would expect an immediate coincidence as sunspots are imprints of magnetic fields. If a solar analogy is assumed, the question comes up why magnetic spots are not seen at the same position as temperature spots. Several reasons can be accounted for, which might explain this discrepancy. One problem is the suppressed photon flux from cool regions, so that the contribution to the circular polarization signatures is smaller from cool than from hot magnetic regions. Therefore, it is more difficult to detect a magnetic field in a cool spot when it is surrounded by warmer magnetic regions. II Peg is in particular known to possess also strong chromospheric activity (e.g. Rucinski 1977), which was linked to plage regions around cool spots (Rodonò et al. 1987) and to flares (Berdyugina et al. 1999b). Plages and flares are also strongly correlated with magnetic activity. Thus, magnetic activity on II Peg is rather complex and mutual cancellations of close bipolar configurations are very likely.

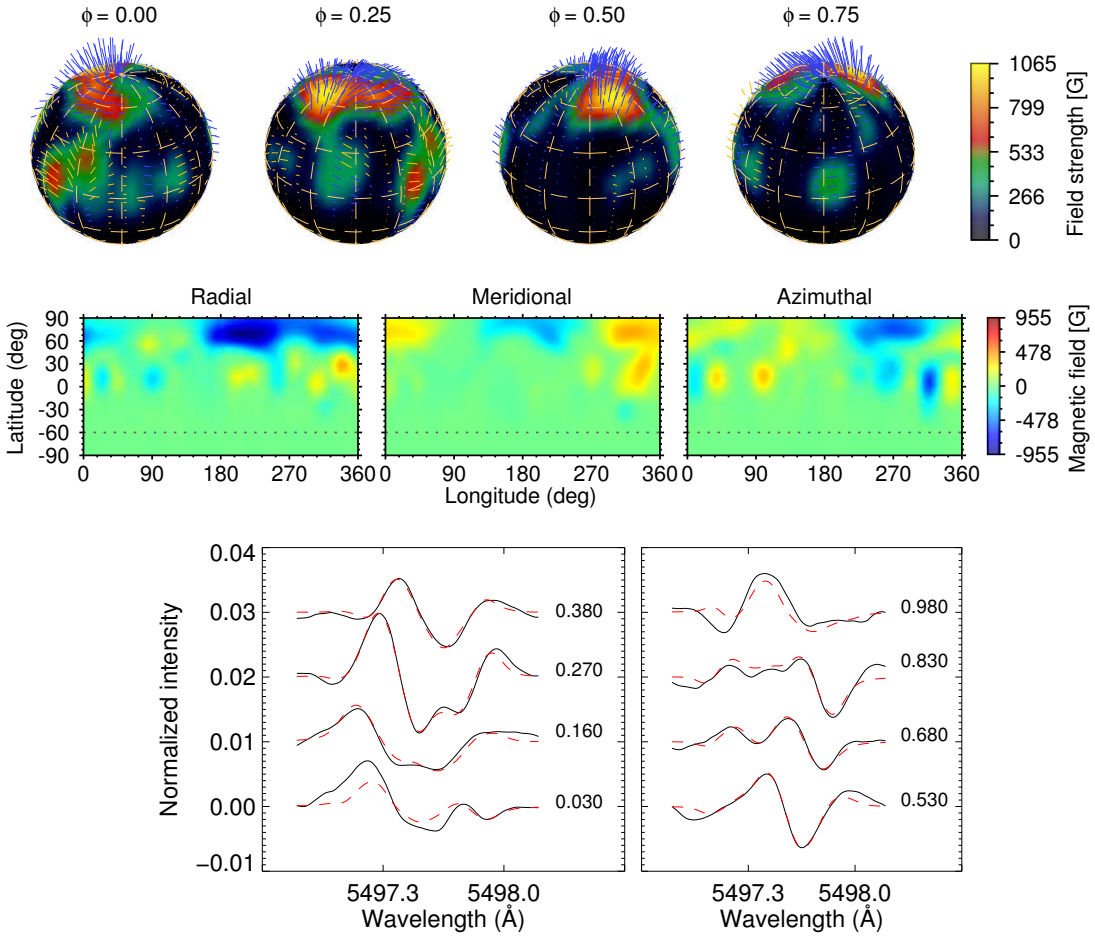

Figure 6.4: Magnetic field maps of II Peg for the 2004 data. First row: field strength in orthographic projection at four different rotation phases. The field orientation is indicated by field lines; blue lines represent a field pointing inwards and yellow lines a field pointing outwards. Second row: radial, meridional, and azimuthal field components are presented in pseudo-mercator projection. Last row: PCA denoised Stokes V profiles of the spectral line Fe I 5497 as black continuous lines with corresponding rotation phases plotted to the right. Fitted profiles are plotted as red dashed lines. For representation purposes, profiles are plotted with a constant offset from each other.

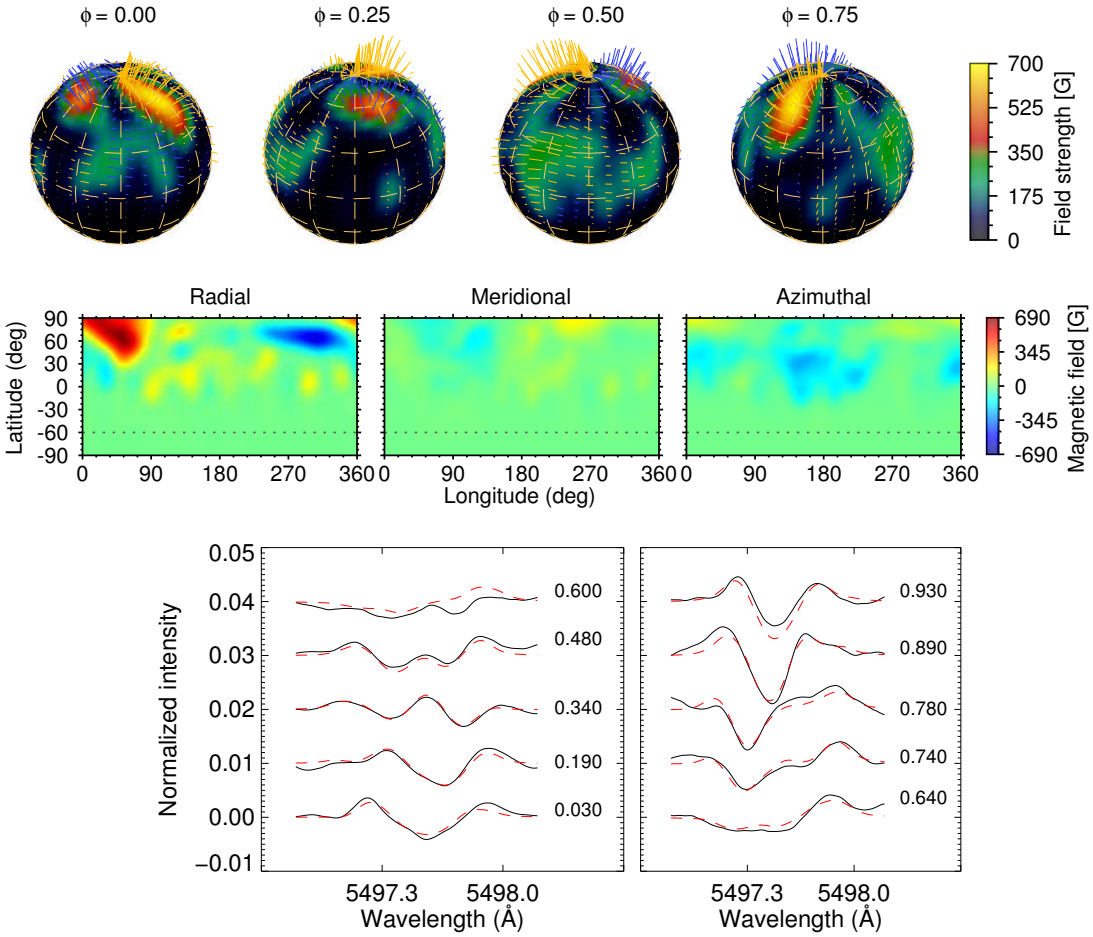

Figure 6.5: Magnetic field maps of II Peg for the 2007 data. First row: field strength in orthographic projection at four different rotation phases. The field orientation is indicated by field lines; blue lines represent a field pointing inwards and yellow lines a field pointing outwards. Second row: radial, meridional, and azimuthal field components are presented in pseudo-mercator projection. Last row: PCA denoised Stokes V profiles of the spectral line Fe I 5497 as black continuous lines with corresponding rotation phases plotted to the right. Fitted profiles are plotted as red dashed lines. For representation purposes, profiles are plotted with a constant offset from each other.

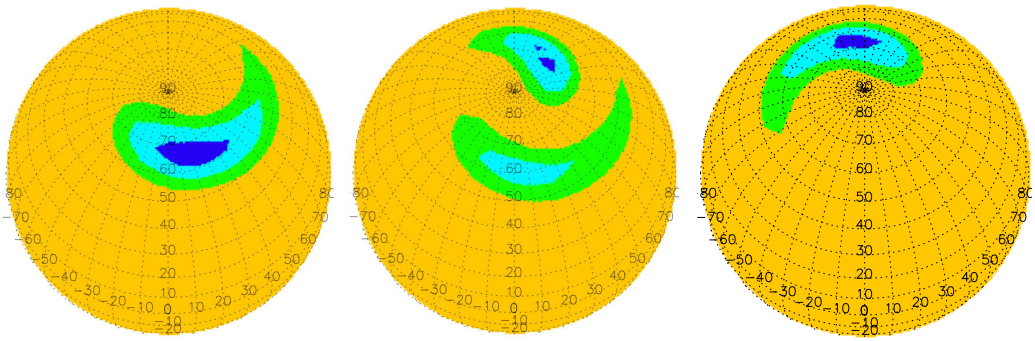

Figure 6.6: Model calculation of the magnetic pressure for a thick layer dynamo model. Three snapshots from a flip-flop cycle are shown. The blue, dark regions exhibit the strongest magnetic pressure (from Elstner & Korhonen 2005).

As mentioned before, former magnetic field studies only derived estimates of the longitudinal field. While Vogt (1980) found at maximum an effective longitudinal magnetic field in the order of 500 G, Donati et al. (1992) estimated maximal values of 70 G. Our derived magnetic field maps possess few distinct magnetic spots, which harbour a predominantly radially oriented field. An estimation of the longitudinal field from the magnetic surface maps yields values of about 70 G and thus favors the findings of Donati et al. (1992).

One phenomenon on II Peg that was so far only derived from long-term photometric observations and Doppler images is the flip-flop mechanism (Berdyugina et al. 1999a). This refers to the fact that active regions appear at two opposite longitudes, so called active longitudes where the strength of the activity changes periodically between these longitudes. However, an essential ingredient according to theoretical models, is the bipolar nature of the two active longitudes, which could not be revealed so far.

The global structure of the magnetic field is determined by the superposition of different dynamo modes, characterized by different symmetries (Brandenburg & Subramanian 2005). Elstner & Korhonen (2005) investigated in detail dynamo models, which were able to generate flip-flops. They modeled an $\alpha^2\Omega$-dynamo as a turbulent fluid in a spherical shell and imposed a solar-type rotation law. The inner boundary condition was described by a perfect conductor, the outer boundary condition by a vacuum condition. In order to explain the flip-flop phenomenon, an oscillating axisymmetric as well as an azimuthal migrating bisymmetric mode must be excited (Elstner & Korhonen 2005). The excitation of the different modes is essentially influenced by the strength of differential rotation, the amount of magnetic diffusivity and thickness of the convection zone. For a thick convection zone where the bottom of the convection zone is at a radius of $r_{in} = 0.4$, Elstner & Korhonen (2005) found models in which opposite spots do not appear exactly 180° apart, but

can occur at longitudes down to 90° apart. Such a thick layer model is shown in Fig. 6.6. It correlates with the magnetic field topology of II Peg shown in Figs. 6.4 and 6.5. In 2004, there is one dominating unipolar active longitude, while in 2007 there are two spots of opposite polarity, as required by dynamo models that are able to explain the flip-flop phenomenon. The two spots are in longitude about 100° apart. According to Durney & Robinson (1982) the bottom of the convection zone for a star of spectral type K2 like II Peg is approximately at $r_{in} = 0.5$ and, thus, closely resembles the thick convection zone model. Note that there are only two magnetic field maps of II Peg so far, nevertheless they seem to confirm nicely the flip-flop generating dynamo models.

7 Conclusion

To draw conclusions, results are summarized and discussed with respect to possible future studies related to the various diagnosis and analysis methods presented in this thesis as well as the temperature and magnetic field inversions of II Peg.

Zeeman Doppler Imaging (ZDI) is a useful and powerful method to retrieve surface magnetic field distributions of rapidly rotating stars from spectropolarimetric observations. Due to the complexity of the problem, many applications of ZDI rely on various approximate methods, which sometimes even completely avoid radiative transfer calculations.

In the ambition to incorporate full polarized radiative transfer calculations in a ZDI for the imaging of active late type stars, several questions rise: How can the large computational burden of such an inversion method be handled? What is an appropriate regularization method, accounting for the localized and small scale magnetic fields expected on late-type stars? How can the often heavily distorted data be denoised, so that a full polarized radiative transfer can still be applied? These issues were addressed by this thesis and possible solutions were given.

Test calculations proof the reliability of the various methods. In the first ZDI approach of the active late-type star II Peg, magnetic field maps were derived for this object. II Peg is known to posses strong surface activity, and its large cool spots as well as its chromospheric emission features were believed to be correlated with magnetic fields. However, up to now only longitudinal field estimates were available. This work allows for the first time to examine the magnetic field topology and opens up the possibility to study phenomena like the proposed flip-flop and to give a deeper insight to the ongoing dynamo process.

7.1 Fast Stokes profile synthesis

To cope with the high computational demands of ZDI, we have developed a fast Stokes profile synthesis method based on Principal Component Analysis (PCA)

and Multi-Layer-Perceptrons (MLPs), a common type of artificial neural networks. These are used to approximate the mapping between atmospheric parameters (temperature, three component magnetic field, line of sight angle) and corresponding Stokes profiles.

As the method is trained on Stokes profiles calculated by a conventional polarized radiative transfer (RT) code, we first evaluated its reliability and accuracy by comparing it with the freely available RT code COSSAM (Stift 2000). This comparison showed remarkably good agreement between both codes.

A detailed validation of the fast synthesis method showed the capability and accuracy of the method as well as the gain in time by almost three orders of magnitude compared to the conventional radiative transfer calculation. Thus, it is an ideal synthesis method for the use in a computationally demanding ZDI. In principle it is applicable and useful in any field where repeatedly extensive numbers of Stokes profile synthesis are required. Another application, which was not approached here, but is worth a further investigation, is the synthesis of co-added profiles by means of PCA-MLP synthesis. Artificial neural networks would be no longer trained on Stokes profiles of single spectral lines, but on co-added profiles of a large number of spectral lines. Applying the same co-adding scheme to observed profiles, this would significantly reduces the noise. Such readily trained neural networks would have just about the same computational request as a network, which is trained to synthesize only Stokes profiles of a single spectral line, as it was presented here.

We believe that the PCA-MLP synthesis is a very powerful tool and ideal for ZDI. It is also very suitable for the study and analysis of stellar magnetic fields in terms of forward modeling, since it allows for an almost instantaneous synthesis of a disk integrated profile. The forward module of our inversion code *iMap* allows, via a graphical user interface, the modeling of an arbitrary temperature and magnetic field configuration and the calculation of the corresponding Stokes profiles.

7.2 Stokes profile inversion

We presented new methods for Zeeman-Doppler Imaging (ZDI) as well as a newly developed inversion code, particularly designed with regard to the forthcoming spectropolarimeter PEPSI at LBT (Strassmeier et al. 2008). It will allow for the observation in all four Stokes components with a signal-to-noise ratio that is until now out of reach. One of its main science case, is the observation of active late type stars. Therefore, we put special emphasis on the ability to reconstruct

their localized and complex magnetic fields. The Inversion code had to incorporate full polarized radiative transfer calculations and make use of all fours Stokes components, in order to allow for a precise reconstruction of the vector magnetic field.

It makes use of a conjugate gradient method, to minimize the square difference between observed and synthesized Stokes profiles by adjusting the temperature and magnetic field surface distribution. In order to reconstruct the localized magnetic fields expected on these stars, a local entropy regularization function was added to the squared error function.

In various test calculations the ZDI code *iMap* proved to be able to successfully retrieve self consistent temperature and magnetic field surface distributions from either Stokes I and V or from all four Stokes components. When using only Stokes I and V there is a noticeable crosstalk mainly between radial and meridional magnetic field component. This has to be kept in mind when interpreting magnetic field maps, derived on the basis of only these two Stokes components. The comparison between two test inversions, where in one case the surface temperatures were set to the true distribution and in the other case set to the effective value, shows that the temperature has significant influence on the ability to recover the true surface magnetic field. We therefore attach importance to a self consistent temperature and magnetic field inversion.

7.3 Multi-Line denoising

Principal component analysis (PCA) was used in this work for two different aspects and proves to be a useful and powerful application. While it was previously used in the synthesis task as a simple dimensionality reduction (Carroll et al. 2008), it served here as a correlation analysis to denoise individual spectral lines.

The widely used least square deconvolution method (LSD; Donati et al. 1997) is not suitable for our purposes, as it only extracts a mean profile with artificial mean line parameters. Our newly developed PCA-denoising method utilizes a large number of spectral lines to decompose Stokes profiles into their respective eigenspectra. By reproducing Stokes profiles of individual spectral lines with only the first eigenvectors a significant increase of the signal-to-noise ratio is achieved.

The PCA based denoising method proofs to be a powerful method for ZDI as it is applicable to all four Stokes components. In contrast to LSD it does not use any approximation method, but only observational data itself to reduce noise

of individual spectral lines. Thus, it allows for an inversion based on individual spectral lines.

7.4 Surface magnetic field on II Peg

The newly developed ZDI code *iMap*, incorporating the fast Stokes profile synthesis, the local maximum entropy regularization as well as the PCA-denoising method, was applied to spectropolarimetric data of II Peg (Carroll et al. 2007). During the observing campaigns in summer 2004 and 2007, Stokes I and V profiles were obtained. An inversion of intensity and circular polarized profiles of the spectral line Fe I 5497 revealed temperature and then magnetic field distributions, by means of DI and ZDI, respectively. While the temperature maps nicely agree with previously obtained Doppler images, magnetic field maps were derived for the first time so far for II Peg. They show few large magnetic regions with predominantly radially oriented magnetic fields. In 2004, there is one large unipolar magnetic spot, whereas in 2007, there are two main spots of opposite polarity, about 100° apart.

The derived surface maps, nicely correlate with dynamo models (Elstner & Korhonen 2005), which are able to explain the flip-flop phenomenon. This was detected on II Peg by long-term photometric analysis and Doppler Imaging (Berdyugina et al. 1999a). Although we can not draw a conclusion regarding the flip-flop phenomenon from only two magnetic field maps, they confirm the flip-flop generating dynamo models.

7.5 Future studies

- We could show that the artificial neural network approach works very well for the synthesis of Stokes profiles of individual spectral lines. To expand on this idea we suggest to train artificial neural networks on already co-added Stokes profiles. This would have several advantages: Applying the same co-adding scheme to observed profiles would significantly reduce the noise in the resulting averaged profile. Implicitly, a large number of spectral lines would be fitted, while at the same time the inversion would still rely on polarized radiative transfer calculations. It would also require just about the same time as an inversion of a single spectral line with the PCA-MLP approach, even though the training process would be more computing intensive.

- The inversion code at its current state takes Stokes profiles of single spectral lines. It should be extended to allow the inversion of several spectral lines simultaneously. This will constrain the surface distributions as for example random noise is better averaged out by a larger sample.
- Besides the conjugate gradient minimization (CG) algorithm we had also implemented the Levenberg-Marquardt (LM) method. However, so far only the CG method was tested and used, due to its robustness and ability to handle a large number of free parameters. The LM algorithm could certainly improve the computation time. However, the LM method also requires extensive testing and possibly modification.
- Molecular lines should be incorporated in the inversion. According to solar analogy, one expects magnetic fields situated within cool spots. However, retrieved magnetic field maps of II Peg show only a small overlap, as has been also observed in former ZDI approaches (Donati et al. 1999). A reason is the photon flux emerging from cool spots, which is due to the lower temperature in respect to the quiet photosphere reduced. Molecular lines, which form only below a certain temperature in cool spots, could help to assess particularly the magnetic field within spots.
- Further observations of II Peg could reveal the long term evolution of the surface magnetic field and possibly confirm the flip-flop cycle, which was inferred from temperature maps by Berdyugina & Tuominen (1998).

Bibliography

Aller, M. F. & Everett, C. H. M. 1972, ApJ, 172, 447 20

Bellot Rubio, L. R. 1998, PhD thesis, Instituto de Astrofisica de Canarias

Berdyugina, S. V., Berdyugin, A. V., Ilyin, I., & Tuominen, I. 1998a, A&A, 340, 437 68, 75, 76

Berdyugina, S. V., Berdyugin, A. V., Ilyin, I., & Tuominen, I. 1999a, A&A, 350, 626 68, 76, 79, 84

Berdyugina, S. V., Braun, P. A., Fluri, D. M., & Solanki, S. K. 2005, A&A, 444, 947 6, 7

Berdyugina, S. V., Ilyin, I., & Tuominen, I. 1999b, A&A, 349, 863 76

Berdyugina, S. V., Jankov, S., Ilyin, I., Tuominen, I., & Fekel, F. C. 1998b, A&A, 334, 863 68

Berdyugina, S. V. & Tuominen, I. 1998, A&A, 336, L25 6, 85

Bishop, C. M. 1995, Neural Networks for Pattern Recognition (Oxford University Press) 28, 30, 31, 47

Bolton, C. T. 1970, ApJ, 161, 1187 20

Brandenburg, A. & Subramanian, K. 2005, Phys. Rep., 417, 1 6, 7, 79

Brown, S. F., Donati, J.-F., Rees, D. E., & Semel, M. 1991, A&A, 250, 463 2, 39, 50, 61

Carroll, T. A., Kopf, M., Ilyin, I., & Strassmeier, K. G. 2007, Astronomische Nachrichten, 328, 1043 84

Carroll, T. A., Kopf, M., & Strassmeier, K. G. 2008, A&A, 488, 781 83

Carroll, T. A. & Staude, J. 2001, A&A, 378, 316 28

Chugainov, P. F. 1976, Izvestiya Ordena Trudovogo Krasnogo Znameni Krymskoj Astrofizicheskoj Observatorii, 54, 89 67

del Toro Iniesta, J. C. 2003, Introduction to Spectropolarimetry (Introduction to Spectropolarimetry, by Jose Carlos del Toro Iniesta, pp. 244. ISBN 0521818273. Cambridge, UK: Cambridge University Press, April 2003.)

Deutsch, A. J. 1958, in IAU Symposium, Vol. 6, Electromagnetic Phenomena in Cosmical Physics, ed. B. Lehnert, 209–+ 1, 9, 39, 44

Donati, J.-F. & Brown, S. F. 1997, A&A, 326, 1135 61

Donati, J.-F., Collier Cameron, A., Hussain, G. A. J., & Semel, M. 1999, MNRAS, 302, 437 76, 85

Donati, J.-F. & Semel, M. 1990, Sol. Phys., 128, 227 2

Donati, J.-F., Semel, M., Carter, B. D., Rees, D. E., & Collier Cameron, A. 1997, MNRAS, 291, 658 2, 3, 63, 83

Donati, J.-F., Semel, M., & Praderie, F. 1989, A&A, 225, 467

Donati, J.-F., Semel, M., & Rees, D. E. 1992, A&A, 265, 669 67, 68, 76, 79

Dupree, A. K. 2003, in The Future of Cool-Star Astrophysics: 12th Cambridge Workshop on Cool Stars, Stellar Systems, and the Sun (2001 July 30 - August 3), eds. A. Brown, G.M. Harper, and T.R. Ayres, (University of Colorado), 2003, p. 1-13., ed. A. Brown, G. M. Harper, & T. R. Ayres, Vol. 12, 1–13 4

Durney, B. R. & Robinson, R. D. 1982, ApJ, 253, 290 80

Eaton, J. A. & Hall, D. S. 1979, ApJ, 227, 907 8

Elstner, D. & Korhonen, H. 2005, Astronomische Nachrichten, 326, 278 79, 84

Goncharskii, A. V., Stepanov, V. V., Kokhlova, V. L., & Yagola, A. G. 1977, Soviet Astronomy Letters, 3, 147 1, 9, 44

Haken, H. & Wolf, H. C. 1996, Atom- und Quantenphysik (Springer) 13

Hatzes, A. P. 1993, in Bulletin of the American Astronomical Society, Vol. 25, Bulletin of the American Astronomical Society, 874–+ 68, 75, 76

Hatzes, A. P., Penrod, G. D., & Vogt, S. S. 1989, ApJ, 341, 456

Hauschildt, P. H. 1992, Journal of Quantitative Spectroscopy and Radiative Transfer, 47, 433 20

Henry, G. W., Eaton, J. A., Hamer, J., & Hall, D. S. 1995, ApJS, 97, 513

Humlícek, J. 1982, Journal of Quantitative Spectroscopy and Radiative Transfer, 27, 437 20

Ilyin, I. V. 2000a, PhD thesis, AA(Astronomy Division Department of Physical Sciences P.O.Box 3000 FIN-90014 University of Oulu Finland) 69

Ilyin, I. V. 2000b, unpublished addendum to the PhD thesis, University of Oulu 69

Jefferies, J., Lites, B. W., & Skumanich, A. 1989, ApJ, 343, 920 3

Johns-Krull, C. M., Valenti, J. A., & Koresko, C. 1999, ApJ, 516, 900 2

Khalack, V. R. & Wade, G. A. 2006, A&A, 450, 1157 3

Khokhlova, V. L. 1976, Astronomische Nachrichten, 297, 217 44

Khokhlova, V. L. & Riabchikova, T. A. 1975, Ap&SS, 34, 403 1

Kochukhov, O., Bagnulo, S., Wade, G. A., et al. 2004, A&A, 414, 613 2, 3

Kochukhov, O. & Piskunov, N. 2002, A&A, 388, 868 43

Kochukhov, O., Piskunov, N., Ilyin, I., Ilyina, S., & Tuominen, I. 2002, A&A, 389, 420 61

Kron, G. E. 1950, Leaflet of the Astronomical Society of the Pacific, 6, 52 9

Kupka, F., Piskunov, N., Ryabchikova, T. A., Stempels, H. C., & Weiss, W. W. 1999, A&AS, 138, 119 20, 23

Kurucz, R. 1993, ATLAS9 Stellar Atmosphere Programs and 2 km/s grid. Kurucz CD-ROM No. 13. Cambridge, Mass.: Smithsonian Astrophysical Observatory, 1993., 13 20, 23, 68

Landi Degl'Innocenti, E. 1992, Magnetic field measurements (Solar Observations: Techniques and Interpretation), 71–+ 27, 67

Landi Degl'Innocenti, E. & Landi Deglinnocenti, M. 1985, Sol. Phys., 97, 239 17

Landstreet, J. D. 1988, ApJ, 326, 967 22

Martínez González, M. J., Asensio Ramos, A., Carroll, T. A., et al. 2008, A&A, 486, 637 65

Narayan, R. & Nityananda, R. 1986, ARA&A, 24, 127 49

Parker, E. N. 1955, ApJ, 122, 293 6

Piskunov, N. 1998, in Astronomical Society of the Pacific Conference Series, Vol. 154, Cool Stars, Stellar Systems, and the Sun, ed. R. A. Donahue & J. A. Bookbinder, 2029–+ 22

Piskunov, N. 2005, in EAS Publications Series, Vol. 17, EAS Publications Series, ed. G. Alecian, O. Richard, & S. Vauclair, 245–250 45

Piskunov, N. E., Kupka, F., Ryabchikova, T. A., Weiss, W. W., & Jeffery, C. S. 1995, A&AS, 112, 525 20, 23

Piskunov, N. E. & Rice, J. B. 1993, PASP, 105, 1415 2, 9, 26, 39

Piskunov, N. E., Tuominen, I., & Vilhu, O. 1990, A&A, 230, 363 51

Press, W. H., Teukolsky, S. A., Vetterling, W. T., & Flannery, B. P. 1992, Numerical recipes in FORTRAN. The art of scientific computing (Cambridge: University Press, |c1992, 2nd ed.) 46, 47, 64

Rees, D. E. 1987, A Gentle Introduction to Polarized Radiative Transfer (Numerical Radiative Transfer), 213–+ 12, 14, 15

Rees, D. E., Durrant, C. J., & Murphy, G. A. 1989, ApJ, 339, 1093 20

Rees, D. E., López Ariste, A., Thatcher, J., & Semel, M. 2000, A&A, 355, 759

Rice, J. B. 2002, Astron. Nachr., 323, 220 26

Rice, J. B. & Strassmeier, K. G. 2000, A&AS, 147, 151 9, 39

Rice, J. B., Wehlau, W. H., & Khokhlova, V. L. 1989, A&A, 208, 179 9, 39, 60, 61

Robinson, Jr., R. D. 1980, ApJ, 239, 961 2

Rodonò, M., Byrne, P. B., Neff, J. E., et al. 1987, A&A, 176, 267 67, 76

Rodonò, M., Messina, S., Lanza, A. F., Cutispoto, G., & Teriaca, L. 2000, A&A, 358, 624 68

Rucinski, S. M. 1977, PASP, 89, 280 67, 76

Rutten, R. J. 2003, in ASP Conf. Ser. 288: Stellar Atmosphere Modeling, ed. I. Hubeny, D. Mihalas, & K. Werner, 99–+ 12

Schrijver, C. J. & Title, A. M. 2001, ApJ, 551, 1099 6

Semel, M. 1989, A&A, 225, 456 1, 10, 39, 44, 67

Semel, M. & Li, J. 1996, Sol. Phys., 164, 417 63

Skilling, J. & Bryan, R. K. 1984, MNRAS, 211, 111

Snieder, R. 1998, Inverse Problems, 14, 387

Socas-Navarro, H. 2005, ApJ, 620, 517 28

Stenflo, J. O. 1994, Astrophysics and Space Science Library, Vol. 189, Solar magnetic fields: polarized radiation diagnostics (Kluwer Academic Publishers) 27

Stift, M. J. 2000, in A Peculiar Newsletter, ed. P. North, Vol. 33 22, 82

Strassmeier, K. G. 1996, in IAU Symposium, Vol. 176, Stellar Surface Structure, ed. K. G. Strassmeier & J. L. Linsky, 289–+ 6

Strassmeier, K. G. 1997, Aktive Sterne : Laboratorien der solaren Astrophysik (Springer) 6

Strassmeier, K. G. 2002, Astronomische Nachrichten, 323, 309 9

Strassmeier, K. G. 2004, in IAU Symposium, Vol. 219, Stars as Suns : Activity, Evolution and Planets, ed. A. K. Dupree & A. O. Benz, 11–+ 4

Strassmeier, K. G., Woche, M., Ilyin, I., et al. 2008, in Society of Photo-Optical Instrumentation Engineers (SPIE) Conference Series, Vol. 7014, Society of Photo-Optical Instrumentation Engineers (SPIE) Conference Series 3, 82

Tuominen, I., Ilyin, I., & Petrov, P. 1999, in Astrophysics with the NOT, ed. H. Karttunen & V. Piirola, 47–+ 69

Vogt, S. S. 1980, ApJ, 240, 567 67, 76, 79

Vogt, S. S. 1981a, ApJ, 250, 327 67, 75

Vogt, S. S. 1981b, ApJ, 247, 975 67

Vogt, S. S. 1988, in IAU Symp. 132: The Impact of Very High S/N Spectroscopy on Stellar Physics, 253–+ 41

Vogt, S. S. & Penrod, G. D. 1983, PASP, 95, 565 1, 9, 39

Vogt, S. S., Penrod, G. D., & Hatzes, A. P. 1987, ApJ, 321, 496

Wade, G. A., Bagnulo, S., Kochukhov, O. Landstreet, J. D., Piskunov, N., & Stift, M. J. 2001, A&A, 374, 265 22, 23, 24, 25, 26

Wade, G. A., Donati, J.-F., Landstreet, J. D., & Shorlin, S. L. S. 2000, MNRAS, 313, 823 3

Washuettl, A. & Strassmeier, K. G. 2001, A&A, 370, 218 41

Wittmann, A. 1974, Sol. Phys., 35, 11 20

Acknowledgements

My thanks go to everyone who supported me during the last years and, thus, contributed to the success of this work.

I am grateful to Klaus G. Strassmeier who, first of all, gave me the opportunity to work on this interesting project. In addition, he also offered me to participate in several international conferences and always gave me advice and support. My special thanks go to Thorsten A. Carroll; without his support this work would not have been possible. I am grateful for his kind supervision and the many helpful and inspiring discussions we had.

Furthermore I want to thank my colleagues of the stellar activity group for fruitful discussions and the nice atmosphere. A special thanks goes to Ilya for obtaining and providing the observational data. Thanks also to Silva and Thomas for detailed revisions of the manuscript. In this context I also thank Nathan and Parham for their help with proofreading and revising English language of the manuscript.

I want to thank everyone at the Astrophysical Institute Potsdam for their kind support, especially the administration and EDV team.

Not to forget all my friends, who even in stressful moments encouraged me and never gave up on my social competence. A special thanks goes to my girlfriend Uta for her encouragement and patience.

I would like to express my gratitude to my parents who always supported me during my whole studies.